TECHNICAL UNIVERSITY OF LIBEREC

NEW TYPES OF FIBROUS ORGANOSILANE MATERIALS AND THEIR POTENTIAL IN REGENERATIVE MEDICINE

Dissertation Thesis

MSc. Johana Kulhánková

2024

"There's Plenty of Room at the Bottom"

Richard P. Feynman

ACKNOWLEDGEMENT

This page serves as a significant expression of my gratitude to all those who, in various forms, contributed to the completion of this thesis, which you are now reading.

First of all, I extend my deepest thanks to my supervisor, Assoc. Prof. Veronika Máková, PhD., and consultant Barbora Nikendey Holubová, PhD. Their unwavering support, invaluable guidance, and boundless patience have been instrumental throughout this journey. Even though they brought four new souls to this world during my studies, they always had time to help, advise and guide me through all the pitfalls of the entire PhD. studies.

The author also expresses profound appreciation to the entire Department of Nanochemistry under the leadership of Assoc. Prof. Michal Řezanka, PhD. Together, they created a friendly atmosphere that made every day a pleasure. I am particularly grateful to Dr. Christopher Hobbs, Jana Müllerová, PhD., MSc. Martin Stuchlík, MSc. Jana Melicheríková, MSc. Petra Karmazínová, MSc. Ilona Krabicová, Jana Karpíšková, PhD., and MSc. Mohamed Ahmed for their fellowship, which I will cherish for the rest of my life.

I extend thanks to all my colleagues who contributed to the outcomes of this work experimentally or by encouraging words.

A special thanks also goes to my current employers who have been lenient with my work performance in the last weeks of writing.

Last but not least, I am immensely grateful to my loving family and friends. They still don't know what I am doing, but they have always believed that it is important. Every time it was needed, I received arms full of understanding. Special thanks to my brother Filip, who, with his intense questions about the state of the work, was the one who kept the adrenaline level in my blood optimal during the last weeks of writing. Infinite gratitude also goes to my partner Libor, for all the support, love and patience he had with me during my studies.

The author acknowledges the assistance provided by the Research Infrastructure NanoEnviCz, supported by the Ministry of Education, Youth and Sports of the Czech Republic under Project No. LM2018124 and the Student Grant Competition of the Technical University of Liberec under project No. SGS-2022-4059.

SUMMARY

This thesis is focused on the fabrication of three biomedically promising organosilanes into fibrous morphology based on a combination of three different fields of science from molecular engineering to supramolecular chemistry. The novel approach involves using a modified sol-gel process in combination with electrospinning techniques for fabricating pure hybrid organosilane fibres. Through this approach, the synthesised organosilanes are effectively transformed into fibrous morphology without the need for typically toxic solvents or additives such as organic polymers, pore-forming agents, or surfactants. The unique combination of inorganic and organic domains connected via strong covalent bonding in the form of nanofibres shows potential in regenerative medicine. This research describes the fabrication of *N,N´*-bis(3-(triethoxysilyl)propyl)oxamide (OBA), *N,N´*-bis(3-(triethoxysilyl)propyl)terephthalamide (BiTSAB), and *N,N´*-bis(3-(triethoxysilyl)propyl)pyridine-2,6-dicarboxyamide (BiTSAP) in 100 mol% in the structure, making them the first created organosilane fibres in such a high molar ratio. Successful preparation of the organosilane fibres was achieved through meticulous observation of structural variations using Fourier Transform Infrared Spectroscopy (FTIR), coupled with adjustments in the sol-gel parameters. On the base of systematic observation and analysis of FTIR spectra, parameters critical for achieving the desired fibrous morphology were determined and conditions, ultimately leading to the successful preparation of the organosilane fibres were set. This analytical approach provided valuable insights into the molecular composition and bonding arrangements within the growing network leading to fibrous formation.

Prepared fibres were characterised using multiple techniques before being employed in biological testing. Following comprehensive characterisation, the fibres were subjected to biological testing to evaluate their compatibility, interaction, and effectiveness in biological environments. This involved assessing cell adhesion, proliferation, differentiation, and overall biocompatibility using various cell culture assays. Formed fibres state cell viability comparable with already known fibrous biomaterials made from organic or inorganic polymers. Moreover, they have demonstrated remarkable efficacy in constructing biomimetic scaffolds, displaying outstanding biocompatibility and seamless interaction with a range of cell types, including stem cells. These fibrous structures possess essential properties for regenerative medicine, fostering a conducive microenvironment for cellular proliferation and differentiation regarding neuroregeneration.

Key words: Biomaterials; Hybrid materials; Organosilanes; Sol-gel process; Electrospinning; Fibres; Stem cells; Neuroregeneration

SOUHRN

Tato disertační práce se zaměřuje na přípravu tří biomedicínsky slibných organosilanů a jejich transformace do vlákenné morfologie na základě kombinace tří různých oblastí vědy od molekulárního inženýrství až po supramolekulární chemii. Tento inovativní přístup zahrnuje využití modifikovaného procesu sol-gel ve spojení s technikami elektrického zvlákňování pro výrobu čistě hybridních organosilanových vláken. Syntetizované organosilany jsou účinně převedeny do vlákenné morfologie bez potřeby užití toxických rozpouštědel nebo přísad, jako jsou organické polymery, porotvorné činitele nebo tenzidy. Jedinečná kombinace anorganických a organických domén spojených kovalentními vazbami ve formě vláken pak vykazuje potenciál nejen v regenerativní medicíně.

Tato práce popisuje syntézu *N,N´*-bis(3-(triethoxysilyl)propyl)oxamidu (OBA), *N,N´*-bis(3-(triethoxysilyl)propyl)tereftalamidu (BiTSAB) a *N,N´*-bis(3-(triethoxysilyl)-propyl)pyridin-2,6-dikarboxyamidu (BiTSAP) ve 100 mol.% ve struktuře, čímž se jedná o první vytvořená organosilanová vlákna v tak vysokém poměru. Úspěšná příprava organosilanových vláken byla dosažena pozorováním strukturálních variací pomocí Infračervené spektroskopie s Fourierovou transformací (FTIR) spolu s úpravami parametrů procesu sol-gel. Na základě systematického pozorování a analýz spekter FTIR byly stanoveny kritické parametry pro dosažení požadované vlákenné morfologie a byly nastaveny podmínky, které vedly k úspěšné přípravě čistě hybridních organosilanových vláken. Tento analytický přístup poskytl cenné poznatky o molekulárním složení a uspořádání vazeb v rostoucí siloxanové síti vedoucí právě k tvorbě vláken.

Připravená vlákna byla charakterizována pomocí nejrůznějších charakterizačních technik a následně byla podrobena biologickému testování k posouzení jejich kompatibility, interakce a účinnosti v biologických prostředích. To zahrnovalo hodnocení adheze, proliferace, diferenciace buněk a celkové biokompatibility v přítomnosti různých buněčných linií.

Vytvořené vlákenné materiály vykazují biokompatibilitu s buněčnými liniemi srovnatelnou s již známými vlákennými biomateriály připravenými z organických nebo anorganických polymerů. Navíc vykazují mimořádnou účinnost při konstrukci biomimetických skafoldů vynikající biokompatibilitou a bezproblémovou interakcí s různými typy buněk, včetně kmenových. Tyto vlákenné materiály tak mají vhodné vlastnosti pro regenerativní medicínu, kdy vytvářejí účinné mikroprostředí pro proliferaci a diferenciaci buněk v souvislosti s neuroregenerací.

Klíčová slova: Biomateriály; Hybridní materiály; Organosilany; Sol-gel proces; Elektrické zvlákňování; Vlákna; Kmenové buňky; Neuroregenerace

LIST OF ABBREVIATIONS

4-OHT	4-Hydroxy-Tamoxyfen
Å	Angström unit
AC	Alternating current
ADSC	Adipose-Derived Stem Cells
Alc	Solvent : Si Ratio
APTES	(3-Aminopropyl)Triethoxysilane
ATCC	American Type Culture Collection
BDNF	Brain-Derived Neurotrophic Factor
BiTSAB	*N,N'*-bis(3-(triethoxysilyl)propyl)terephtalamide
BiTSAP	*N,N'*-bis(3-(triethoxysilyl)propyl)pyridin-2,6-dicarboxamide
BOx	Bridging oxygens
BTESP	1,4-bis(triethoxysilyl)benzene
BTESBP	4,4'-bis(triethoxysilyl)-1,1'-biphenyl
CP/MAS	Cross-Polarization Magic Angle Spinning
DAPI	4′,6-Diamidino-2-Phenylindole
DC	Direct current
DCM	Dichloromethane
DMEM	Dulbecco's Modified Eagle Medium
DMF	Dimethylformamide
EGF	Epidermal Growth Factor
FBS	Fetal Bovine Serum
FGF	Fibroblast Growth Factor
FTIR	Fourier-Transform Infrared Spectroscopy
GFAP	Glial Fibrillary Acidic Protein
H-bonding	Hydrogen bonding
HCl	Hydrochloric acid
HUVEC	Primary Human Umbilical Vein Endothelial Cells
HSA	Human Serum Albumin
iMR-90	Cell line for possible utilization for Neural Tissue Reconstruction
iPSC-NPs	Induced Pluripotent Stem Cell-Derived Neural Precursors
ISO	International Organization for Standardization
IUPAC	International Union of Pure And Applied Chemistry
k ratio	H_2O : Si Ratio
LIN28	Marker of Undifferentiated Human Embryonic Stem Cells
LO	Longitudal Optical Mode
ls NMR	Liquid-State Nuclear Magnetic Resonance
MAS	Magic Angle Spinning
MTEOS	Methyltriethoxysilane
MTT	Multi-Table Tournament Assay
MW	Molecular weight
NANOG	Transcription Factor in Embryonic Stem Cells
NIPH	National Institute of Public Health
NBOx	Non-Bridging oxygens
NSC	Neural Stem Cells
OBA	*N,N'*-bis(3-(triethoxysilyl)propyl)oxamide
OCT4	Transcription Factors that are used to form Induced Pluripotent Stem Cells
PBS	Phosphate-Buffered Saline
PCL	Polycaprolactone
PCR	Polymerase Chain Reaction
PE	Polyethylene

PP	Polypropylene
RLCA	Reaction Limited Cluster Aggregation
RLMC	Reaction Limited Monomer Cluster
PVDF	Polyvinylidenfluoride
RPM	Rotation per Minute
RT	Room temperature
SEM-EDS	Scanning electron microscopy with Energy-Dispersive X-Ray Spectroscopy
SOX2	Transcription Factor Essential for Maintaining Self-Renewal or Pluripotency Of Undifferentiated Embryonic Stem Cells
SPC_01	Human Lung Cancer Cell Line
ss NMR	Solid State Nuclear Magnetic Resonance
SBF	Simulated Body Fluid
TEA	Triethylamine
TEM	Transmission Electron Microscopy
TEOS	Tetraethoxysilane
TEPS	Triethoxyphenylsilane
TESP-SA	3-(Triethoxysilylpropyl)succinic anhydride
TGA	Thermogravimetric Analysis
THF	Tetrahydrofuran
TMOS	Tetramethoxysilane
TO	Transversal Optical Mode
TPP	Tissue Culture Test Plates
TRITC	Tetramethylrhodamine

CONTENT

1 INTRODUCTION

The development of novel nanofibrous materials for regenerative purposes represents a significant advance in the continually evolving field of regenerative medicine. The precise design and engineering of biomaterials have revealed a new era of therapeutic possibilities, offering unprecedented precision and effectiveness in tissue repair and regeneration. The unique properties of nanofibrous materials, including their high surface area, porosity, and biomimetic characteristics, position them as indispensable tools in fostering cellular responses crucial for successful regenerative outcomes. The potential of these materials to mimic the extracellular matrix on a nanoscale range and provide a supportive framework for cellular growth underscores their promise in neuroregenerative medicine and beyond.

As researchers continue to explore the frontiers of material science and regenerative medicine, the convergence of innovative materials with biological systems holds immense promise for unlocking new therapeutic possibilities. This synergy offers insight into a future where damaged tissues can be repaired and organs regenerated with unprecedented precision. Neuroregenerative medicine is at the forefront of scientific exploration and seeks to address the intricate challenges associated with the repair and regeneration of the central nervous system. These biomaterials must possess a combination of key attributes, including robust structural support, a conducive environment for cell growth, high surface area, and structural variability. Such properties are essential for the creation of physical conduits that facilitate the transport of electrical signals and enable communication between neurons. By carefully integrating these features, biomaterials can play a major role in advancing neuroregeneration.

2 THEORETICAL BACKGROUND

2.1 Biomaterials

Due to the limited ability of the human body to regenerate, the development of materials capable of supporting regeneration or replacing permanently damaged parts of the body is a very developed scientific field. Biomaterials are generally defined as systematically inert substances (or groups of substances) that are used to replace damaged or underdeveloped tissues, organs, or parts of organs in the human body to restore proper function [1]. Biomaterials are materials projected to be incorporated into a biological system to replace or supplement any tissue, organ, or function of an organism (**Figure 1**). Biomaterials are primarily used for medical applications. However, they are also used for cell growth in cultures, for blood protein testing in clinical laboratories, for testing biotechnological applications, and in the field of gene diagnostics [2,3].

The basic property of every biomaterial is biocompatibility. This term represents the ability of a material to coexist in close contact with host tissue without causing unacceptable damage to the human body. Equally important is the ability to not exhibit toxic or detrimental effects on biological systems and the ability of the material to perform the desired function with an appropriate host response [4]. The appropriate choice of material for a particular application depends on the properties of the material (hardness, resistance, toughness, etc.), the place of application (soft, hard tissue), structure, composition, stability, and especially biocompatibility [1,2,4].

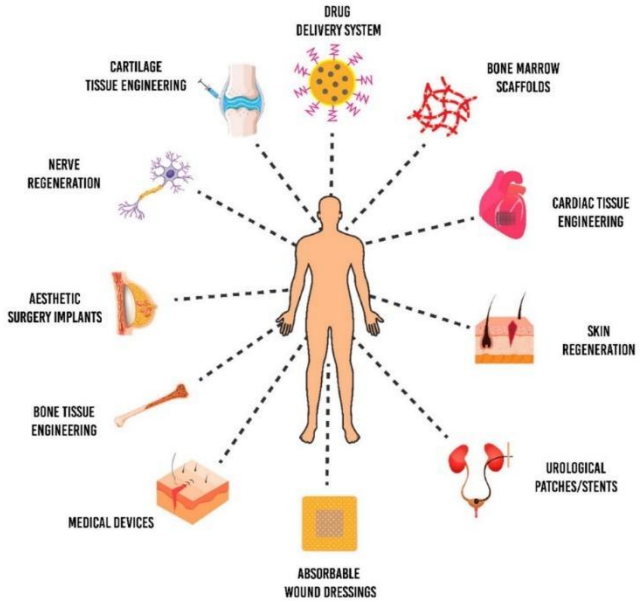

Figure 1 Schematic diagram of the biomaterial and the applicability of the biopolymer in various biomedical applications [5].

Biomaterials are generally divided into four main groups: polymeric, metallic, ceramic, and natural. A special group is represented by composite materials which are created by combining two or more groups of materials. Recently, the emergence of organic-inorganic hybrid materials has been observed in the literature due to their unique physical and chemical properties, combined with the numerous possibilities arising from the coupling of chemistry and engineering methodologies [6].

2.2 Hybrid materials

According to IUPAC (International Union of Pure and Applied Chemistry), a structure composed of an intimate mixture of inorganic components, organic components, or a combination of both, which interpenetrate on a scale of less than 1 μm, can be called a hybrid material [7,8]. Organic-inorganic hybrid materials can be defined as multicomponent compounds having at least one of the inorganic or organic components in sub-micrometric or, more commonly, nanometric sizes [6,9]. They represent a new class of materials offering properties that combine and improve upon those of the individual constituents. The growing interest in hybrid organic-inorganic materials in both academic and industrial fields stems from the convergence of diverse expertise and is driven by the utilisation of a combination of different approaches [6].

2.2.1 Classification

According to the bond between organic and inorganic phases, hybrid materials are divided into two major classes. *Class I* describes those types of hybrid materials where the organic and inorganic components interact via weak intermolecular bonds such as Van der Waals, hydrogen or weak electrostatic bonds. Blend (**Figure 2a**) are those types of hybrids from Class I where strong chemical interactions are missing. Cross-linked polymeric matrix with the inclusion of inorganic clusters or nanoparticles are typical representatives of blends. Another formation belonging to Class I is an interpenetrating network (**Figure 2b**). This form is the inter-penetration of the result of the organic-inorganic network without the formation of strong chemical interactions [9,10].

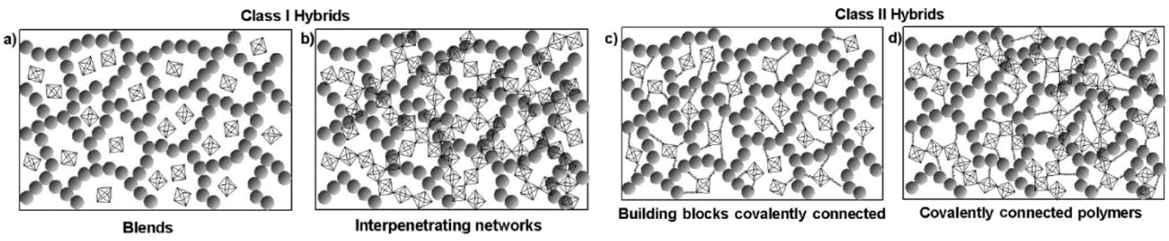

Figure 2 Schematic representation of different types of hybrid materials [11].

Class II describes those types of hybrid materials in which the components are bound with strong covalent or ionocovalent bonds or in which the combination of strong

and weak bonds can be found. For class II it is typical when inorganic structural units, clusters, or particles are covalently bonded to an organic matrix (**Figure 2c**) or when a covalent bond can be found between the inorganic and organic phase (**Figure 2d**) [6,9,10].

There is a gradual change in the strength of chemical interactions as described in **Table 1** which can be also used to distinguish among various hybrid materials.

Table 1 Interaction between species and their properties [11]

Type of interaction	Strength [kJ/mol]	Range	Character
Van der Waals	< 50	Short	Nonselective, nondirectional
H-bonding	5-65	Short	Selective, directional
Coordination	50-200	Short	Directional
Ionic	50-250	Long	Nonselective
Covalent	350	short	Predominantly irreversible

Hybrid materials are currently attractive to create high-performance and high-functional materials [12]. The advantage brought by the production of hybrid materials is their processing. Contrary to pure inorganic materials, high temperature manufacturing process is not needed. Hybrid materials usually show more polymer-like handling because of their large organic centre or because of the formation of a cross-linked inorganic network formed by the series of the same small precursors resembling the polymerisation reaction. Such behaviour can be used in the final shaping of the hybrid materials into many forms such as bulks, films, nanoparticles, and even nanofibres [11,13–15].

The biggest advantage of these materials is the conjunction of both organic and inorganic moiety into one material combining functions and properties that are unattainable for individual units. Due to the huge variability of components from both the organic and inorganic classes, this area of science is very interesting for many industries, as molecular designing provides an opportunity to create an unlimited number of new materials with large spectra of desirable properties [11]. Furthermore, the desirable function of hybrid materials can be changed by modification of the composition at the molecular scale or by further functionalization.

Although hybrid materials made from various metal oxides (Ti [16–18], Al [19,20], Pb [21,22], Mn [23], etc.) have been used in a wide range of applications for several decades, precisely organosilanes form the group of hybrid materials that meet all these demanding requirements.

2.2.2 Organosilanes

Organosilanes belong to a group of hybrid materials described as chemical compounds containing at least one bond between carbon and silicon atoms [24]. Nowadays, organosilanes are used in a wide range of applications, such as coupling agents in

adhesives [25], crosslinking agents to increase mechanical strength [26], or as surface treatments for glass [27], ceramics [28], or metals [29] to improve their chemical resistance. They are also utilised in electronics [30], energetics [31], the pharmaceutical industry [32], and medicine [33]. Especially in medicine, organosilanes play a major role in many areas. They are used for the production of medical supplies, such as micro- and nano needles for transdermal application [34], substitutes in the form of artificial hip joints [35], breast implants [36], or dental and hearing implants [37]. One of the most widespread applications of organosilane hybrid materials in medicine is the production of dental fillings, which serve as a replacement for toxic amalgam fillings. Organosilanes are also often used in orthopaedics, where orthopaedic replacements made from Co-Cr alloys are coated to protect against corrosion [38].

In terms of chemical structure, organosilane hybrid materials can be prepared from monomeric precursors, which may be divided into four basic types according to their chemical nature. Examples of individual groups of precursors are shown in **Figure 3**. Among the four basic types of precursors generally include simple silicon alkoxides (Type I.) such as tetramethoxysilane (TMOS) or tetraethoxysilane (TEOS) which can create inorganic networks with covalent bonds via hydrolysis/polycondensation mechanism. Type II. is a group of alkoxides of various other elements, mainly metals such as Al, Zr, Ti, and Sn which are usually used in combination with Type I. to increase the cross-linking of the silicate network, increase the stiffness, or change the porosity of the final material. Another group is created by alkyl alkoxysilanes whereas the alkyl functionality is represented by non-reactive organic groups (Type III.). These materials are significant by containing the Si-C bond which affects the mechanical properties of the final material and influences the surface properties such as increasing hydrophobicity. The last group describes alkyl alkoxysilanes with reactive organic groups capable of secondary polymerization via polycondensation or other mechanisms (Type IV.) [39].

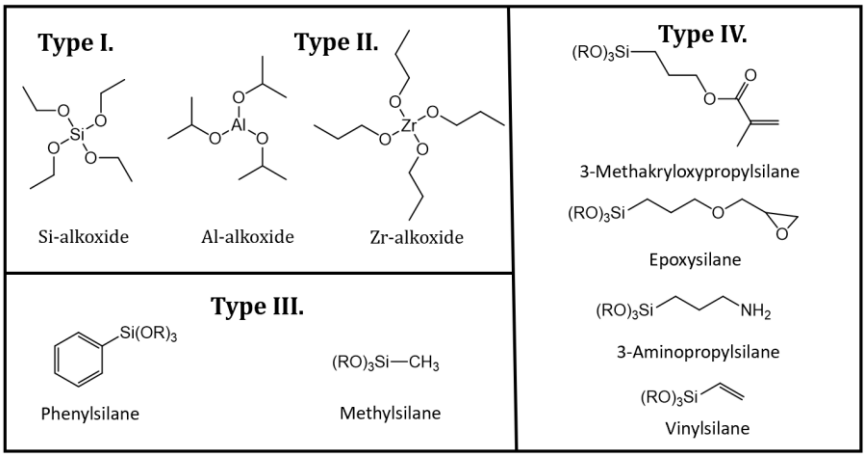

Figure 3 Selected structures of hybrid materials and their classification into individual types [11].

Organosilane precursors can be classified also based on the type or number of organic groups attached to the silicon atom. The number of various alkoxy groups on silicon atoms determines the potential for forming multiple bonds with other silica atoms, thus increasing the resulting level of cross-linking. Therefore, the final hybrid organosilane material may be controlled using a wide variety of functional organo-alkoxysilanes (**Figure 4**) from monofunctional trialkoxysilanes (T), difunctional dialkoxysilanes (D) that form linear oligo or polysiloxane structures to tetraalkoxysilanes (Q) that tend to form highly crosslinked polymers depending on several processing parameters [11,40]. Focussing on the nomenclature pertaining to the bonding between silicon and carbon atoms has significant implications for understanding the structural intricacies of these compounds. Precursors characterised by a solitary Si-C bond are designated as organo-mono-silylated, indicative of the singular connection between silicon and carbon within their molecular architecture. On the contrary, compounds featuring a pair of Si-C bonds are termed organo-bis-silylated, underscoring the presence of two distinct silicon-carbon linkages in their molecular framework.

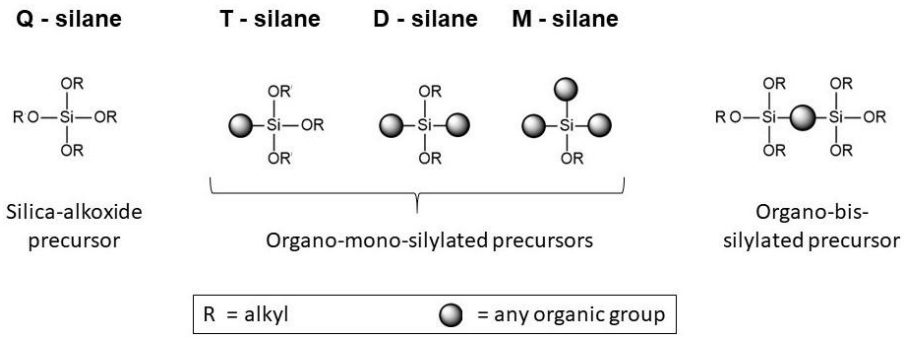

Figure 4 Differences in organosilane structure concerning the position of organic molecules in the silica framework [40].

Bonding characteristics and structural properties can also be used to distinguish between various hybrid organosilane materials. An organic moiety can be present in the final structure in different positions [11]. When containing a functional group allowing an attachment directly to the network, a discrete area of an inorganic network is modified. Such a hybrid molecule is called a network modifier (**Figure 5**) and is typical for organo-mono-silylated precursors. The modification takes place simultaneously during the formation process [11,41]. Such organosilanes have the general formula $Si(OR')_x$-R_{4-x} (x = 1-3), where R represents the organic group (alkyl, aryl, acrylic, epoxy, amino etc.) and R' is a hydrolysable alkoxy unit [40].

The situation is different when the organic segment is modified by more than one spacer. Further reactions lead to the formation of the structure in which the organic

segment is an integral part of the final structure (**Figure 6**). Such formation is typical for organo-bis-silylated (so-called bridged organosilane) precursors referred to as network builders with general formula $(R'O)_3$-Si-R-Si-$(OR')_3$ [40].

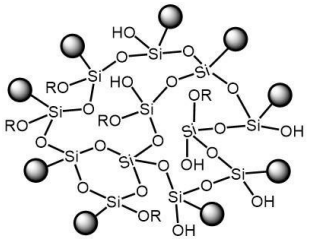

Figure 5 Principle of network modifier [41].

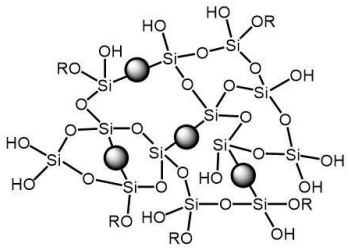

Figure 6 Principle of network builder [41].

Organosilane precursors may also possess many different geometries (rigid, flexible, planar, etc.), which are factors used to precisely control the parameters that govern the structures of the targeted hybrid material [40,42]. In addition, bridged organosilanes have a higher capability to self-organize due to the induction of van der Waals interactions and hydrogen bonding. Such a property is a great advantage in case highly organised structures are required.

2.2.2.1 Processing

There are numerous strategies for processing hybrid organosilanes leading to the formation of desirable morphology or form. Each pathway depends on the specific type of organosilane precursor, its properties, and possibilities. Moreover, its intended application is a crucial factor. Nowadays, the two most widely used approaches are the building block approach and the *in situ* approach [11].

The building block approach operates with groups of atoms that maintain their molecular integrity during the formation process. This formation is achieved using standard coordination chemistry methods where the units react under mild conditions [43].

Contrary*, the in situ* approach requires the chemical transformation of an initial precursor. During the process, organosilane precursors tend to transform into multidimensional structures within the series of reactions. The final structure is then determined by the input parameters and reaction conditions. During the process, it is usual that the properties of a final structure differ from the initials. Controlling the processing parameters is then essential in regarding the desirable function of the created material [44]. An *in situ* approach proves to be suitable for fibre formation, with one such method being the sol-gel process. This method offers the advantage of various parameter modifications, thereby providing flexibility in controlling the fibre formation process. Further details regarding the sol-gel process and its parameters will be described in the following chapter.

2.3 Sol-gel process

The most commonly used *in situ* approach for processing organosilanes is the sol-gel process. The history of silica, silicate and silane chemistry started in the 17th century when a Belgian chemist, physiologist and physician Jan Baptist van Helmont mentioned in his work the reactivity of silicon in glass with air [45]. Two centuries later, the "grandfather" of sol-gel chemistry, Jacques-Joseph Ebelmen, described the process of formation of silyl ethers by mixing absolute alcohol with silicon tetrachloride ($SiCl_4$) [46]. He also published work mentioning the formation of silica gel from silicic ethers in the presence of air moisture. The volume of such a gel contracted with time until the formation of a transparent material similar to glass [47]. Next, significant progress in silicon chemistry was made in the middle of the 19th century with the discovery of the silane (SiH_4) compound and the hypothesis of the existence of an alternative organic chemistry based on silicon rather than carbon was published [48]. The following research led to the confirmation of organic–inorganic hybridisation into the formation of compounds characterised by a carbon–silicon bond. In 1863 the synthesis of the first organosilicon compound, tetraethylsilane, was described by the reaction between $SiCl_4$ and diethyl zinc [6]. Since 1940, mixing organic and inorganic materials has attracted the science community. Although the sol-gel process has been a known technology for nearly a century, it remains a widely used method with extensive applications, as evidenced by the thousands of patents developed from its principles. Despite its longstanding history, numerous research groups continue to explore its potential applications, reflecting the enduring interest in modifying this versatile technique. Until 2022 more than 126,000 research papers were published worldwide mentioning the sol-gel process [49].

2.3.1 Definition and principles of organic sol-gel route

Nowadays is the sol-gel processes well-known techniques of preparation materials by a low-temperature method with possible control of the final product via several processing parameters. In general, it is a process in which monomers into a colloidal suspension (sol), followed by the formation of a continuous network that surrounds the liquid phase (gel) through condensation reactions [50]. This method is used for fabricating metal alkoxides such as $Si(OR)_4$, $Ti(OR)_4$ or $Al(OR)_3$. Less commonly used in the sol-gel process are oxides derived from Ni, Cr, Sn, Pb, or Fe [15]. Metal alkoxides are popular precursors because of their rapid reaction with water. This reaction is called hydrolysis and its mechanism is described in **Equation 1**.

$$\equiv Si - OR + H_2O \leftrightarrow \equiv Si - OH + ROH \quad (1)$$

Two partially hydrolysed molecules can be linked by condensation reaction while forming low-molecular substances such as alcohol (**Equation 2**) or water (**Equation 3**).

$$\equiv Si - OR + HO - Si \leftrightarrow \equiv Si - O - Si \equiv + ROH \quad (2)$$

$$\equiv Si - OH + HO - Si \equiv \leftrightarrow \equiv Si - O - Si \equiv + H_2O \quad (3)$$

This type of reaction can continue to build larger molecules by the process of polycondensation. The number of bonds that a monomer (silica alkoxide) can form is called functionality (*f*). Typical silicon alkoxides are bifunctional (*f=2*), trifunctional (*f=3*) or tetrafunctional (*f=4*). Four is the highest number of bonds to make silicon alkoxides [51].

2.3.2 Sol-gel processing parameters

The same precursors can lead to the formation of different structures by minor changes in conditions[51,52]. The most significant processing parameters and their influence are discussed in the following chapters. **Figure 7** presents a schematic of the routes that one could follow within the scope of sol-gel processing with the right choice of appropriate processing parameters [53]. In the following subchapters, focus will be placed on the definition of fundamental process parameters that significantly influence the sol-gel process, thereby leading to the formation of diverse material structures. These parameters can influence the final product morphology, ranging from fibrous structures to powders or bulk materials.

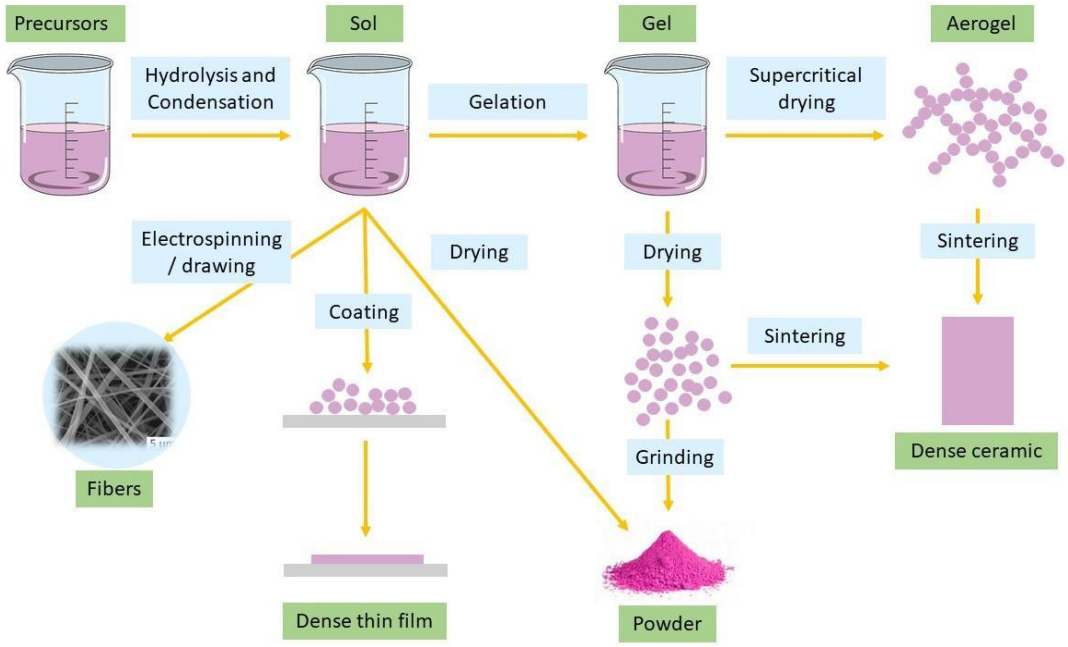

Figure 7 Schematic representation of the different stages and forms of products possibly obtained from the sol-gel process.

2.3.2.1 Catalyst

Compared to transition metals such as Ti or Zr, silicon is in general less electropositive. The partial positive charge on silicon (δ(Si) ~ +0.32 ppm in $Si(OEt)_4$) makes it less susceptible to nucleophilic attack and coordination expansion does not occur spontaneously with nucleophilic reagents [54,55]. Therefore, the noncatalysed reaction may be very slow and exhibit the need to be catalysed, either with a based catalyst (which has a strong negative charge) or with an acid catalyst that has a strong positive charge which is capable of attacking the oxygen (δ^-) atoms of the alkoxy group [54,56]. The resulting structure then differs significantly depending on the catalyst due to the relative rates of hydrolysis and condensation reactions.

Both the hydrolysis and condensation reactions acid or base-catalysed take place through the S_{N-2} mechanism with penta- or hexavalent intermediates/transition states. However, there are differences in the formation of intermediate and transition states which also affect the speed of reactions and subsequently the structure [57]. Under acidic conditions, the alkoxide group is protonated in a rapid first step. The electron density is removed from silicon atoms thereby being more electrophilic and more susceptible to attack by water approaching from the opposite side of the electron density deviation (**Scheme 1**) [58]. As a consequence, a pentavalent intermediate is formed. By formation of this intermediate state, the positive charge on the first protonated alkoxide group is reduced, making it a so-called leaving group (in the form of the alcohol molecule ROH). Thus, hydrolysis results in the transformation of alkoxy groups in the precursor structure (Si-OR) into silanol groups (≡Si-OH) [41].

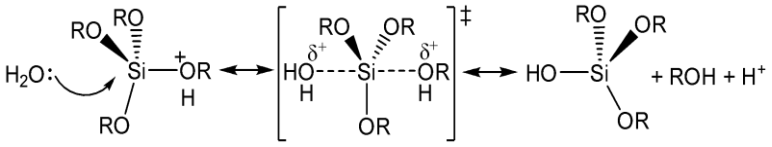

Scheme 1 Acid-catalysed hydrolytic reaction.

On the contrary, during base-catalysed hydrolysis, water dissociates to produce nucleophilic hydroxyl anions that attack the silicon atom. This is followed by the S_{N2}-Si mechanism in which -OH displaces -OR while forming a pentacoordinate intermediate (reaction details in **Scheme 2**). The intermediates decompose through a second transition state in which any of the surrounding ligands can acquire a partial negative charge.

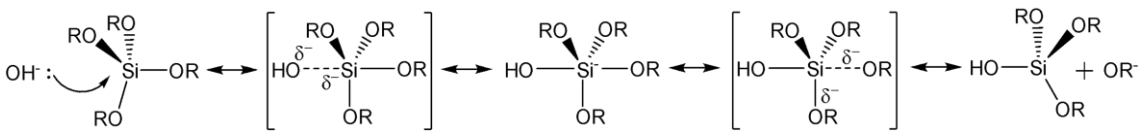

Scheme 2 Base-catalysed hydrolytic reaction with both transition states.

The velocity of each hydrolysis step depends on the stability of the transition state, which depends on the relative electron-withdrawing ability of the -OH or -OR group. This leads to deceleration of the hydrolytic reactions while the reaction mixture is acid-catalysed whereas acceleration of the reaction mixture is base-catalysed. Commonly used catalysts in the sol-gel process are mineral acids and ammonia. However, there are many other catalysts used such as acetic acid, KOH, amines, KF, HF or titanium/vanadium alkoxides. The speed of hydrolytic reactions is also influenced by the strength and concentration of the acid or base catalyst. Aelion et al. [59] described the same behaviour with all strong acids, while weaker acids required a longer reaction time to achieve the same extent of reaction. By varying the catalyst (concentration 0.05 mol.% : TEOS), the effect on gelation time for hydrolysed TEOS with four equivalents of water (k = 4) was observed and summarised in **Table 2** [60].

Table 2. Comparison of a different catalyst used in sol-gel chemistry according to the pH of the initial solution and the gelation time.

Catalyst	Initial pH of the solution	Gelation time [h]
HF	1.90	12
HCl	0.01-0.05	92
HNO_3	0.01-0.05	100
H_2SO_4	0.01-0.05	106
CH_3COOH	3.70	72
NH_4OH	9.95	107
No catalyst	5.00	1000

As well as hydrolytic reactions being affected by the catalyst, equally the catalysation of condensation reactions needs to be taken into consideration. Polymerisation into the form of a siloxane bond (Si-O-Si) occurs by a reaction producing either water (**Equation 2**) or alcohol (**Equation 3**) producing. Although the condensation of silanols can proceed without involving catalysts, their use, especially in organosilanes, is beneficial. Similarly to hydrolysis reactions, numerous catalysts were observed to exhibit both acidic and basic characteristics. However, understanding the catalytic effect of condensation reactions is often complicated by the increase in acidity of silanol groups by the effect of reverse reactions. Grubbs [61] described a method for measuring the rates of silanol condensation reactions based on titration of the reaction solution with a Karl Fischer reagent. Such reactions can define the total content of Si-OH and water in the solution. This reaction assumes a reduction of the apparent water concentration to one-half of its initial value when condensation of the silanol solution is completed. However, the conclusion of this study pointed to an incomplete condensation of trimethylsilanol caused by a rapid reaction of $((CH_3)_3Si\text{-}OH$ with methanol while forming $(CH_3)_3Si\text{-}OCH_3$ and water. With this reaction, the silanol is removed from the system, while the following condensation

equilibrium is established slowly. A rate law deduced from reactions with both acid and base catalysts was found to be the same for both reactions; however, it was calculated to be approximately 500 times as active as KOH in promoting condensation reactions [51].

Within *acid-catalysed condensation*, reactions may occur preferentially between protonated silanols and neutral species (**Scheme 3**). It was observed that a decrease in gel time below the isoelectric point of silica was observed; therefore, it is likely that the mechanism of the reaction is influenced by the protonated silanol species. The protonation of silanol makes silicon more electrophilic and thus more susceptible to nucleophilic attack [51].

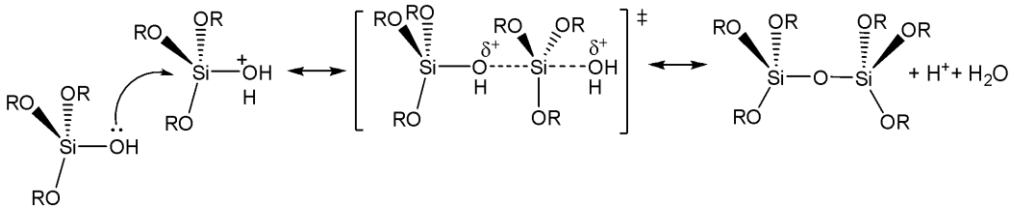

Scheme 3 Acid-catalysed condensation reaction.

The most widely agreed mechanism of *base-catalysed condensation* reaction in aqueous systems (**Scheme 4**) describes the attack of a nucleophilic deprotonated silanol on a neutral silicate species. The reaction takes place above the isoelectric point of silica, where silanols are deprotonated according to their acidity. The acidity of silanols is highly influenced by the environment of the silicon atom. While the remaining groups -OR and -OH are replaced by -OSi, the acidity of the protons on the remaining silanols increases with the reduced electron density of the silicon atoms [51].

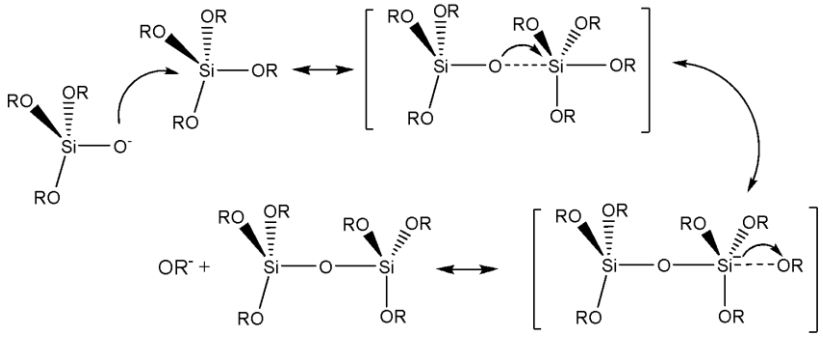

Scheme 4 Base-catalysed condensation reaction.

It is appreciable that the structure of the materials generated by the sol-gel process evolves sequentially as a product of a combination of hydrolysis, condensation, and a reverse reaction. Engelhardt et al. [62] used ^{29}Si NMR to investigate a typical sequence of condensation products at high pH. The results of their observations indicated a typical succession started with a monomer, led by a dimer, linear trimer, and cyclic trimer, cyclic tetramer, and ended with higher-order rings. Hence, according to the above-mentioned

mechanisms and laboratory observations, a base-catalysed sol-gel system is suited when bulk materials or nanoparticles are the desired final morphology whereas acid-catalysed reactions are preferred for gels and fibres [51].

2.3.2.2 Solvent

Among other sol-gel processing parameters leading to desirable products, a wise choice of a solvent and its amount is very important. A polar alcohol-based solvent is used as a homogenising agent, causing the mixing of precursors. This allows originally water-immiscible alkoxide precursors based on silicon to mix with water, which is necessary for initiating hydrolysis reactions (example in **Figure 8**). In addition, solvents prevent or diminish a steric hindrance due to the size of the organic functionality in the organosilane precursor.

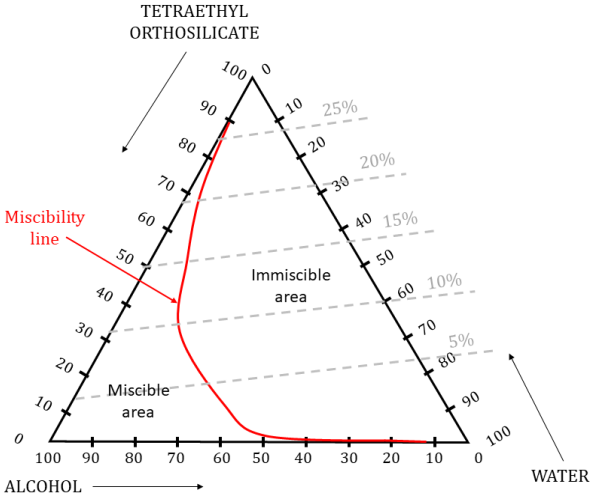

Figure 8 Ternary phase diagram for TEOS, water and alcohol (95% Et-OH + 5% water) at 25 °C [51].

In general, there are two main groups of polar solvents: protic – such as methanol, ethanol, isopropanol, butanol, etc. and aprotic solvents – such as *N*,*N*-dimethylformamide (DMF), tetrahydrofuran (THF), dichloromethane (DCM), etc. which have a different effect on the rates of S_N1 and S_N2 reactions [63]. The availability of labile protons determines whether anions or cations are solvated more strongly through hydrogen bonding. With this definition, protic solvents can promote acid-catalysed reactions and decelerate base-catalysed reactions, whereas aprotic solvents have in reverse effect. Hydrolysis mechanisms may be also affected by hydrogen bonding between species when the weak leaving group can be activated by hydrogen bonding with the solvent while executing the bimolecular nucleophilic reaction mechanism [51,57,64]. The physical properties of different solvents are listed in **Table 3**.

Table 3 Physical properties of solvents most frequently used in sol-gel chemistry divided into two groups (a) protic solvents and (b) aprotic solvents [51].

Solvent	MW	bp [°C]	ρ [g/cm³]	ε	η [mP]	μ [D]
Water	18.01	100.0	1.000	78.5	10.1	1.84
Methanol	32.04	64.5	0.791	32.6	5.4	1.70
Ethanol	46.07	78.3	0.785	24.3	10.8	1.69
2-ethoxyethanol	90.12	135.0	0.930	-	-	2.08
Formamide	45.04	193.0	1.129	110.0	33.0	3.70
N,N-Dimethylformamide	73.10	152.0	0.945	34.7	7.9	3.86
1,4-Dioxane	88.12	102.0	1.034	2.2	10.87	0
Tetrahydrofuran	72.12	66.0	0.889	7.3	-	1.63

MW – molecular weight; bp – boiling point; ρ – density (20 °C); ε – dielectric constant (25 °C); μ - dynamic viscosity (20 °C); η – dipole moment

Together with the availability of a labile proton, polarity has also a very important role concerning the solvating ability. The polarity of a used solvent determines the solvating ability of polar or nonpolar species. To solvate polar, tetrafunctional silicate species, more polar solvents such as water, alcohol or *N,N*-dimethylformamide are usually used in the sol-gel process. Less polar solvents (1,4-dioxane, tetrahydrofuran, etc.) can be used for alkyl-substituted or incompletely hydrolysed systems. It can also be found with solvents with both polar and nonpolar behaviour. Such solvents (methoxyethanol, ethoxyethanol, etc.) are suitable for systems where a distribution of polar and nonpolar species is present [51,65].

The dipole moment of a solvent determines the length between species to which one can distinguish the other's charge. This length is increased with the descending dipole moment of a solvent. Negative charge localised on the reactants can be stabilised with a strong dipole moment of a highly polar solvent and result in a greater extent than the system increasing the energy of activation and consequently in an additional deceleration of the rate condensation [64].

2.3.2.3 Parameter k (H_2O : Si ratio)

The sol-gel process is well known for the possibility of producing different forms of material from a solution, such as bulk, coatings, films, fibres, or powders. Because water is an initiator of hydrolytic reactions, the presence of water is a crucial parameter for the sol-gel process. The amount of water in the solution is directly responsible for the final polysilicate product. An increase in the value of the k parameter promotes the amount of hydrolysis reactions. In theory, ***the k ratio*** can achieve values from <1 to more than 50. Although the stoichiometry amount is a significant factor, the outcome of the sol-gel process is influenced significantly. Pouxviel [66] proved by ^{29}Si NMR analysis, that the increase of the *k* value accelerates the hydrolysis reactions [67]. The hypothesis was observed in three different systems: reaction of a TEOS in a (a) low water system (k = 3), (b) medium water

system (k = 4) and (c) high water system (k = 10). Using ^{29}Si ssNMR, the evolution of Q^0 (nonhydrolysed monomer) units was observed. In the medium-water system, there were Q^0 units were observed after four hours of reaction time, whereas in the high-water system, any nonhydrolysed species were observed after one hour of reaction time.

As discussed above, the hydrolysis is promoted by the increased ***k*** value. However, when ***k*** is increased while maintaining a constant [solvent] : [silicate] ratio, the silicate concentration is reduced. Consequently, hydrolysis and condensation rates are then lowered, which causes an increase in the gelation time. Such a hypothesis was proved on TEOS : ethanol, acid catalysed system (**Figure 9**) [51].

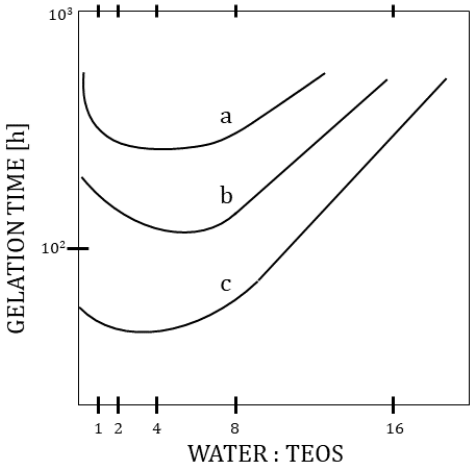

Figure 9 Schematic description of the influence of a k parameter on the gelation time in different ethanol : TEOS ratio a = 3; b = 2; c = 1 [51].

2.3.2.4 Steric and inductive effects

The steric effects of the substituents play an important role in the hydrolytic stability of organosilanes. Hydrolysis and condensation rates are significantly reduced by branched groups, chain length, or degree of branching on the organosilane precursor. However, their concentration does not influence the density or mechanical properties of the final product.

The influence of the inductive effect shows under acid conditions the increase of the hydrolysis rate with the degree of substitution (x) of electron-providing alkyl groups, whereas under basic conditions the effect is reversed. From an experiment by Schmidt et al. [71] is clear that with the consistent acceleration of the hydrolysis reaction with acidic conditions, while using base conditions, the hydrolysis is retarded. Such influence suggests the sensitivity of reaction mechanisms to inductive factors. The inductive effect of substituents is less evident compared to the steric effect but manifests progressively in the stabilisation of transition states during hydrolysis and polycondensation about the used catalyst and charge of the various states. Substitution of alkyl groups to alkoxy results in an increase of the electron density on the substituted silicon. On the contrary, the substitution of the hydroxyl group for alkoxy (hydrolysis) or substitution of -OSi for the alkoxy or hydroxy group (condensation) decreases the electron density in silicon (**Figure 10**). Hence,

alkyl substitution increases the stability of positively charged transition states while hydroxyl or bridging oxygen substitution increases the negatively charged transition state. The kinetics of reactions involving positively or negatively charged transition states should be enhanced by these factors [51].

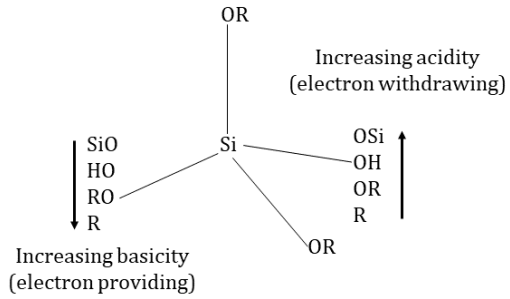

Figure 10 Inductive effects of the substituents (-R, -OR, -OH, -OSi) attached to silicon [51].

2.3.2.5 Other parameters

Beyond the parameters mentioned in previous chapters, other parameters merit to be mentioned. The sol-gel process is typically a stirring using a magnetic stirrer for the whole reaction time to assure homogeneity within the solution and support the speed of the reaction. Another parameter influencing the reaction kinetics is also the temperature. According to Van 't Hoff, when the temperature of the solution increases by 10 °C, the reaction rate increases by 1.5 –4x [68–70]. According to studies in chemical dynamics, the form and dimension of the apparatus and relative moisture are also important influencing parameters [71].

2.3.3 Sol-gel kinetics

The final structure of polysiloxanes or other siloxane products and their application significantly depend on the kinetics of the process. A thorough understanding of the reaction kinetics, mechanism, transformation and subsequent setup of parameters can lead to the control of the final product's properties. Polymerization of alkoxysilanes is a sequence of reactions consisting of three following steps.

1. Hydrolysis: The alkoxy group is substituted by the hydroxyl group in all acidic, base and neutral systems.
2. Condensation: siloxane bridges (-Si-O-Si-) are formed using two hydrolysed alkoxysilane molecules while forming water or alcohol.
3. Phase separation: in this step, the reaction medium loses its homogeneity to form a solid phase on the continuous liquid or liquid phase in a continuous solid. These phases are usually called sol and gel.

The kinetics of each step depends especially on the type of catalyst and solvent, Alc (solvent : Si) ratio and k ratio, nature of a silane precursor or temperature/time of

polycondensation. A large number of conditions can be changed in the sol-gel process which can lead to many variations of the properties and structures of the produced material with differences in kinetic parameters [72–74].

In the following chapter, Q, T, D and M letters will be used to describe the number of attached oxygen atoms to a single silicon (**Figure 11**). Usually, these letters come together with the number, to express the number of hydrolysed (-Si-OH), nonhydrolysed (-Si-OR) and siloxane (-Si-O-Si-) bonds around the central silicon atom.

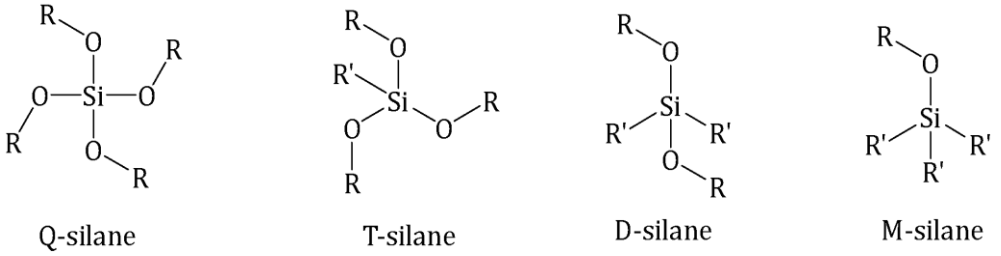

Figure 11 Scheme showing different types of reacted silanes, where -OR is an alkoxy group and R' is any organic group.

The network development in silicate systems proceeds predominantly by condensation of clusters with monomers or with other conglomerations. The progression of condensation depends on the degree of hydrolysis which is closely connected with the amount of water and the catalyst nature. Low pH (~ 2) and k > 4 setup results in complete hydrolysis in the early stages, condensation is then set in between completely hydrolysed species by a process called reaction-limited cluster aggregation (RLCA). Condensation of Q silanes describes monomers (Q^0) or end groups on chains (Q^1). After consumption of the monomers, condensation continues preferentially on Q^1 and more acidic Q^2 and Q^3 units leading to weakly branched units (chain ends preferably react with chain middles). Such created structures are then kinetically stabilised, and the rate of dissolution for trimers or higher polysilicates is very low. At low pH but k < 4, the condensation reactions occur between incompletely hydrolysed species as the alcohol-producing condensation is still slower than water produced. The pattern of condensation reflects the pattern of hydrolysis. Nonhydrolysed -OR groups then nurture the formation of almost linear or weakly branched macromolecules. Therefore, the probability of R-O-R forming a condensation reaction is relatively low and nonhydrolysed extended structures can be highly concentrated without the formation of a gel. Such behaviour is useful for fibre-making production and due to it is systems highly spinnable [51,72,75,76].

Same as at low pH systems, at high pH (above 7) within the k > 4, complete hydrolysis is expected. Reverse reactions are presumably as dissolution and redistribution under basic conditions at Q^1 thereby providing a constant source of monomers. Weakly acid species have a propensity to be protonated, while strongly acid species are inclined to be

deprotonated, the condensation most likely proceeds between those species, which leads to the growth of a network by RLMC aggregation (reaction limited monomer-cluster) or by an Eden growth leading to form a compact non-fractal structure. Contrary, high pH systems with k < 4, prefer to incorporate the nonhydrolysed sites into the growing structures as the condensation within the sites is less likely than at the hydrolysed sites. Such behaviour results in mass/surface fractals or porous reaction products [51,72,77]. Above mentioned structural changes are depicted in **Figure 12**.

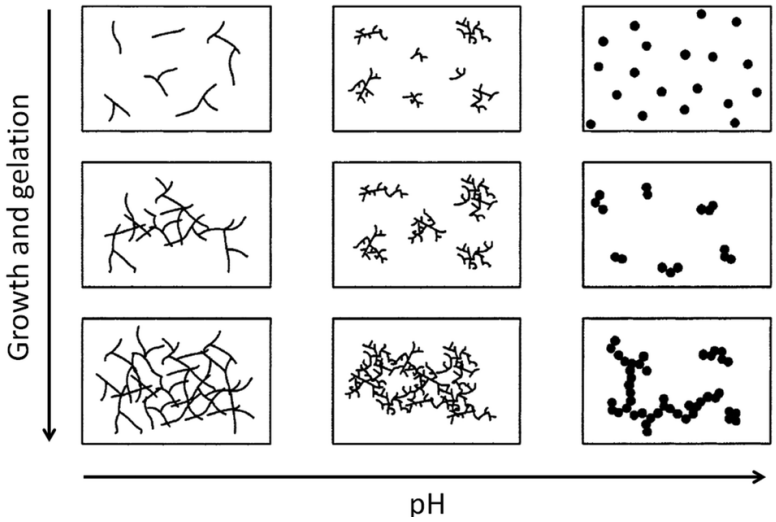

Figure 12 Diagram of a pH effect on the growth of a gel structure [78].

As mentioned before, each of the network developing steps, hydrolysis or condensation, has its own kinetic parameters describing various interactions within -OR, -OH or -OSi functional groups. To describe the kinetic parameters of each reaction, three rate constants (in **Equations 4, 5 and 6**) are required. Assink and Kay [79–81] used ^{1}H and ^{29}Si NMR to define rate constants during the initial stages of acid-catalysed TMOS reactions. They also considered several kinetics models to determine the evolution of functional groups surrounding silicon atoms.

$$\equiv Si - OR + H_2O \overset{k_H}{\leftrightarrow} \equiv Si - OH + ROH \quad (4)$$

$$2 \equiv Si - OH \ \frac{k_{CW}}{2} \leftrightarrow \ 2\,(\equiv Si - O) - Si + \ H_2O \quad (5)$$

$$2 \equiv Si - OH + SiOR \ \frac{k_{CA}}{2} \leftrightarrow \ 2\,(\equiv Si - O) - Si + \ ROH \quad (6)$$

Mechanism of hydrolysis and condensation with rate constants (k_H for hydrolysis; k_{CW} for condensation of water and k_{CA} for condensation of alcohol)

^{1}H NMR was used to identify the relative amount of methoxy functional groups and methanol molecules as a function of reaction time. These observations resulted in the demarcation of two limiting cases. The first limit case occurs when the hydrolysis rate is much larger than the condensation rate. Methoxy functional group concentration is quickly

reduced to the value corresponding to complete hydrolysis without any condensation. Contrary, when the hydrolysis rate is much smaller than the condensation rate, hydrolysis is followed by quick condensation and the reduction in methoxy functional group concentration occurs at a rate proportional to the hydrolysis rate. ^{29}Si NMR was used to observe the rate of formation of Si-O-Si bonds. As well as within ^{1}H NMR, two limiting cases need to be contemplated based on **Equation 7**.

$$\frac{\partial[(SiO)Si]}{\partial t} = k_{cw}[SiOH]^2 + k_{ca}[SiOH][SiOR] \quad (7)$$

When k_{cw} is much higher than k_{ca}, the condensation rate will be proportional to $[SiOH]^2$. Contrary, if k_{ca} is much higher than k_{cw}, the condensation rate will be proportional to [SiOH] [SiOR]. After all, two main simplifications for kinetics were defined, the rate constants for hydrolysis as well as condensation depend on the functional group reactivity (not on the silicon chemical environment), and the rate coefficient for a specific species going through one of the mentioned reactions is the product of a statistical factor and the appropriate functional group rate coefficient [51,66,72,76].

2.3.4. Sol-gel process of fibres

Acknowledging the importance of meticulously parameterizing the sol-gel process to optimize the formation of elongated, minimally branched molecular chains, thus enhancing the propensity for the resultant material to create fibrous morphology, the following experiments were guided by several fundamental principles. These principles are based on a comprehensive understanding of the intricate interplay between various process parameters and their impact on the molecular architecture and final morphology of the synthesised materials. Consequently, the ensuing investigations are designed to systematically explore and modify focused parameters, aiming to elucidate their nuanced effects on the sol-gel process and the resulting material properties. The following insights applied in subsequent experiments were:

1. Choice of the **acid catalyst** due to the relative rates of hydrolysis and condensation reactions
2. **Substoichiometric coefficient** of water as an initiator of hydrolysis
3. Suitable **choice of solvent** is essential to enable the miscibility of all components within a chemical system, facilitating uniform distribution, effective interaction, and efficient dissolution
4. **Amount of solvent** to optimize molecular interactions and promote the desired chemical transformations considering the processing challenges posed by highly bulky molecules and taking into account both a steric hindrance and inductive effects

By leveraging these insights, it becomes feasible to modulate key aspects of the sol-gel reaction together with the reaction time and temperature to achieve the formation of the desired structures effectively.

2.4 Electrospinning techniques

Electrospinning is a versatile technique for generating fibres from polymer solutions or melts [82]. Remarkable progress has been made with regard to the development of electrospinning methods and the engineering of electrospun nanofibres to suit or enable various applications [83]. Nanofibres produced from electrospinning techniques exhibit diverse features, such as high porosity, high surface area-to-volume ratio, small pore size, low weight and good mechanical properties [84]. The first patented method of producing nanofibrous materials from polymeric solution was recorded in 1934 by American scientist Anton Formhals [85]. In general, the electrospinning technique means the application of high voltage to a polymer fluid. Such charges are induced in the fluid until the critical amount. When charges within the fluid reach a critical amount, a fluid jet will erupt from the droplet at the tip of the feeder resulting in the formation of a Taylor cone. The electrospinning jet travels towards the region of lower potential, which in most cases, is a grounded collector [86].

2.4.1 Definition and principles

Needle electrospinning is the most often electrospinning technique used in conventional electrospinning setups [87]. A schematic representation of the single-needle experimental setup with horizontal configuration can be seen in **Figure 13**. The needle is fed with a polymeric solution and embedded into the linear dispenser which presses the piston of the needle at constant speed. The source of high voltage is connected to the metallic part of the needle which is aimed toward the grounded collector. The distance between the needle and collector is one of the crucial parameters of the setup. Needle electrospinning is a very helpful technique in a scale of laboratory production, however, for the industrial scale it is not efficient enough.

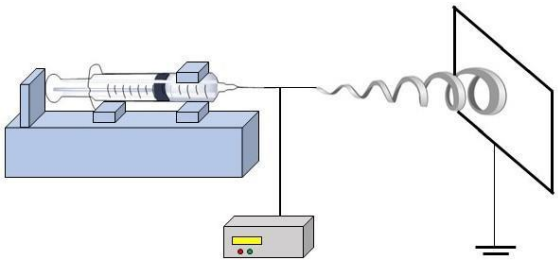

Figure 13 Needle electrospinning setup.

A huge discovery regarding electrospinning techniques was made in 2003 when Jirsák et al. [88] patented a method of nanofibres production from a polymer solution using

electrospinning and a device for carrying out the method. This technology introduced a method of nanofibres production from a polymer solution using electrospinning in a direct current (DC) electric field created by a potential difference between a charged electrode and a counter electrode. The polymer solution for spinning is supplied into the electric field using the surface of a rotating charged electrode. In a device for carrying out the method, the charged electrode is pivoted and part of its circumference is immersed in the polymer solution. The free part of the circumference of the charged electrode is positioned opposite the counter electrode [89]. This device was commercialised by Elmarco Company under the name Nanospider™ (**Figure 14**), however, the setup is based on one single jet from a nozzle and the electrospinning process is not very productive.

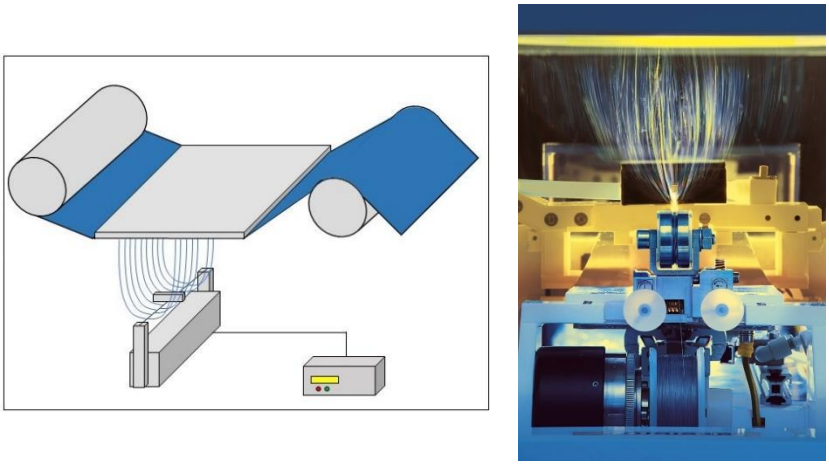

Figure 14 Nanospider setup (a) and the inner part of the chamber of the spinning device (b).

In 2014, another device for nanofibres production based on alternating current (AC) was described (**Figure 15**). Within AC electrospinning combined with an aptly shaped, needleless spinning electrode in the form of a metallic rod (10 mm) highly efficient nanofibrous plums are generated by changing the polarity. The resulting plume carries no residual charge, hence no electrically active collector is required for capturing the created nanofibres. The movement of fibres is realised by a physical phenomenon – electric wind [90,91].

Using the AC method results in higher productivity in comparison with the DC method. Depending on the polymeric solution and shape of the electrode, production efficiency can be higher up to 20x. Another difference is the possibility of producing more voluminous layers using the AC method, which is not possible in DC spinning. Due to the absence of an active electrical collector, extremes can be created with this method porous layers of nanofibres of arbitrary thickness. The disadvantage of the AC variant is a lower degree of homogeneity of the resulting structures compared to the DC variant [92].

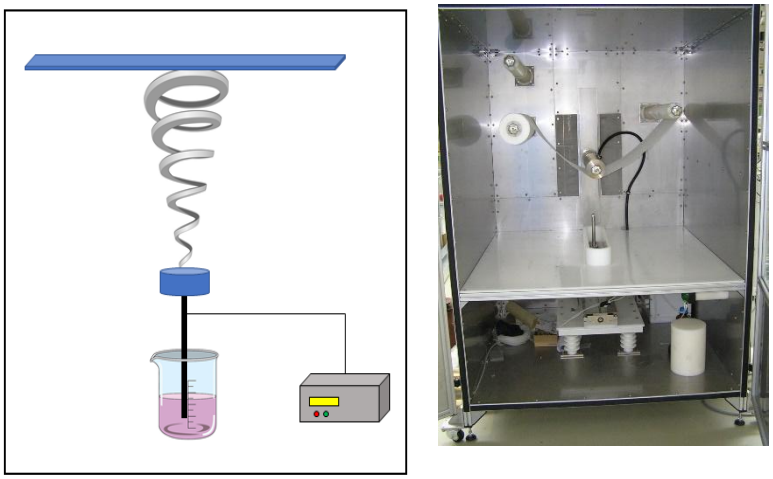

Figure 15 KOMES setup (a) and the inner part of the chamber of the spinning device (b).

2.4.2 Electrospinning processing parameters

The electrospinning process is influenced by different factors and parameters which further influence the morphology and features of created fibres [83,93]. The most important parameters are solutions parameters – viscosity, conductivity, surface tension, etc., environmental parameters such as temperature, humidity and air velocity in the electrospinning chamber and parameters of the spinning itself such as distance between the tip and collector, electrical potential, flow rate, the molecular weight of the selected polymers, the geometry of the collector [82].

The viscosity of the spinning solution is one of the crucial aspects of the fibre-forming technology that can be determined by varying the concentration of the polymer solution. Solutions with optimum viscosity only yield the respective fibres in the micro to nanoscale diameters [41]. During the electrospinning process, the applied voltage also needs to be high enough to overcome the surface tension of the spinning solution to produce fibres. Yang and his group [94] reported that by reducing the surface tension of the solution without changing the concentration, beaded fibres could be converted into smooth fibres. Likewise, the conductivity of the solution may play a key role in the fibre formation process [93]. Similarly, the diameter and shape of the gauge may change the diameter and morphology of the fibre respectively. It was examined that there is a minimal distance required to give the fibre sufficient time to evaporate redundant solvent before [40,65,95,96]. Environmental parameters such as humidity, temperature, pressure or airflow also strongly influence the electrospinning process and they are directly influencing fibrous morphology, diameter and properties. Higher temperatures can reduce solvent evaporation and lead to a decrease in fibre diameter, additionally, at high temperatures, the viscosity of a polymer solution can decrease, altering the fibre production. The level of humidity influences fibre formation while impacting the electrospinning process. Water molecules in the environment can condense on the fibrous surface, leading to bead

formation on the fibre. Controlling the mentioned parameters is critical in producing electrospun fibres with the desirable properties and characteristics [93].

2.5 Regenerative medicine

Regenerative medicine is a specific branch of research which is focused on developing methods to regrowth, repair or replace damaged or diseased cells, organs or tissue. It combines several research areas including classical medicine, tissue engineering, gene therapy, stem cell research as well as materials science [97]. The field of regenerative medicine can be still evaluated as relatively new since many of the techniques and therapies are still experimental. However, the potential of this field is enormous when it has the potential to change the ways how we treat a variety of diseases such as organ transplantations, heart diseases, diabetes or neurological disorders. Regenerative medicine is a promising field of research which can greatly improve the quality of life for many people. It is a rapidly advancing area which brings breakthroughs and developments thus undoubtedly continuing to push the boundaries of what is possible in medicine [98].

The field of regenerative medicine is an area where hybrid organosilanes can play an important role. While combining features from both, organic and inorganic moiety, they can be used to create scaffolds for tissue engineering, as drug delivery agents or form artificial organs [40].

2.5.1 Sterilisation

The possibility to sterilise a biomaterial is a very important parameter of every medical device. This is a critical and at the same time indispensable step of biomaterial preparation, which aims to prevent contamination and infection. Sterilisation aims to eliminate all forms of microbial life, including highly resistant bacterial spores. There are several methods on how to sterilise a biomaterial and the choice of a method depends on the type of sterilised material, its intended use or the acceptable level of risk [99].

The most commonly used sterilisation technique of medical devices is autoclaving. This method involves high-pressure steam and high temperature (typically at 121 – 134 °C). The principle is based on the property of liquids under pressure. Water is heated to a temperature above its normal boiling point. Such high temperatures and pressure are lethal to microorganisms and spores in a short time, making autoclaving a very effective method for a wide range of materials including surgical tools and laboratory equipment. However, the disadvantage of the autoclaving process is that sterilised materials are exposed to extreme conditions and many materials (plastics, rubbers, etc.) are not capable of managing this process [100,101].

Dry heat sterilisation is another widely used method using the heating of a material for high temperatures. Used temperatures are between 160 – 180 °C which is high enough

to kill the microorganisms by protein denaturation, oxidative damage and loss of the cell water. This method is less effective than autoclaving. However, the conditions are not that extreme and can be used for heat-resistant materials that may be damaged by moisture or radiation. On the other hand, the dry heat sterilisation process is slower and less effective, because the dry air is not as effective as steam or radiation. In addition, the process has to be carefully controlled to ensure the maintenance of the temperature during the whole time throughout the whole chamber [102,103].

Radiation sterilisation is another often-used method, especially for heat-sensitive materials. This process involves exposing the material to ionising radiation (gamma rays from cobalt-60 or electron beams). Such high-energy radiation causes ionisation of the microbial DNA, leading to lethal damage and the destruction of the microorganisms. This process is very effective and fast. Sterilisation requires only minutes/hours (depending on the dose of radiation and the nature of the contamination). Also, this method can be used for various materials including plastics, rubbers, textiles, etc. However, using this method, changes in the physical and chemical properties of certain materials can be observed as well as the degradation of their functionality. In addition, radiation sterilisation facilities are very complex and expensive and they require very strict safety measures due to the potential of ionizing radiation [104,105].

Gas plasma sterilisation is a low-temperature technique involving gas plasma. It is effective, relatively cheap and safe for a huge variety of materials. It is a modern, innovative method using a mixture of gases as a sterilising agent combined with microwave energy which creates plasma. The principle involves the use of a low-temperature plasma generated from gases such as hydrogen peroxide or peracetic acid which are excited by energy. Plasma consists of reactive species such as free radicals, charged particles or UV photons. These reactive species can destroy microorganisms through mechanisms of oxidation, breaking down the cell walls or damaging DNA. The biggest advantage lies in the possibility to effectively sterilise a wide range of materials including heat and moisture-sensitive ones without leaving any toxic residues. In addition, it is a fast process which often takes less than an hour to go through. Moreover, it is an environmentally friendly technique as the used gases are easily broken down into non-toxic components. On the other hand, the effectiveness of this process depends on the type of material, the nature of the contamination, the type of used gas and the conditions of the process itself. Furthermore, not all materials are compatible with this type of sterilisation. Especially those which are sensitive to oxidation. Moreover, within this method, limitations in penetration make it less suitable for use with complex or dense material [106,107].

Nowadays, chemical sterilisation is not quite a common process, especially in the bioimplantation process. The principle is in the use of chemical agents such as ethylene oxide, hydrogen peroxide or peracetic acid. These chemicals can penetrate the material and kill microbes effectively. However, the presence of residuals is often detected which can be harmful also to humans and the environment [108]. Individual sterilisation methods, their advantages and disadvantages are listed in **Table 4**.

Table 4 Methods of sterilisation together with their advantages and disadvantages.

Method of sterilisation	Principle	+	-
Autoclaving	High-pressure steam heat	Effective	Extreme conditions for the material
Dry heat	Heating in the oven	No extreme conditions	High temperatures, less effective
Radiation	Ionising radiation (gamma rays/electron beams)	Highly effective	Can cause changes in material structure
Gas plasma	Low-temperature gas plasma	Effective, suitable for a huge variety of materials	Can cause changes in material structure
Chemical	Using chemical agents (ethylene oxide/hydrogen peroxide/peracetic acid)	Effective	Residuals can cause problems after the application

Sterilisation of an implant or any medical tool is a very important part of the process of preparation because the consequences of insufficient sterilisation and subsequent infection can have unfathomable consequences. The sterilisation process must be validated to ensure its effectiveness and at the same time does not cause undesirable changes in the properties of the material [99].

2.5.2 *In vitro* testing

In vitro testing refers to experiments performed in a controlled environment outside of the living organism using laboratory equipment. Such experiments aim to provide insights into the probable behaviour of the developed material in the environment of a living organism with the help of various body fluids or cell lines, bacteria and other biological entities. *In vitro* testing is often used in the early stages of scientific research or drug delivery development. Such type of testing is a key part of biological and medical research used for a wide variety of purposes.

2.5.2.1 Simulated Body Fluid

To simulate the conditions in living organisms, a solution copying the composition of the inorganic part of blood plasma was designed. This solution was named Simulated Body Fluid (SBF) and its preparation is covered by ISO 23317:2014. The solution does not

contain cells or other blood elements, but initial bioactivity testing is sufficient [109]. In general, the formation of an apatite layer on the surface of the tested material to form a bond with the bone tissue is considered to fulfil the conditions of bioactivity. *In vivo* investigation of cell and tissue interactions with biomaterials is a time- and financially very expensive step necessary for the development of new biomaterials, and therefore a faster and cheaper variant of testing primary interactions was proposed [110,111]. The research carried out by Ogino et al. [112] can be considered as the first attempt to create a solution for testing biomaterials *in vitro*. The research included tests of the newly discovered Bioglass® in a solution containing TRIS and hydrochloric acid at pH 7.4. After the end of the experiment of the tested material, the presence of a new layer was detected, it was rich in calcium and phosphorus, which is determined as an indicator of biocompatibility. In the past, testing in SBF was widely used, as it was a very fast method for finding out the first information and breeding biomaterial in the body environment, which did not require any demanding equipment or specialised workplace. Even though testing in SBF can provide useful insight, this method cannot fully replicate the complex environment of the human body. Now, with the development and availability of technology, including the growing number of specialised workplaces, testing in SBF is not used much anymore. Later it also turned out that this solution was not suitable for all types of materials and there is a need to be modified.

2.5.2.2 Biocompatibility assessments

Biocompatibility testing is one of the most used methods when new biomaterials are developed. Biocompatibility has also been described as the ability of a material to perform with an appropriate host response in a specific application. Biocompatibility or safety evaluation addresses the identification of an appropriate host response [113]. Using this testing procedure, the compatibility with living tissue is observed. Such a method involves a series of tests and evaluations to determine whether the tested material is suitable for use within living organisms without causing adverse reactions or harm. Moreover, the biocompatibility concept also includes biofunctionality and biostability. The chemical, mechanical, and structural properties of biomaterials, their interaction with the biological environment or even the methodology of assessment can influence biocompatibility. High biocompatibility and functional properties are very desirable for new biomaterials [114]. The primary goals of biocompatibility testing are to ensure the safety of future patients and to prevent adverse reactions or complications [115].

Observing cytotoxicity is usually the first in the row of biocompatibility testing procedures. It evaluates the biological reactivity of living cells to the biomaterial extract solutions including cell viability, growth, and metabolic activity [116]. Biomaterials are

assigned cytotoxicity ratings based on visual evidence of changes in the morphology of cell lines together with their lysis, rounding, spreading and proliferation [117]. Usually, three different qualitative cytotoxicity tests are used according to the mechanical properties of the tested material.

The direct contact method is used when low-density material is observed. Using these methods, material is placed directly onto cells pre-growth in the testing container. Cells are then incubated together with the material. During the incubation, toxic agents derived from the material can diffuse into the culture medium and attack the cells while causing cellular damage such as structural disintegration, alternation of cell morphology, reduction in cell adhesion and proliferation or decrease in metabolic activity [114].

Cytotoxicity elution test is an *in vitro* qualitative analysis suitable for polymeric materials. The principle of this method is the application of a material's extract to the pre-cultivated mice fibroblasts and incubated for 48 hours [118]. After incubation, morphological changes of the cells are microscopically observed. Materials are then classified in the range from 0 to 4 according to the percentage of deformed cells. The highest accepted number for biomedical purposes is 2 (mild reactivity) [114].

MTT assay is currently the most commonly used method for cell growth rate and toxicity testing [119]. The principle of this test is to measure the metabolic activity of living cells by colourimetry. Yellow tetrazolium salt 3-(4,5-dimethylthiazol-2-yl)-2,5-diphenyltetrazolium bromide is dosed in the exact volume into the test wells and incubated. Living cells metabolise the salt by mitochondrial enzymes into purple formazan crystals. The colour intensity of the solution then corresponds to the number of living cells [114].

2.5.2.3 Cell biology

Cell biology testing, also known as cellular biology testing, is a branch of biology that focuses on the study of cells, which are the fundamental units of life [120]. Cell biology testing involves a wide range of techniques and experiments to understand the structure, function, and behaviour of cells [121]. It refers to a range of scientific experiments, assays, and procedures used to study the structure and functions of cells. These tests can investigate different cellular processes like cell division, growth, protein synthesis, DNA replication, energy metabolism, signal transduction, and cell death in the presence of tested material [122]. To comprehend the behaviour of living cells, the careful selection of a cell culture is a pivotal factor in cell biology testing. This technique involves growing cell lines under controlled conditions, typically outside their natural environment. This is usually accomplished through the use of a special growth medium that contains the necessary

nutrients and conditions for the cells to grow. By changing these factors, different aspects of cell biology can be tested [123].

The fundamental technique within cell biology testing starts with cell culture. It involves growing and maintaining cells from multicellular organisms in a controlled environment outside of their natural habitat, usually in a laboratory. Cell culture allows the study of cells in isolation, free from the complexities of an organism. This can provide valuable insights into how cells function, their biochemistry, and the effects of drugs or toxins [124]. There are two basic approaches used, cell lines and primary cultures.

Cell lines are defined as cultures that by subculturing (passage from dish to dish) have been serially transplanted in an uninterrupted sequence of generations and can be maintained for a long time [125]. They have been adapted to grow continuously in an artificial environment, typically a growth medium in a petri dish. They are valuable research tools in cell biology testing due to their ability to proliferate indefinitely, allowing for large-scale studies and long-term experiments. Usually, cell lines are derived from tumours and can divide indefinitely. They are often easier to grow and maintain compared to primary cells. However, cell lines also have their limitations. They do not perfectly mimic the *in vivo* state of cells within a tissue or organism, which can limit the applicability of the results. Moreover, issues such as cell line contamination and misidentification can impact the reliability of the research findings. Despite these challenges, cell lines continue to be a cornerstone of cell biology research due to their ease of use, reproducibility, and the wealth of knowledge they have provided over the decades [121,125–127].

Primary cultures are cells taken directly from the living organism (human, animal, plant). After isolation, they grow in the culture medium in a laboratory environment [125]. Using primary cell culture, cells usually maintain their original function and morphology for a limited time, and they do not proliferate indefinitely. Therefore, these cultures are often more challenging to maintain than cell lines. However, such a method provides a closer overview of the *in vivo* state and is particularly useful in understanding the biology of different tissues. The cells are more likely to display typical cellular functions and responses, making them valuable for biological and medical research. Also, primary cells are considered more biologically relevant than immortalised cell lines because they retain many of the characteristics of the tissue from which they were derived. On the other hand, primary cells have a limited lifespan and can only be cultured for a finite number of passages [128,129].

Cellular biology encompasses the study of different cell types, ranging from prokaryotic cells (e.g., bacteria) to eukaryotic cells (e.g., plant and animal cells) and also investigates the various components and structures within cells, including organelles such

as the nucleus, mitochondria, endoplasmic reticulum, or cytoskeleton by employing a wide range of laboratory techniques, including microscopy, flow cytometry, molecular biology methods (PCR, DNA sequencing), and cell-based assays to observe and manipulate cells [128,130]. Cell biology testing is a dynamic and iterative process that involves careful planning, execution, and analysis. It is an essential tool for advancing our understanding of cellular processes, disease mechanisms, and the development of new materials in various fields of biological and medical research [131]. The transition from *in vitro* to *in vivo* experiments is an essential step in the development and evaluation of new drugs, treatments, therapies or biomaterials. It involves testing a substance or intervention first in a controlled, simplified laboratory setting (*in vitro*) serving as a preliminary step and then in living organisms (*in vivo*) to understand its effects, safety, and efficacy. The choice between *in vitro* and *in vivo* experiments depends on the research goals and the stage of scientific investigation [132,133].

2.5.3 *In vivo* testing

In vivo testing is a scientific and medical research testing method that involves conducting experiments or studies inside a living organism, typically an animal or a human being, to understand how biological processes, drugs, medical devices, or other interventions affect the organism [134]. *In vivo* testing is an essential component of biomedical and pharmaceutical research which can help scientists understand the mechanisms underlying diseases and the action of drugs. Animal models help to study the progression of a disease or the mode of action of a particular drug [135]. By *in vivo* testing determination of the effectiveness of a drug or treatment in a real biological system can be also observed. It also includes testing whether the intervention achieves the desired therapeutic effects. *In vivo* experiments also provide data on how a drug is absorbed, distributed, metabolised, and excreted within a living organism (pharmacokinetics) and how the drug exerts its effects on the body (pharmacodynamics) [136].

In vivo testing is an essential step in the drug development process, preclinical research, and various aspects of medical research. It helps bridge the gap between *in vitro* (test tube or cell culture) experiments and clinical trials in humans. Animal models, such as mice, rats, rabbits, dogs and non-human primates, are commonly used for *in vivo* testing due to their genetic and physiological similarities to humans. However, ethical considerations and differences in biology between species can limit the generalizability of results to humans, and researchers must carefully design experiments and interpret findings accordingly [137,138].

3 CURRENT STATE OF RESEARCH and THESIS GOALS

Until 2021 only 5 solitary research papers regarding the preparation of the purely hybrid organic-inorganic organosilane nanofibres have been published [40,41,139–141] by three independent groups. Fibrous materials prepared by *Tao et al.* were composed mainly of inorganic components based on TEOS. The content of the organic component was only 10^{-4} mol.%. On the contrary, *Schramm et al.* used different processes for the formation of hybrid organosilane fibres. These fibres were prepared by co-condensation of (3-triethoxysilylpropyl)succinic anhydride (TESP-SA) with either TEOS, methyltriethoxysilane (MTEOS) which were hydrolysed and reacted subsequently with (3-amino)propyltriethoxysilane (APTES). However, the prepared sol had to be adjusted before electrospinning with a non-ionic surfactant Triton X-100 as a spinnability facilitator which remained inside the prepared hybrid fibres. These types of nanofibres have several disadvantages such as low mechanical resistance, or decomposition with the change of the environment in which they have been formed. They also need to be prepared with the presence of cationic surfactants and/ or various types of gelators. The third group, *Máková et al.* [40] successfully prepared the first types of hybrid organic-inorganic nanofibres in a significantly high molar ratio of hybrid precursors inside the silica matrix without any use of spinnability facilitators. Such preparation was possible with a proper understanding and use of sol-gel processing parameters during the synthesis of a spinnable sol subsequently processed via a properly set DC electrospinning.

This research aimed to enhance our understanding of the parameterization influence on the sol-gel process impacts the resulting structure, particularly concerning the development of fibre-forming solutions using synthesised organosilane precursors with specific molecular designs. As a result of the overall experimental process, this thesis aimed particularly to investigate the influence of the Alc parameter (alcohol/Si mol.% ratio) on sterically bulky synthesised molecules, utilizing infrared spectroscopy as the primary analytical technique. Following the accurate definition of sol-gel process parameters, the study shifted its attention towards fabricating fibrous organosilane materials from these specifically designed precursors and assessing their physicochemical characteristics, with a particular emphasis on their potential applications in regenerative medicine. A key aspect of the investigation was exploring the potential conductivity of the fabricated fibrous materials, considering their role in supporting tissue regeneration, especially in cardiological and neuroregenerative applications.

4 EXPERIMENTAL PART

4.1 Organosilane materials

For this work, three organosilane structures were designed considering further applications in regenerative medicine. Proposed molecules were organo-bis-silylated, containing aliphatic, aromatic and heterocyclic disposition in the silica framework.

4.1.1 Synthesis

For the synthesis of organo-bis-silylated precursors, followed chemicals were used: dichloromethane (DCM; 95% Penta, CZ), toluene (98% Lach:Ner; CZ), triethylamine (TEA; 99% Sigma-Aldrich, CZ), (3-aminopropyl)triethoxysilane (APTES; 98% TCI Chemicals, CZ), oxalyl chloride (98% Sigma-Aldrich, CZ), terephthaloyl chloride (99% Sigma-Aldrich, CZ), 2,6-pyridinedicarbonyl dichloride (97% Sigma-Aldrich, CZ), anhydrous $MgSO_4$ (Lach:Ner, CZ). When dry solvent (DCM, Toluene) was needed, they were left for several days over molecular sieves (4 Å; Acros Organics).

4.1.1.1 N,N'-bis(3-(triethoxysilyl)propyl)oxamide

Precursor *N*,*N*´-bis(3-(triethoxysilyl)propyl)oxamide (OBA) was synthesised in a 3-necked round bottom flask, dried overnight at 90 °C. The dried flask was sealed and subjected to several vacuum/argon cycles before finally introducing argon. 200 ml of dry DCM was introduced and stirred at 350 RPM whilst in an ice bath, being kept between 0 and 5 °C. 120 mmoles of TEA and 80.5 mmoles of APTES were then added to the reaction flask. Separately, 40 mmoles of oxalyl chloride was dissolved into 30 ml of dry DCM within a flask which had been dried in an oven and introduced with argon in a similar manner as the flask above. The DCM/oxalyl chloride was added to the main reaction flask drop-wise using a syringe, turning the reaction yellow. Following the addition of DCM/oxalyl chloride, the reaction flask was left stirring at RT for 3 h at 350 RPM. The described reaction can be seen in **Scheme 5**.

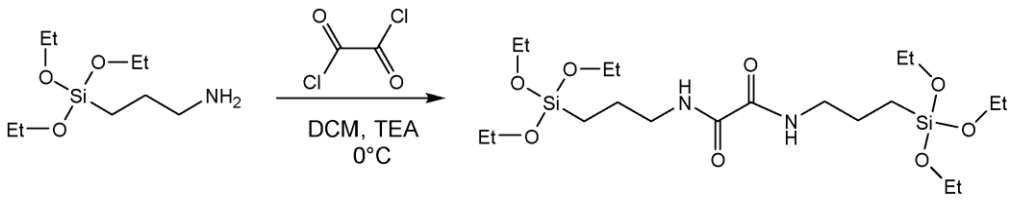

Scheme 5 Synthesis of OBA precursor.

The reaction solution was then mixed with 300 ml of Milli-Q water and separated, with the organic phase re-collected and the process was repeated a further 2 times before finally obtaining the organic phase product over anhydrous $MgSO_4$. The remaining solvents were removed via evaporation. 100 ml of toluene was then added to the product and mixed for 5 min before removal of solvents via evaporation, with this process repeated a total of 3 times. 50 ml of toluene was then added to the product, and filtered through a paper membrane

filter followed by passing the product through a 0.22 µm PVDF syringe filter. Finally, the remaining solvent was removed via evaporation, and lastly a drying at 1 mbar and 50 °C for 10 h, producing a slightly viscous yellow compound with an obtained yield of 85.9 %. The produced OBA was stored under argon and in a fridge until use. The product was confirmed for structure and purity using mass spectroscopy (Sciex X500R QTOF HR, USA) and NMR (500 MHz instrument; JEOL, Japan) at 25 °C. The calculated theoretical *m/z* for the product was 496.264, with *m/z* 496.265 found. ^{1}H-NMR (400 MHz, DMSO-d_6) δ (ppm) 8.72 (2H, t, CH_2NH-), 3.74 (12H, q, OCH_2CH_3), 3.10 (4H, m, $NHCH_2CH_2$), 1.51 (4H, m, $CH_2CH_2CH_2$), 1.14 (18H, t, OCH_2CH_3), 0.51 (4H, t, CH_2CH_2Si). ^{13}C-NMR (400 MHz, DMSO-d_6) δ (ppm) 160.1, 57.8, 41.5, 22.3, 18.2, 7.3.

4.1.1.2 N,N'-bis(3-(triethoxysilyl)propyl)terephtalamide

Precursor *N,N´*-bis(3-(triethoxysilyl)propyl)terephtalamide (BiTSAB) was synthesised in a 3-necked round bottom flask, dried overnight at 90 °C. The dried flask was sealed and subjected to several vacuum/argon cycles before finally introducing argon. 250 ml of dry Toluene, 50.0 mmoles of terephthaloyl chloride (TPC) and 150 mmol TEA were added to the reaction flask. Dropwise addition of 101.0 mmoles of APTES turning the reaction yellow. The reaction flask was left stirring at RT for 3 h at 350 RPM. The described reaction can be seen in **Scheme 6**.

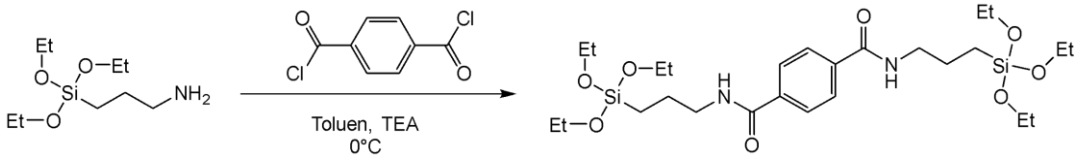

Scheme 6 Synthesis of BiTSAB precursor.

The reaction solution was then mixed with 300 ml of Milli-Q water and separated, with the organic phase re-collected and the process was repeated a further 2 times before finally obtaining the organic phase product over anhydrous $MgSO_4$. The remaining solvents were removed via evaporation. 100 ml of toluene was then added to the product and mixed for 5 min before removal of solvents via evaporation, with this process repeated a total of 3 times. 50 ml of toluene was then added to the product, and centrifuged at 25.000 rpm/20 min/RT several times. This process was followed by passing the product through a 0.22 µm PVDF syringe filter. Finally, the remaining solvent was removed via evaporation, and lastly a drying at 1 mbar and 50 °C for 10 h, producing a slightly viscous yellow compound with an obtained yield of 80.9 %. The produced BiTSAB was stored under argon and in a fridge until use. The product was confirmed for structure and purity using mass spectroscopy (Sciex X500R QTOF HR, USA) and NMR (500 MHz instrument; JEOL, Japan) at 25 °C. The calculated theoretical *m/z* for the product was 496.264, with *m/z* 496.265 found. ^{1}H-NMR (400 MHz, DMSO-d_6) δ (ppm) 8.72 (2H, t, CH_2NH-), 3.74 (12H, q, OCH_2CH_3), 3.10 (4H, m,

NHCH_2CH$_2$), 1.51 (4H, m, CH$_2$CH_2CH$_2$), 1.14 (18H, t, OCH$_2$CH_3), 0.51 (4H, t, CH$_2$CH_2Si). ^{13}C-NMR (400 MHz, DMSO-d$_6$) δ (ppm) 160.1, 57.8, 41.5, 22.3, 18.2, 7.3.

4.1.1.3 N,N'-bis(3-(triethoxysilyl)propyl)pyridin-2,6-dicarboxamide

Precursor *N*,*N*′-bis(3-(triethoxysilyl)propyl)pyridine-2,6-dicarboxyamide (BiTSAP) was synthesised in a 3-necked round bottom flask, dried overnight at 90 °C. The dried flask was sealed and subjected to several vacuum/argon cycles before finally introducing argon. 250 ml of dry Toluene was mixed with 20.0 mmoles of 2,6-pyridinedicorbonyl dichloride and 100 mmol TEA were added to the reaction flask. Dropwise addition of 40.0 mmoles of APTES turning the reaction yellow. The reaction flask was left stirring at RT for 3 h at 350 RPM. The described reaction can be seen in **Scheme 7**.

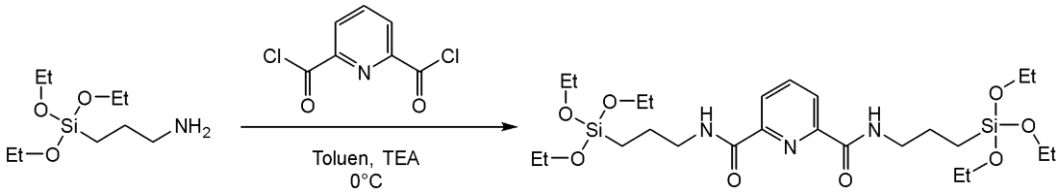

Scheme 7 Synthesis of BiTSAP precursor.

The reaction solution was then mixed with 300 ml of Milli-Q water and separated, with the organic phase re-collected and the process was repeated a further 2 times before finally obtaining the organic phase product over anhydrous MgSO$_4$. The remaining solvents were removed via evaporation. 100 ml of toluene was then added to the product and mixed for 5 min before removal of solvents via evaporation, with this process repeated a total of 3 times. 50 ml of toluene was then added to the product, and centrifuged at 25.000 rpm/20 min/RT several times. This process was followed by passing the product through a 0.22 µm PVDF syringe filter. Finally, the remaining solvent was removed via evaporation, and lastly a drying at 1 mbar and 50 °C for 10 h, producing a slightly viscous yellow compound with an obtained yield of 80.9 %. The produced BiTSAP was stored under argon and in a fridge until use. The product was confirmed for structure and purity using mass spectroscopy (Sciex X500R QTOF HR, USA) and NMR (500 MHz instrument; JEOL, Japan) at 25 °C. The calculated theoretical *m/z* for the product was 496.264, with *m/z* 496.265 found. ^{1}H-NMR (400 MHz, DMSO-d$_6$) δ (ppm) 8.72 (2H, t, CH$_2$N*H*-), 3.74 (12H, q, OCH_2CH$_3$), 3.10 (4H, m, NHCH_2CH$_2$), 1.51 (4H, m, CH$_2$CH_2CH$_2$), 1.14 (18H, t, OCH$_2$CH_3), 0.51 (4H, t, CH$_2$CH_2Si). ^{13}C-NMR (400 MHz, DMSO-d$_6$) δ (ppm) 160.1, 57.8, 41.5, 22.3, 18.2, 7.3.

4.2 Sol-gel process

To create a polymeric solution a one-pot synthesis was utilised. The principle of such a reaction lies in mixing all chemicals (silica precursor, solvent (Ethanol 99.8%), demineralised water (pH = 7; conductivity = 0.055µS/cm; resistivity 18.2 MΩ/cm) and catalyst (HCl, 35%)) in a round-bottom flask, heating and stirring for a certain time interval

at room temperature. After homogenization of the sol, the flask is heated in an oil bath up to 90 °C and refluxed while mixing for 350 RPM. It is important to observe the growth of the polysiloxane matrix and to end the process of heating and stirring at the appropriate time before the structure grows too much within the 3D network or before the sol enters the gel phase. The final sol is then adjusted to the viscosity of around 60 mPas and ready to be spun.

4.3 Electrospinning

Hybrid fibres were prepared using two different electrospinning techniques. First, on a laboratory scale, the needle jet technique was used. The final, concentrated sol was fed into the syringe (5ml) with a dosing needle (thickness 1.2mm). The needle was inserted into the linear dispenser (ONE Syringe Pump; Darwin Microfluidics, FR) with a feeding rate of 1.5 - 5 ml/h. The distance between the needle and the collector was set to 15 – 25 cm. Voltage for needle electrospinning was in the range of 20 – 30 kV.

Likewise, the Nanospider™ (Elmarco s.r.o., CZ) device for industrial production was used to examine the fabrication of such created fibres in higher doses. The parameters of the Nanospider™ device are listed in **Table 5.** The climatic conditions for all the experiments were regulated by NS AC150 1000/2000 (Elmarco, Czech Republic) air conditioning system.

All nanofibres were deposited on a polypropylene spunbond support textile material using different speeds from 10 mm/min to 20 mm/min.

Table 5 Parameters of Nanospider device for creating organo-bis-silylated fibres in 100 mol% concentration.

Distance between electrode and collector [mm]	Voltage [kV]		Speed of cartridge [mm/s]	Temperature [°C]	Humidity [%]
	Electrode	Collector			
160	<40	>-20	<340	<24	>30

4.4 Instrumental techniques

4.4.1 Liquid-state Nuclear magnetic resonance (ls NMR)

Nuclear Magnetic Resonance (NMR) spectroscopy was undertaken at ambient temperatures recorded using the spectrometer JNM-ECZ400R/M1 (400 MHz, JEOL, Japan). ^{1}H spectra were referenced to the chemical shift for the solvent residual peak employed in the measurement.

4.4.2 Solid-state Nuclear magnetic resonance (ss NMR)

Solid-state NMR spectra were recorded at 11.7 T using a Bruker AVANCE III HD spectrometer. The 3.2-mm and 4-mm cross-polarization magic angle spinning (CP/MAS) probes were used for ^{13}C (Larmor frequency of 125.783 MHz) and ^{29}Si (Larmor frequency

of 99.367 MHz) measurements, respectively. ^{13}C NMR chemical shift was calibrated using α-glycine (^{13}C: 176.03 ppm; carbonyl signal) as an external standard and ^{29}Si NMR spectra were referenced to the external standard M_8Q_8 (^{29}Si: -109.8 ppm). ^{13}C MAS NMR spectra were acquired at the speed of the sample rotation of 20 kHz using a 10 s recycle delay and 4096 scans. The ^{29}Si CP/MAS NMR spectra were recorded at an MAS rate of 7 kHz with the number of scans of 4096. A recycle delay of 5 s and cross-polarization (CP) contact time of 5 ms were used for the recording of ^{29}Si CP/MAS NMR spectra. In all cases, high-power ^{1}H decoupling (SPINAL64) was used for the removal of heteronuclear coupling. Samples were packed into ZrO_2 rotors and subsequently kept at room temperature. NMR experiments were conducted under active cooling, done at 298 K temperature. Bruker TopSpin 3.2 pl5 software package was used for the processing of the spectra.

4.4.3 Fourier-transform infrared spectroscopy (FTIR)

The sol-gel reaction was assessed periodically using FTIR Spectrometer Nicolet iZ10 (Thermo Fisher Scientific, USA) with an ATR diamond crystal angle of 45° and a spectral range of 4000 – 400 cm^{-1}, with 16 sample scans, 32 background scans, a resolution of 2 cm^{-1}, apodization: Happ-Genzel, atmospheric suppression correction and baseline. All solution-based samples were analysed after the evaporation of ethanol. Electrospun NFs were analysed using the above method with samples measured as prepared without post-electrospinning treatment and also after heat treatment at 175 °C for 18 h.

4.4.4 Thermogravimetric analysis coupled with FTIR (TGA-FTIR)

Samples were analysed on a Q500 thermogravimetric analyser (TA Instruments, New Castle, USA). Samples were placed on a platinum pan and analysed in an inert atmosphere of nitrogen with a flow rate of 60 $ml.min^{-1}$. The samples were heated at 10 $°C.min^{-1}$ from RT to 850 °C. When TGA was run in tandem with FTIR Nicolet IS10 (Thermo Fisher Scientific, USA), a transfer line heated to 220 °C from the TGA furnace connected to a 20 cm quartz cuvette heated to 240 °C was used for FTIR analysis of the TGA products.

4.4.5 Viscometer

The dynamic viscosity of the final solution was measured by Vibro Viscometer SV-1A (A&D Instruments, UK). All samples were measured in polycarbonate sample cups (2 ml) in temperature range 20 – 30 °C. Before every measurement, the viscometer was calibrated by a one-point calibration process using demineralised water.

4.4.6 Scanning electron microscopy (SEM)

Formed fibres were studied by SEM (ZEISS, Sigma Family, DE). All samples were viewed as secondary electron images (28 kV). The fibre diameter was characterised using NIS Elements software (LIM, CZ) and was assessed from a total of 200 measurements.

4.4.7 Determination of specific surface area (BET)

Before analysis, the fibre sample was degassed in a vacuum at 105 °C for 48 hours to remove residual solvents. The raw data was obtained using the adsorption of krypton at liquid nitrogen temperature (AutoSorb iQ MP, Quantachrome, Florida, USA), with the BET surface area calculated using ASiQwin software.

4.4.8 Contact angle measurement

The contact angle of the created fibrous layers was observed using the See System E instrument (Advex Instruments, Czech Republic). The liquid used for the measurement of the contact angle comprised demineralised water with a surface tension of 72.53 mN/m. The Kwok-Neumann and Li-Neumann model was used to calculate the surface energy.

4.5 Biological assessment

Since the proposed structures are intended for the needs of regenerative medicine, several experiments regarding such needs were performed. In collaboration with the Physiological Institute Academy of Sciences Prague, biological testing with several cell lines was demonstrated to confirm created fibre properties.

4.5.1 Sterilisation

Sterilisation of all samples was performed by plasma low-temperature steriliser (Sterrad 100 NX, Switzerland). The STERRAD 100NX steriliser is based on 58 % to 59.5 % H_2O_2, which is concentrated to approximately 83 % before being evaporated. The sterilisation approving tests were performed in a certified laboratory of the National Institute of Public Health (NIPH) according to ČSN EN ISO 11137-1.

4.5.2 Simulated Body Fluid

Simulated Body Fluid (SBF) was prepared according to ISO 23317:2007; Implant for surgery – In vitro evaluation for apatite-forming ability of implant materials. This standard describes the method and capability of apatite formation on the surface of a material during immersion in Simulated Body Fluid. All samples were tested as triplicates in PE testing tubes and stored in incubated heat at 36.6 °C for 28 days.

A plastic bottle (PE, 1000ml) was placed into the water bath. 700 ml of demineralised water subjected into the bottle was stirred for 350 RPM and heated for 36.5 °C. The exact order of chemicals (described in **Table 6**) was added to the demi water. At the end of the preparation, a few drops of 1M HCl were added to the solution to adjust the pH for pH 7.4.

Table 6 Order, amount purity and mass of reagents used for preparation of 1 L of SBF.

Reagent	Amount [g]	Purity [%]	Molar mass [g·mol^{-1}]
NaCl	8.035	99.5	58.443
$NaHCO_3$	0.355	99.5	84.006
KCl	0.225	99.5	74.551
$K_2HPO_4 \cdot 3H_2O$	0.231	99.0	228.222
$MgCl_2 \cdot 6H_2O$	0.311	99.0	203.303
HCl	39	99.0	36.460
$CaCl_2$	0.292	96.0	110.984
Na_2SO_4	0.072	99.0	142.042
TRIS	118	99.0	121.135

4.5.3 Cell biology testing

4.5.3.1 Cell viability

Initial biocompatibility screening was performed in compliance with the standard ISO 10993-5: Biological evaluation of medical devices - Tests for in vitro cytotoxicity, using 3T3-A31 murine fibroblasts. Cell viability upon exposure in direct contact was evaluated by standard MTT test and extended to include cell membrane disruption examination through spontaneous LDH leak test. Cell morphology was monitored at all time points (24, 48 and 72 hours) by fluorescent microscopy. In general, cells were cultured under standard conditions (5 % CO_2, 37 °C) in a complete culture medium containing high glucose Dulbecco's modified Eagle's medium (DMEM, Sigma-Aldrich, USA) supplemented with 5 % fetal bovine serum (FBS, Gibco), 5 % new-born calf serum (NBCS, Sigma-Aldrich, USA) and 1 % penicillin-streptomycin (P/S, 10.000 U, Sigma-Aldrich). Cytotoxicity study was performed in a 24-well format. For the exposure, 30.000 cells were seeded per well and cultured 24 hours prior to the experiment. On the day of exposure, the culture medium with unattached cells was discarded, circular sections of nanofibrous sheets (10 mm diameter) were placed directly on the bottom of each well and 1 ml of fresh complete medium was added. Each sample was tested in triplicate. Positive control (7 % DMSO) and cell control were handled and tested under the same conditions. In the selected time points (24, 48 and 72 hours) culture medium was collected for the LDH leak test and cell viability of adhered cells was tested by standard mitochondrial oxidoreductases activity test using MTT assay (1 mg/ml, serum-free medium, 120 minutes). The degree of MTT reduction was determined spectrophotometrically by absorbance intensity reading at 570 nm (background subtracted at 650 nm) on SynergyHTX multi-plate reader (BioTek). The percentage of viable cells was calculated as cell control (CC, considered 100 %) absorbance proportion and statistically analysed. The lactate dehydrogenase (LDH) spontaneously released to the culture medium during the exposure period was tested by CyQUANT™ LDH Cytotoxicity Assay (Invitrogen, Thermo Fisher Scientific, USA) according to the manufacturer´s instructions. The substrate

colour reaction was measured spectrophotometrically at 490 nm (background subtracted at 680 nm) on a multi-plate reader. The percentage of LDH in culture media as a sign of cellular membrane disruption was calculated as the absorbance proportion of the completely lysed population (at the corresponding time point) after subtracting culture medium control values. Results were statistically analysed.

For the cell morphology evaluation, cells were seeded on round coverslips (12 mm) and treated under the same conditions. After the exposure period, cells were washed with Dulbecco's PBS solution (DPBS, pH 7.4), fixed with ice-cold methanol and stained with DiOC6(3) (0.1 μg/ml) for 45 minutes in the dark. Cell nuclei were counterstained with DAPI using Fluoroshield™ mounting medium (Sigma-Aldrich, USA). The imaging was carried out on MDi8 inverted microscope (Leica) using HC FL PLAN objective and integrated LAS X system.

Quantitative data obtained by biocompatibility testing were statistically analysed and presented as mean values ± standard deviation (SD). Results were evaluated statistically using GraphPad Prism 8.4.2. The normality of the data was tested by the D'Agostino-Pearson test or the Shapiro-Wilk test. If the data passed the normality test, statistical significance between control and groups was determined by ANOVA with Dunnett´s comparative test (p set to 0.05) or by Brown-Forsyth and Welch ANOVA with Dunnett´s T3 multiple comparison test (p set to 0.01) for pairs of groups.

4.5.3.2 Biocompatibility

The biocompatibility of prepared samples was further tested by three types of human stem cells: adipose-derived stem cells (ADSC) for basic estimations, Human Umbilical Vein Endothelial Cells (HUVEC) alone or cultivated with ADSC for possible utilisation for soft tissue reconstruction, and after all human neural stem cells, induced pluripotent stem cell-derived neural precursors (iPSC-NPs) IMR-90 cell line for possible utilisation for neural tissue reconstruction. All cells were cultivated under static conditions in 24-well polystyrene plates (Techno Plastic Products, Switzerland). The cells were seeded in a density of 25.000 cells/cm^2 and cultivated in a humidified air atmosphere with 5 % CO_2, and at 37 °C in a cell incubator (Thermo Fisher Scientific, USA). The cultivation medium depended on the cell type.

4.5.3.2.1 The human adipose-derived stem cells (ADSC)

ADSC were isolated from lipoaspirate according to our earlier study [142]. In passage 2, the cells were characterised by flow cytometry (Accuri C6 Flow Cytometer) for the presence of markers typical for mesenchymal stem cells (CD105, CD90, CD73, CD29) and the absence of markers of other cell types, such as hematopoietic cells and endothelial

cells (CD45, CD34, CD31). The ADSC were grown in Dulbecco's Modified Eagle Medium (DMEM), supplemented with 10 % of fetal bovine serum (FBS; both for Gibco, Thermo Fisher Scientific), 1 % of ABAM antibiotics (100 IU/mL of penicillin, 100 μg/mL of streptomycin, and 0.25 μg/mL of Amphotericin B; Sigma-Aldrich, USA) and basic fibroblast growth factor (FGF2; 10ng/mL, GenScript).

4.5.3.2.2 Primary Human Umbilical Vein Endothelial Cells (HUVEC)

HUVEC (PromoCell, Germany) were isolated from the vein of the umbilical cord which is commonly used for physiological and pharmacological investigations. They express endothelial markers CD31/105. Cells were cultivated in Endothelial Growth Medium 2 (EGM-2) (PromoCell, Germany), a low serum cell culture medium containing 2 % of FS. Also, in the case of co-cultivation with ADSC, the cell type mix was cultivated in EGM-2.

4.5.3.2.3 The human neural stem cells (NSC)

iPSC line was used, derived from female foetal lung fibroblasts (IMR-90 line, ATCC, USA) transduced with a lentivirus-mediated combination of OCT4, SOX2, NANOG and LIN28 human cDNA [143]. Clone selection, validation of the iPSC line and derivation of neuronal precursors are described in detail in [144]. Human induced pluripotent stem cell-derived neural precursors (iPSC-NPs) were routinely cultured in tissue culture flasks coated with poly-L-ornithine (0.002 % in distilled water) and laminin (10 μg/ml in DMEM : F12), both obtained from Sigma (St. Louis, MO). Culture medium comprised of DMEM/F12 and Neurobasal media mixture (1:1) supplemented by B27 and N2 supplements (GIBCO, Life Technologies, Grand Island, NY), penicillin and streptomycin (50 U/ml, GIBCO), FGF (10 ng/ml), EGF (10 ng/ml) and BDNF (20 ng/ml) (PeproTech, London, UK) was replaced every second day.

4.5.3.3 Cell morphology and distribution

The cell morphology and spreading of ADSC were evaluated by the filamentous actin (F-actin), visualised by staining cells with phalloidin conjugated with tetra-methylrhodamine (TRITC) (Sigma-Aldrich, MO, U.S.A., Cat. No. P1951), in order to evaluate the assembly of the actin cytoskeleton and the shape and spreading of cells on the tested materials. The cell nuclei were counterstained by DAPI (1:200). The samples were stained for 1 hour at room temperature, and rinsed with PBS. Fluorescent images were acquired by an Olympus IX71(Obj. 20x).

The growth and differentiation of NSCs were analysed using immunofluorescent labelling for βIII-tubulin, nestin, neurofilaments and GFAP. For immunofluorescent staining, cells grown on nanofibres were fixed in 4 % paraformaldehyde in PBS for 15 min, washed with 0.1 M PBS and treated with Triton X-100 (0.5 %) in PBS. After blocking with normal goat

serum (10 % in PBS) NSCs were incubated with antibodies to βIII-tubulin (1:200), nestin (1:2000), NF70 (1:200) or GFAP (1:200) diluted in PBS containing 1% BSA and Triton X-100 (0.5 %). This was followed by incubation in secondary goat anti-mouse IgG antibody conjugated with Alexa-Fluor 594 (1:400) or goat anti-rabbit IgG antibody conjugated with Alexa-Fluor 488. The nuclei were visualised using DAPI (1:200). Fluorescent images were acquired by LSM 810 DUO laser scanning confocal microscope (Zeiss).

The cell metabolic activity, which demonstrates the cell surviving on tested samples and is regarded as an indirect marker of the number and proliferation activity of cells, was estimated spectrophotometrically on day 6 after cell seeding, A conversion of resazurin (Cat. No. R7017, Sigma-Aldrich) was used to measure metabolic activity of the cells which is considered as an indirect indicator of cell proliferation. The principle of this redox indicator assay is based on the colorimetric conversion of blue resazurin to pink resorufin which can be quantified by fluorescence or absorbance measuring. This reduction is brought about by the activity of mitochondrial enzymes in the viable cells. In brief, the stock resazurin solution (4mM) was added to DMEM without phenol red to a final concentration of 40 μM. The cells were rinsed with PBS and the resazurin solution was added to the cells in each well and incubated with the reagent for 3 hours at 37 °C. The absorbance was measured (Ex/Em = 530/590 nm) using the VersaMax ELISA microplate reader (Molecular Devices LLC, Sunnyvale, CA, USA). A background control (resazurin solution without cells) was subtracted.

5 RESULTS AND DISCUSSION

This thesis describes three different organosilanes in the form of fibres targeting regenerative medicine as a result of very complex research. Initial work with organosilanes was based on a commercially available precursor such as triethoxyphenylsilan (TEPS – **Figure 16a**), 1,4-bis(triethoxysilyl)benzene (BTESB – **Figure 16b**) or 4,4'-bis(triethoxysilyl)-1,1'-biphenyl (BTESBP **– Figure 16c**). Firstly, fibre formation from monosilylated TEPS and its bissilylated analogue BTESB were studied in different molar ratios to TEOS. Starting from 1 mol.% BTESB to 99 mol.% TEOS (**Figure 17**), the parameters were changed to final 50 mol.% : 50 mol.%. Higher ratios of organosilanes in the silica matrix were also studied, however without a suitable polymerization and formation of a long spinnable polymeric chain. With obtained information from FTIR observations combined with supramolecular engineering studies, another commercially available organosilane precursor was identified - BTESBP. This precursor was described in the literature in many forms and applications such as aerogel for the fields of heat preservation materials, heat insulation materials, waste gas treatment materials, wastewater treatment materials and catalysts or in the form of the sensor for electrochemical detection of dopamine [40]. In different forms it was also mentioned in drug delivery systems [145] or biosensors [146].

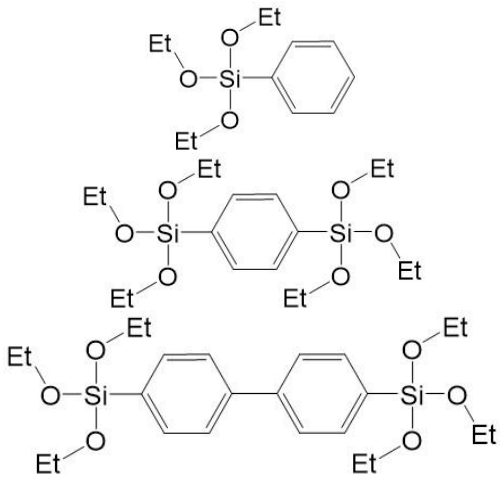

Figure 16 Structures of firstly investigated organosilanes precursors a) triethoxyphenylsilane (TEPS); b) 1,4-bis(triethoxysilyl)benzene (BTESB); c) 4,4'-bis(triethoxysilyl)-1,1'-biphenyl (BTESBP).

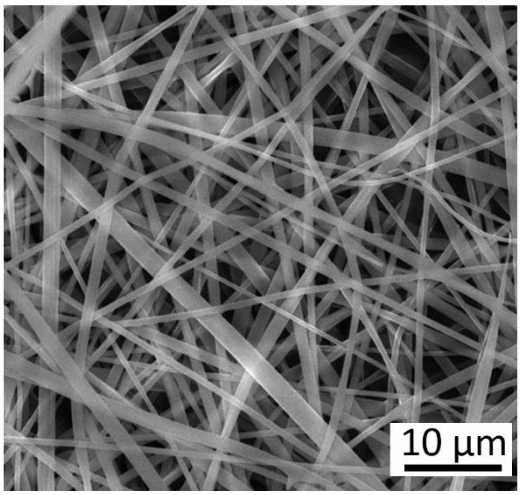

Figure 17 First created organosilane fibrous material via one-pot synthesis in 1 mol.% BTESB to 99 mol.% TEOS ratio.

By combining three independent fields of science (organic and organometallic chemistry, sol-gel chemistry, and electrospinning technology), it was possible to obtain unique results in the preparation of purely organosilane fibres. Such a concept resulted in patented technology *PS4427EP – Máková, Holubová, Kulhánková; Method for the preparation of a sol for the preparation of hybrid organosilane fibres by electrostatic spinning, the sol*

prepared by this method and hybrid organosilane fibres prepared by the electrostatic spinning of this sol. The true novelty of this patented work lies in the preparation of such fibrous materials, without the support of any spinnability enhancers or facilitators such as spinnable organic polymers, various types of surfactants, or non-polar organic solvents, which are in many cases highly toxic and also economically inconvenient.

This thesis presents three different types of bridged organosilanes which were considered suitable candidates for the fibre-making process applied in the field of soft tissue and neuro regeneration biomaterials. They are all based on APTES with different organic linkers with aliphatic (OBA), aromatic (BiTSAB) and heterocyclic (BiTSAP) disposition to compare different behaviour during the sol-gel process and fibre formation regarding the organics in the silica framework. The selection of precursors was guided by their utility in tissue engineering, due to the presence of -NH groups that offer binding sites for proteins, facilitating cellular adhesion and tissue integration. Additionally, the chosen precursors were evaluated by their structural features, which hold promise for imparting conductivity to the resulting materials.

5.1 Synthesis of bissilylated bridged organosilane precursors

All precursors discussed were synthesised by the already mentioned procedure with a yield of more than 65 wt.% (OBA) and more than 90 wt.% (BiTSAB, BiTSAP). After the synthesis and purification, the structure of all precursors was analysed using ^{1}H (**Figure 18, S1 and S2**), and ^{13}C (**Figure S3-S5**) liquid state NMR. Thermogravimetric decomposition was evaluated to define the thermal stability of the synthesised precursor to set the appropriate processing parameters of sol-gel postproduction.

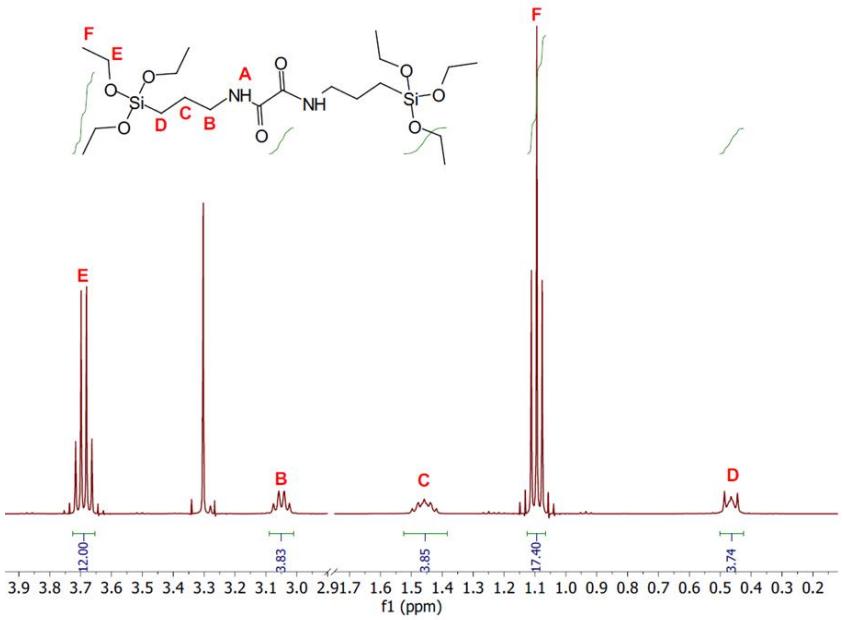

Figure 18 Spectrum of the ^{1}H liquid state NMR of the synthesised OBA precursor measured in DMSO-d_6.

Thermal stability of the precursors was measured in the temperature range from 25 °C to 650 °C in a nitrogen atmosphere with all samples tested (**Figure 19, S6 and S7**). The first leakage in all experiments occurs around 90 °C which corresponds to the evaporation of absorbed water and residual ethanol (proved by coupled FTIR – **Figure S8**). In the case of OBA precursor, the thermal decomposition (94.8 wt.%) occurs immediately after the water/ethanol evaporation. TGA of BiTSAB and BiTSAP precursors shows higher thermal stability together with the decomposition of different structures (detected as evaporation of dissociated ethanol or ethoxy groups). Decomposition of the organic part of the precursor (60 wt.% and 94 wt.%) occurs around 240 °C.

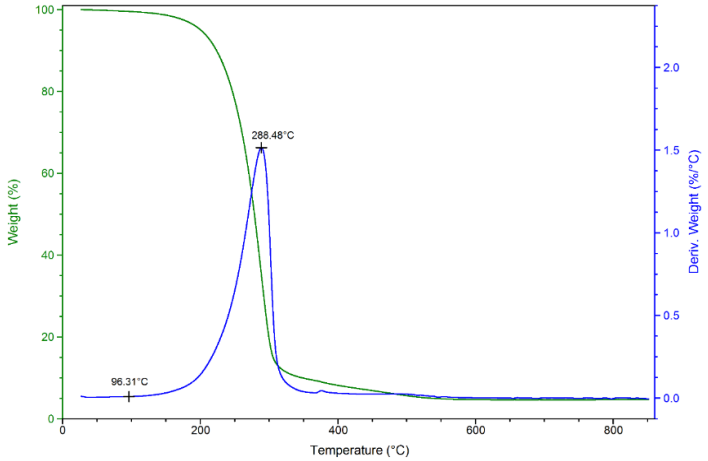

Figure 19 Scheme of thermal behaviour of synthesised precursor OBA.

According to the obtained measurements, the successful synthesis of all precursors was proved. Both ^{1}H and ^{13}C NMR analyses confirmed the fine structure of the OBA, BiTSAB and BiTSAP together with their purity (any other structure was detected in the spectra). TGA analysis proved lower thermal stability (maximum 90 °C) of OBA precursor when compared to aromatic (BiTSAB) and heterocyclic (BiTSAP) structures. Hence, this finding has to be taken into consideration when sol-gel processing parameters are set.

5.2 Sol-gel

Based on the previous experiments, to create a spinnable polymer using the sol-gel process, several processing parameters had to be considered for the fibre-making process. The most important are heating time and temperature, stirring time and intensity, form and amount of catalyst, nature of a solvent and its volume, Alc (alcohol/Si mol.%) and k (H_2O/Si mol.%) parameters.

After synthesis, precursors were stored in a round-bottom flask in a solid state at a temperature around 7 °C. To fully homogenise the precursor with solvent (ethanol), the flask was heated to 50 °C and stirred for several minutes. After first homogenization, demineralised water was required as a hydrolysis initiator and strong inorganic mineral

acid as a catalyst (HCl) was added to the mixture to adjust the pH of the mixture to ~ 2. After final homogenising, the prepared sol was heated and refluxed. The reflux parameters highly depend on the thermal stability of the precursor and the parameters of the used solvent.

However, the Alc parameter emerges as a particularly intriguing variable, especially when considering its incomplete description in prior research. High dilution introduces a new dimension, necessitating a careful balance in manipulating the Alc parameter to achieve the desired molecular architecture. Drawing from principles in supramolecular chemistry, where non-covalent interactions govern molecular assembly, this approach embraces the use of sterically large molecules in high molar ratios. Unlike conventional sol-gel strategies, which often involve low solvent concentrations and small molecular precursors. The deliberate incorporation of large molecules in concentrated solutions prompts a change of parameters, particularly the Alc parameter, within the sol-gel framework.

Table 7 Molecular weight of mentioned organosilanes.

	TESP	BTESB	BTESBP	OBA	BiTSAB	BiTSAP
MW [g/mol]	240.37	402.73	478.73	496.75	572.85	573.83

The initial step in this experimental setup involved setting the Alc parameter to levels previously proven successful in the formation of fibres using different organosilane precursors. It is important to acknowledge that the molecules used in the sol-gel process at the beginning of this problematics were sterically bulky, but the organosilanes introduced in this thesis are even larger (**Table 7**). Parameters of the sol-gels are noted in **Table 8**.

Table 8 Parameters of the sols with low Alc parameter.

	Silane : TEOS [mol. %]	Alc parameter	k parameter	Heating time [hours]	Bath temperature [°C]
OBA	100	40	2.01	120	60
BiTSAB	100	40	1.75	2	90
BiTSAP	100	40	2.03	2	90

Decision was made to recalibrate the Alc parameter on the base of the initial experiments supported by FTIR analyses together with our previous experiences, because they did not yield the expected success. Given the higher molecular weight of the precursors used in this thesis, the Alc parameter was now set as a ratio relative to the molecular weight regarding the ratio of the previously employed organosilane precursors. This adjustment reflects a nuanced understanding that the optimal Alc level might be influenced by the specific molecular characteristics of the large molecules under investigation for more

effective control over the synthesis process. Redefined parameters of the sol-gels are noted in **Table 9**.

Table 9 Parameters of the sols with Alc parameter calculated on the base of molecular weight ratios from previous experiments.

	Silane : TEOS	Alc parameter	k parameter	Heating time	Bath temperature
	[mol. %]			[hours]	[°C]
OBA	100	42	2.01	120	60
BiTSAB	100	48	1.75	3	90
BiTSAP	100	48	2.03	3	90

The redefined Alc parameter, tied to the molecular weight of the organosilane precursor, did not again yield the desired outcomes. However, as will be discussed in the following chapter, the polycondensation process progressed positively and partial spinnability of the sol (higher viscosity, spraying) was observed during the electrospinning attempt. Thus, the approach was once again adapted. To optimise conditions for the sol-gel process, the Alc parameter was increased beyond the previously established levels. As already mentioned above, inspiration came from the field of supramolecular chemistry, which employs the principle of high dilution. By elevating the Alc parameter, the research aims to enhance the space for molecular motion and reactivity of the sterically large molecules, potentially influencing the kinetics of the sol-gel reactions. In this study, the stoichiometry of prepared sols was around 1: 65 (silane: alcohol). For the preparation of hybrid nanofibres, these conditions were set experimentally. The parameters of these sols themselves are noted in **Table 10.** The positive outcome, marked by the successful formation of fibres, underscores the importance of parameter optimization and showcases the dynamic nature of scientific exploration.

Table 10 Parameters of the final sols.

	Silane : TEOS	Alc parameter	k parameter	Heating time	Bath temperature
	[mol. %]			[hours]	[°C]
OBA	100	68	2.01	144	60
BiTSAB	100	65	1.75	1	90
BiTSAP	100	65	2.03	1	90

To observe changes in the structure during the polymerization process several characterisation techniques can be considered to use. Most often NMR, FTIR, Raman, UV-VIS or mass spectroscopies are used. In the meticulous process of setting and adjusting the Alc parameter, the research employed a sophisticated monitoring technique - Fourier Transform Infrared Spectroscopy (FTIR). At each stage of parameter refinement, FTIR

served as a powerful analytical tool, allowing for real-time observation and analysis of molecular changes in the reaction system. This monitoring approach provided invaluable insights into the evolving chemical landscape, enabling us to assess the impact of varying Alc concentrations on the sol-gel reactions. FTIR spectra facilitated the identification of specific functional groups, elucidating the progress of hydrolysis and condensation reactions critical to the sol-gel process. The data obtained through FTIR not only guided the decision-making process in setting the Alc parameter but also offered a nuanced understanding of molecular transformations, ultimately contributing to the successful navigation of challenges and the achievement of desired outcomes in the preparation of fibres.

Using FTIR, the position of the specified peak typical for a defined structure can be observed. With this technique, the stability of the organic part of organosilanes can be observed, hence changes in characteristic areas for -OH, -OR, ≡Si-O-Si≡ can be also identified. The demonstrative spectra presented in the following chapter have been derived from monitoring the behaviour of the organosilane OBA throughout the sol-gel process. These spectra serve as a visual representation of the changes and interactions occurring within the OBA molecules as the sol-gel reactions progress in time from the beginning of hydrolysis to the gel time. The monitoring of OBA provides insights into the transformation of organosilane precursor into the desired spinnable sol, allowing a detailed understanding of the sol-gel chemistry and the evolution of molecular species during the process. For the measurement, a 50 µl droplet was placed on the crystal using an automatic pipette. However, because of the high dilution of the system, the alcohol had to be first evaporated so its intensity did not overwhelm the detection of other vibration bands. **Figure 20** is implemented as a demonstration of FTIR spectra of organosilanes for a better description of the following studies.

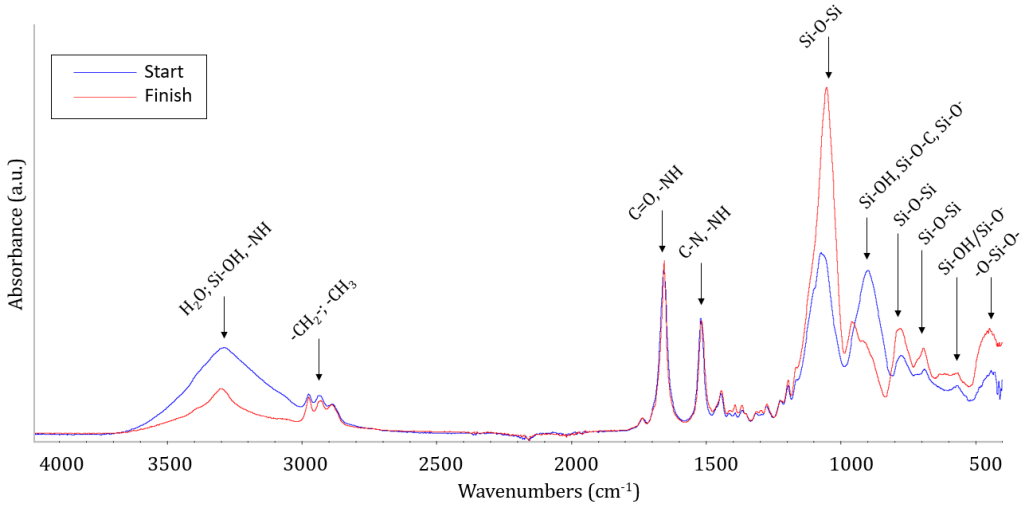

Figure 20 FTIR spectra of organosilane OBA at the beginning (blue line) and at the end (red line) of the sol-gel process as an illustration for FTIR studies with marked fingerprint regions of important bonds.

In the context of the study, the critical focus lies within the spectral range of fingerprint region - 1800 to 500 cm^{-1} (**Figure 21**) [147]. This specific frequency range is deemed most significant for the investigation, as it captures key vibrational modes and absorption features relevant to the analysis. Area 1800-1200 cm^{-1} corresponds to the specific organic functionality inherent in the utilized precursors. The progression of the sol-gel reaction does not alter the chemical nature of the organic spacer which is also proved by ssNMR of already created fibres. The range from 1800 to 500 cm^{-1} typically encompasses vibrational bands associated with silanes, offering valuable information about the chemical composition and interactions in the studied material. In this area, there are three strong absorptions identified by peaks at ~ 1060, ~ 763, and ~ 466 cm^{-1}.

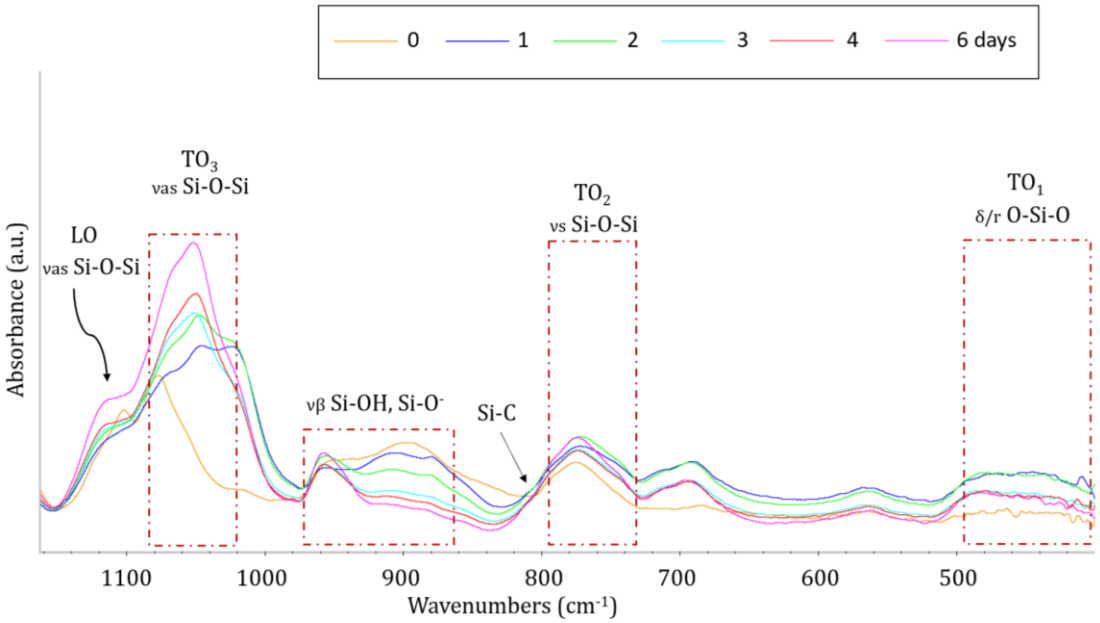

Figure 21 FTIR spectra of the different stages of the OBA precursor sol-gel process measured in days with a focus on the wavenumber's characteristics for silica materials (1400 – 400 cm^{-1}).

The lowest frequency mode at ~ 460 cm^{-1} is attributed to transverse-optical (TO_1) rocking motions, occurring perpendicular to the ≡Si-O-Si≡ plane, involving oxygen atoms that bridge two adjacent Si atoms (**Figure 22a,b**). This vibrational mode is characterised by the oscillation of oxygen atoms associated with the bridging bonds. Additionally, some cationic motion is coupled with this mode, indicating that the behaviour of the Si cations is intricately connected to the rocking motions of the bridging oxygen atoms. The coupling of cationic motion to this vibrational mode suggests a dynamic interplay between the silicon cations and the structural elements in the ≡Si-O-Si≡ network, providing valuable insights into the nature of the molecular interactions within the system [148].

Slightly under 800 cm^{-1}, a subtle band is detected, attributed to the transverse-optical (TO_2) symmetric stretching of the oxygen atom along a line that bisects the ≡Si-O-Si≡ angle (denoted as θ) (**Figure 22c,d**). This vibrational mode involves the symmetric

stretching of oxygen atoms with some simultaneous motion of Si cations. The presence of Si cation motion in conjunction with the TO symmetric stretching of oxygen highlights the coupled dynamics of the ≡Si-O-Si≡ network.

The largest absorption band at 1060 cm^{-1} is more intricate and likely conceals additional absorption bands. The strongest among them is the bridging transverse optical phonon mode (TO_3) of antisymmetric stretching of the siloxane bonds ≡Si-O-Si≡ (where oxygen atoms move in a direction parallel to silicon atoms, accompanied by significant Si cation motion). A weak shoulder toward higher frequencies suggests the longitudinal optical phonon mode (LO) of the bridging antisymmetric stretching of the ≡Si-O-Si≡. Similarly, a slight shoulder on the lower frequency side may be attributed to the stretching vibration of the silanol species (≡Si-OH; ~ 950 cm^{-1}) or the ≡Si-O^- (910 cm^{-1}) species (**Figure 22e,f**) [149,150]. Shoulder near above 800 cm^{-1} is attributed to the Si-C bond vibration, indicating the presence of an organic functionality connected to a silicon atom [148].

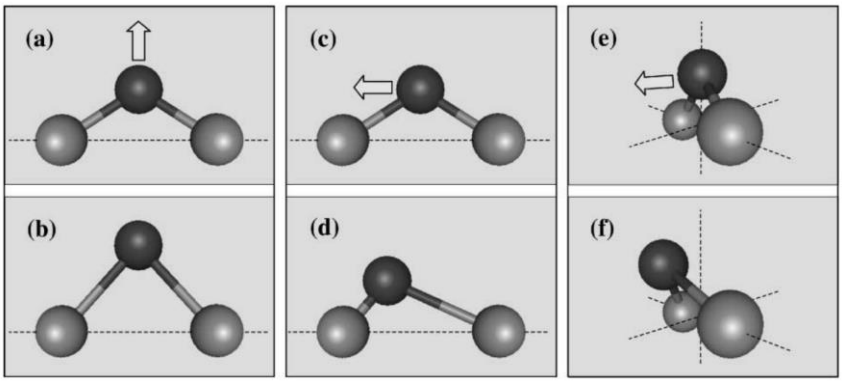

Figure 22 Schematic representation of the vibrational motions of oxygen atoms (dark) concerning the bridged silicon atoms (grey): symmetric stretching motion along the bisector of the Si–O–Si bridging angle (a) and (b), antisymmetric stretching motion parallel to the Si–Si line between the two bridged cations (c) and (d), rocking motion perpendicular to the Si–O–Si plane (e) and (f) [154].

It is evident that over time, the intensities of these ≡Si-O-C and ≡Si-OH bands decrease, signifying the successful removal of solvent and condensation alcohol by-products. During the process, the previously robust band 1100-1000 cm^{-1} can undergo a transformation into a single absorption peak at 1066 cm^{-1}, with an accompanying shoulder at around 1160 cm^{-1}. This peak corresponds to the longitudinal optical (LO) and transverse optical (TO) modes of the antisymmetric stretching vibration of the ≡Si-O-Si≡ bond, indicating a specific densification/evolution of the inorganic polysiloxane matrix in the system during the hydrolysis and polycondensation stage. The broad absorption band in the interval around 950 – 900 cm^{-1} (associated with the antisymmetric vibration of ≡Si-OH) diminishes over time but also evolves into well-depicted narrow absorption at around 950 cm^{-1} indicating uncondensed Si-OH species. This phenomenon is desirable because

encouraging a full polycondensation of all Si-OH groups into the 3D network is not suitable for fibre-making purposes (due to the low k parameter in the sol-gel process which causes suppression of hydrolytic reactions). Hence a small portion of unreacted Si-OH should remain in the spinnable sol proving the formation of linear and low-branched structures (as will be also further confirmed in the Si ssNMR spectroscopy of already prepared fibres).

Furthermore, the region between 763 and 466 cm^{-1} appears to obscure additional absorption features, possibly corresponding to the symmetric stretching vibration of ≡Si-O-Si≡ (siloxane rings) at around 680 cm^{-1} and the stretching of SiO_2 defects at around 580 cm^{-1}. Fingerprint regions for a comprehensive list of potential absorption frequencies for organosilanes are listed in **Table 11** [148,150,151].

Table 11 Characteristic vibration frequencies in FTIR spectra for organosilanes (cm^{-1}).

Peak position	Origin	Structural units
450 cm^{-1}	δ/r O-Si-O	-O-Si-O-
~ 580 cm^{-1}	νs Si-OH/Si-O^-	SiO_2 defects (NBOx)
~ 680 cm^{-1}	νs Si-O-Si	≡Si-O-Si≡ (BOx)
750 – 800 cm^{-1}	νs Si-O	≡Si-O-Si≡ (BOx)
~ 910 cm^{-1}	νβ Si-O	Free Si-O^- (NBOx)
950 – 1000 cm^{-1}	νβ/s Si-O	≡Si-OH (NBOx)
1050 – 1100 cm^{-1}	νas Si-O-Si; TO	≡Si-O-Si≡ (BOx)
~ 1100 cm^{-1}	νas Si-O-C	≡Si-O-C (NBOx)
1150 – 1200 cm^{-1}	νas Si-O-Si; LO	≡Si-O-Si≡ (BOx)

* νs – symmetric stretching vibration, νas – asymmetric stretching vibration, δ – deformation vibration (bending), νβ – in plane stretching vibration, r - rocking

The changes observed in the absorption peaks of Si-O-Si and Si-OH mentioned above can also be interpreted from the perspective of the growth and linking of the structural units within the silicon network, which extends through the oxygen atom. In this context, attention can be directed towards the concept of bridging oxygens (where oxygen leads to additional silicon) and non-bridging oxygens (where oxygen is compensated by, for example, an alkaline ion or proton H^+ resulting in Si-OH, etc.). To gain a comprehensive understanding of the ongoing reactions during the sol-gel process, it is imperative to closely monitor additional changes in the FTIR spectrum, specifically focusing on the detection of bridging (BOx – **Figure 23a**) and non-bridging oxygens (NBOx – **Figure 23b**).

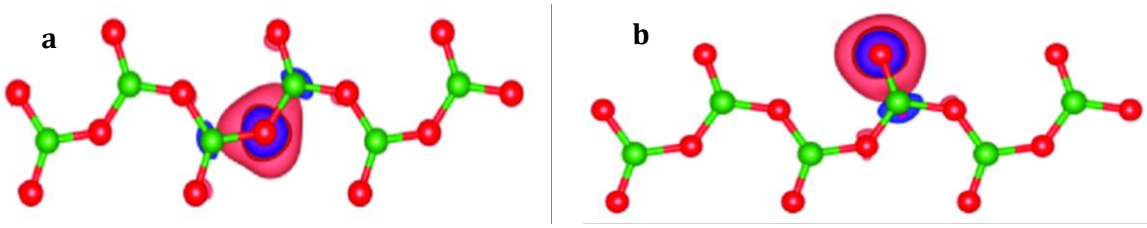

Figure 23 Scheme of bridging (BOx) and non-bridging (NBOx) oxygens [152].

This targeted analysis offers a more nuanced understanding of the molecular transformations occurring during the reactions, essential for unravelling the complexities of the sol-gel process. Bridging oxygens are involved in forming bonds between adjacent Si atoms, contributing to the network structure, while non-bridging oxygens are associated with terminal oxygen atoms in the network (**Figure 24**). This behaviour suggests a dynamic shift in the system, with a growing prevalence of bridging oxygen species and a corresponding reduction in non-bridging oxygen species. Such changes are indicative of ongoing reactions that contribute to the restructuring of the Si–O–Si network [148,150,153].

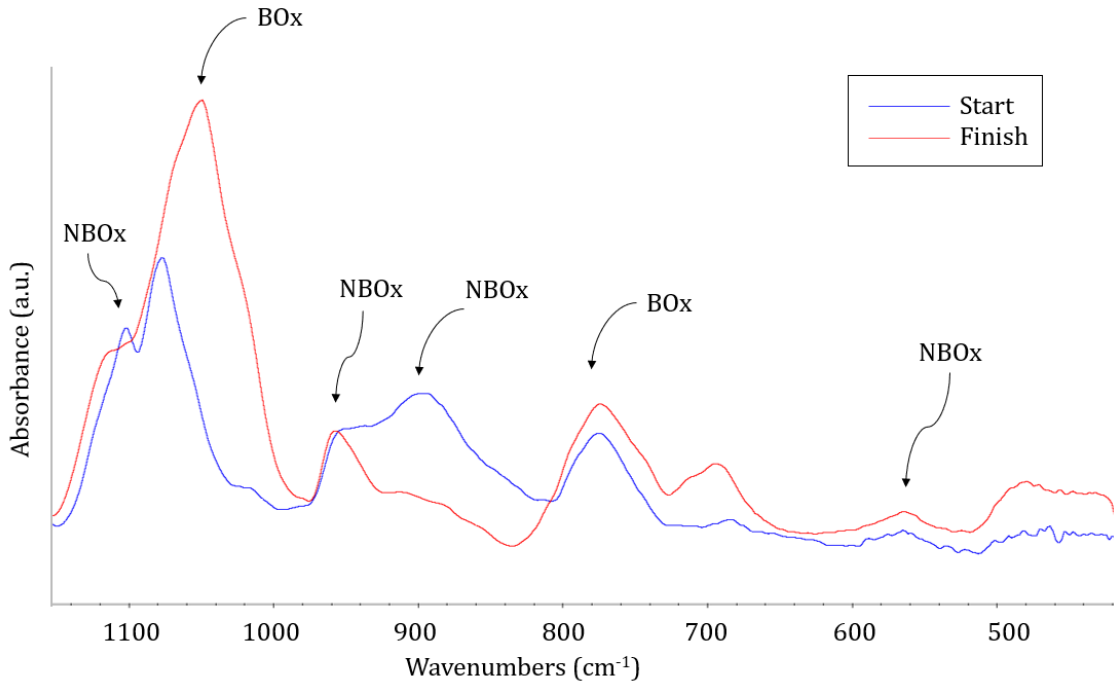

Figure 24 Evolution of (BOx) and non-bridging (NBOx) oxygens during the sol-gel process of OBA organosilane observed using FTIR.

Together with the intensity of BOx and NBOx, their shift in wavenumbers can occur and hence need to be evaluated. Shift towards higher wavenumbers (blue-shift) may suggest an increase in bond strength or a change in the local chemical environment that is affecting the vibrational frequency of the bonds. Conversely, a shift towards lower wavenumbers (red-shift) may indicate a weakening of bonds or alterations in the molecular structure [154]. The strongest red shift in the BO_x peaks is noticeable due to the higher steric hindrance of organic groups bonded directly to a silicon atom (Si-C) (**Figure 25**).

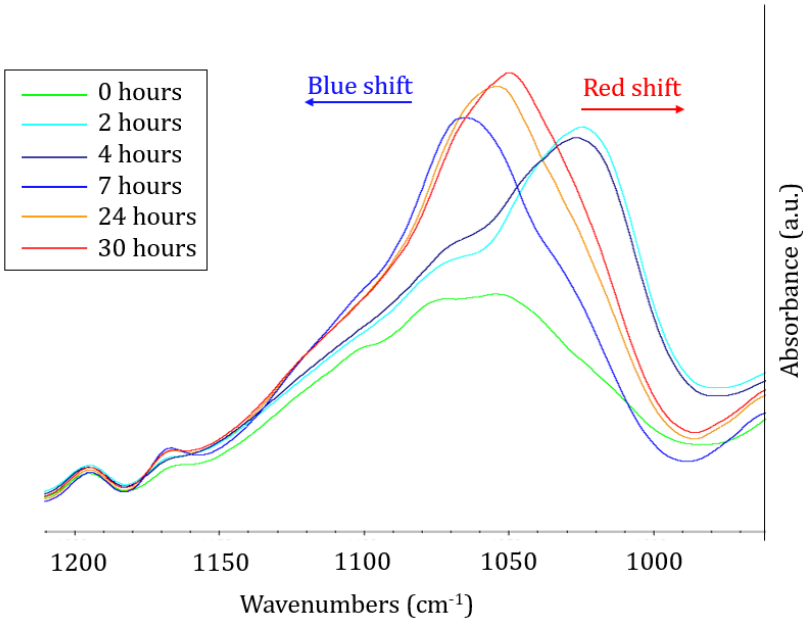

Figure 25 Representation of red shift and blue shift during the sol-gel process of organosilane OBA observed using FTIR.

The dynamic shifts in the BOx and NBOx peaks (**Figure 26**) across the spectra provide a visual representation of the evolving molecular environment during the sol-gel process. The changes in these oxygen species are indicative of the intricate hydrolysis and condensation reactions, illustrating the progression towards a more interconnected ≡Si–O–Si≡ network. In summary, a decrease in intensity of the peak at ~900 cm^{-1} over time is detected which has been previously described in acid-based systems for silanes, with the peak attributed predominantly to the absorption of ≡Si-OH, further indicating the subsiding hydrolysis due to the polycondensation process occurring [155,156]. This is also accompanied by a significant decrease in the intensities of the bands at around 3700 – 2800 cm^{-1} attributed to the H_2O/-OH and aliphatic (water and ethanol are products of the polycondensation reactions). Other significant changes can be observed within the area from 1200 – 700 cm^{-1} corresponding to the various Si bonds. Increasing and broadening of the peaks ~ 1155 and ~900 cm^{-1} describe the polycondensation reaction – forming of ≡Si-O-Si≡ bonds and decreasing of ≡Si-OH signals.

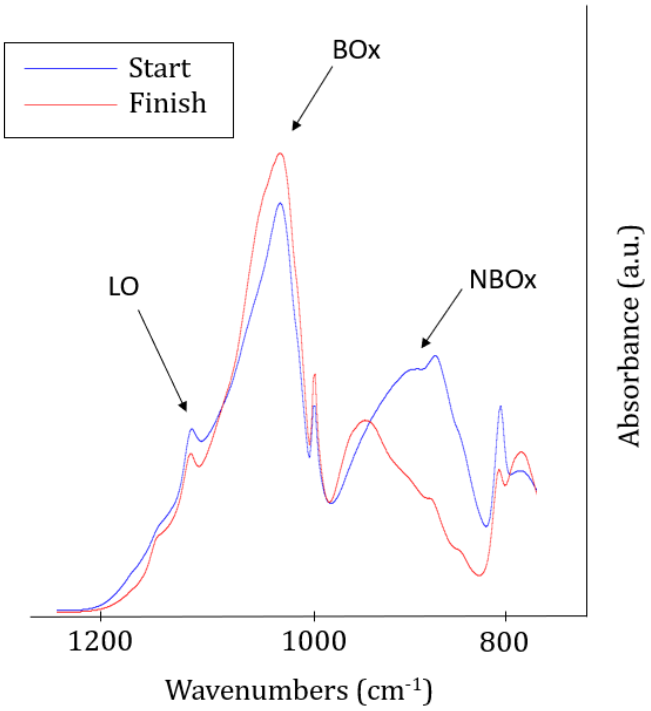

Figure 26 FTIR spectra of changes in the structure of OBA focusing on BOx peak (~ 1100 cm^{-1}) and absorption area NBOx (~ 950 cm^{-1}).

5.2.1 FTIR observations of OBA organosilane

As mentioned above, the temperature of sol-gel with OBA had to be set to 60 °C because of the thermal stability of the precursor. Hence, to see any changes in the structure, FTIR measurements were taken on a day's basis which allows for the tracking of changes with a high temporal resolution, enabling a detailed understanding of the system's behaviour.

The OBA sols *with low Alc* exhibit during the heating only a slight increase in the intensity of peaks in the monitored fingerprint region. As evident from **Figure 27**, the peak position ~ 1100 cm^{-1} (BOx) is almost at the same intensity level during the monitored time as well as the peak positioning ~ 760 cm^{-1} (BOx). A similar trend is noticeable in the absorption area ~ 950 cm^{-1} (NBOx) representing Si-OH and Si-O^- where the intensity remains unchanged over time, suggesting a significant presence of hydrolysed groups. However, these groups do not engage in bonding over time, likely resulting in numerous short chains with limited mobility for subsequent polycondensation reactions. There are also evident increases in the intensity of area ~ 450 cm^{-1} (O-Si-O) which indicates possible cyclisation of the structure and ~ 580 cm^{-1} (NBOx) which indicates SiO_2 defects in the forming structure. Spectra in 2D visualisation with a focus on the range 1700 – 400 cm^{-1} can be seen in **Figure S9**. When observing the ratio of BOx and NBOx intensities at low Alc levels, fluctuations are noticeable (**Figure 30**). This fluctuating pattern suggests a dynamic and

potentially unsuitable network formation during the sol-gel process, indicating variations in the formation of silicon-oxygen network structures. Hence, it becomes evident that the forming structure may not be suitable for successful spinning through electrospinning techniques, later confirmed by unsuccessful electrospinning attempts

In response to the observed complexities in the OBA sols with low Alc, an approach was taken *to increase the Alc parameter*. This increase was calculated considering a molecular weight ratio drawing from insights gained in previous successful experiments. Such modified OBA sol exhibits almost similar behaviour as with low Alc in the peak intensity position ~ 1100 cm^{-1} (BOx) and ~ 760 cm^{-1} (BOx) (**Figure 28**). While the likelihood of the formation of cyclic structures in the system still prevails, the less significant increase in intensity for these structures can be attributed to the molecules having more space for movement in the reaction flask, hence higher polycondensation of hydrolysed species can be observed. The expanded spatial freedom potentially allows for a more dynamic and diverse molecular arrangement, affecting the intensity changes in the FTIR peaks associated with cyclic structures. Despite the continued potential for cyclisation, the nuanced variations in intensity underscore the influence of spatial constraints on the sol-gel reactions. Spectra with a focus on the range 1700 – 400 cm^{-1} can be seen in **Figure S10**. When examining the changes in the ratio of BOx and NBOx intensities, fluctuations in these values are apparent. In the initial days of observation, a slight, linear increase is observed, suggesting the formation of a siloxane network by molecules in close proximity. However, as the size of the condensed molecules increases over time, their movement within the confined space becomes more challenging, leading to a prevalence of reverse reactions and a decrease in the intensity ratio.

Following the observed changes in the system, a decision was made *to further increase the Alc parameter by more than half of the original value*. This adjustment brought about notable changes in the structure of both BOx and NBOx. As evident from **Figure 29 and Figure S11,** significant changes in the peak position ~ 1100 cm^{-1} (BOx) and ~ 760 cm^{-1} (BOx) which are characteristic of the forming of Si-O-Si structure were detected. Moreover, there is an evident decrease in wavenumbers ~900 cm^{-1} (NBOx) and area ~ 450 cm^{-1} (O-Si-O) and ~ 580 cm^{-1} (NBOx) which indicates defects in the forming structure. Despite the observed decrease in NBOx intensity, it is notable that this absorption region has not entirely vanished. This observation further validates the accuracy of the set parameters for the sol-gel process. To create a sol suitable for successful spinning, the resulting molecular structure needs to consist of long but sparsely branched chains. By adjusting the water ratio to be sub-stoichiometric, hydrolysis is inhibited at the beginning of the sol-gel reaction, ensuring that the conversion from Si-O-C to Si-OH occurs slowly. This prevents the system

from having sufficient time for subsequent condensation to form a highly interconnected network, which would not be conducive to the fibre-making process. Observing the changes in the ratios of BOx and NBOx absorption areas reveals an almost linear increase over time. These observations further support the gradual condensation of molecules, characterised by the transformation of Si-OH to Si-O-Si, resulting in the formation of a continuous network. However, this network appears to be minimally branched, as a significant amount of silanol units is still detected in the system [148]. This observed behaviour suggests a dynamic and transformative reaction within the system. Dynamic alteration signifies a substantial restructuring of the Si–O–Si network, indicative of the intricate interplay of hydrolysis and condensation reactions within the sol-gel process. Such evolution in the molecular structure is a key indicator of the system's responsiveness to adjustments in the experimental parameters, particularly the Alc parameter followed by successful electrospinning and fibre production.

The observations mentioned above can be further supported by tracking the shifts in the defined BOx (**Figure 31a**) and NBOx (**Figure 31b**) absorption regions on the wavenumber axis. At low and MW Alc, the shifts in wavenumbers for both BOx and NBOx are minimal and do not exhibit any consistent trend in positioning. Some position changes are so subtle that they fall below the resolution capability of the device. However, a different behaviour is noted *at high Alc*. In this case, the absorption region for BOx demonstrates a notable shift towards lower wavenumbers (red shift). This shift corroborates the formation of a loose structure of siloxanes, indicating a less dense, more linear arrangement. Conversely, when tracking the position of the NBOx, a noticeable shift to higher wavenumbers – a blue shift, is observed which (from the Si-OH point of view) indicates a certain densification of the hydrolysed species in the structure, which again indicates a large number of uncondensed silanol units in the system and confirms the formation of a little branched, linear network. Such observation confirms a significant change in the structure of the organosilane, indicating a desirable network densification and effective removal of the solvent.

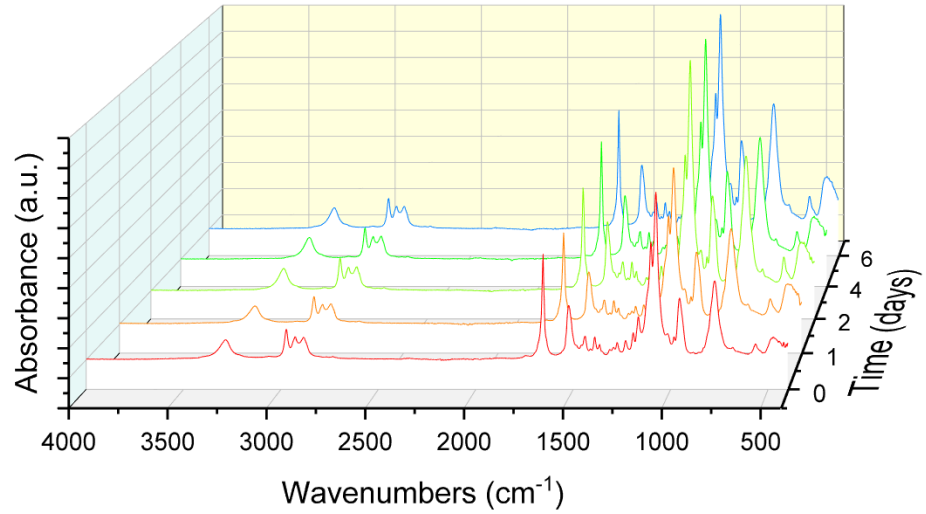

Figure 27 FTIR spectra of changes in the structure of OBA precursor during the sol-gel process with low Alc.

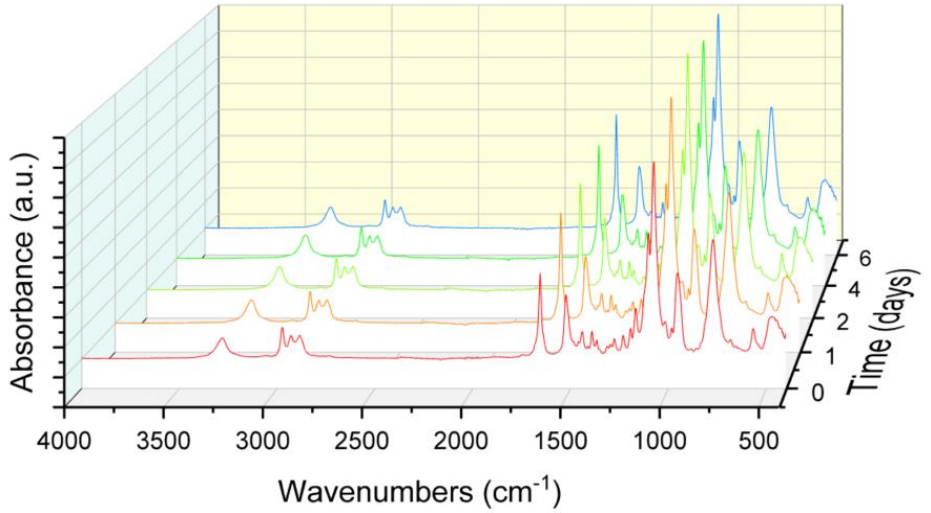

Figure 28 FTIR spectra of changes in the structure of OBA precursor during the sol-gel process with calculated Alc according to their MW.

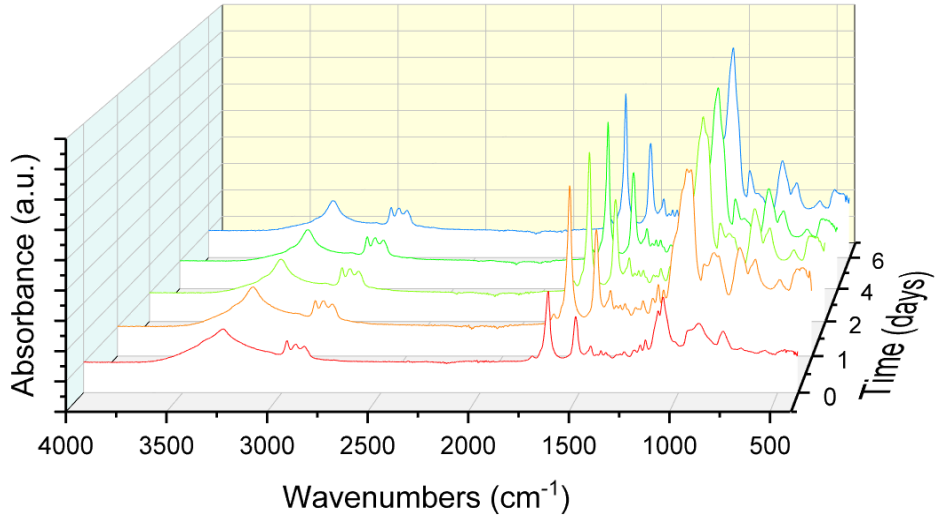

Figure 29 FTIR spectra of changes in the structure of OBA precursor during the sol-gel process with high Alc.

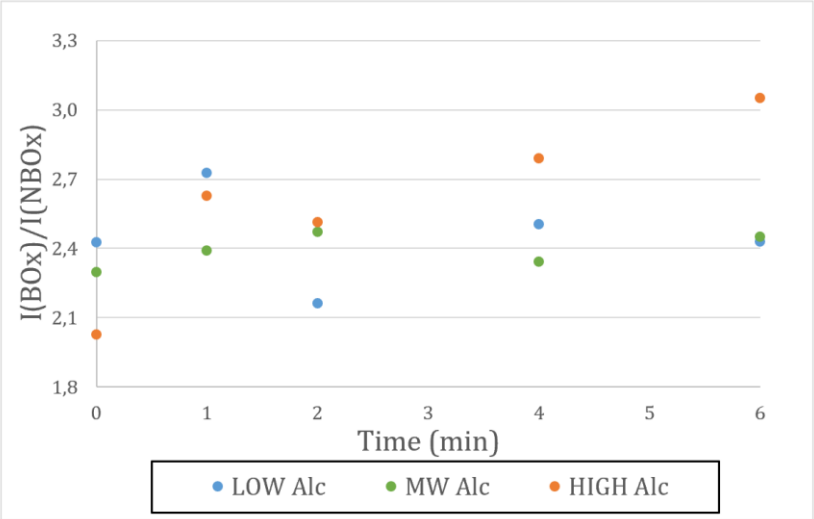

Figure 30 Changes in intensity of the ratio BOx/NBOx bands as a function of time during the sol-gel process of OBA.

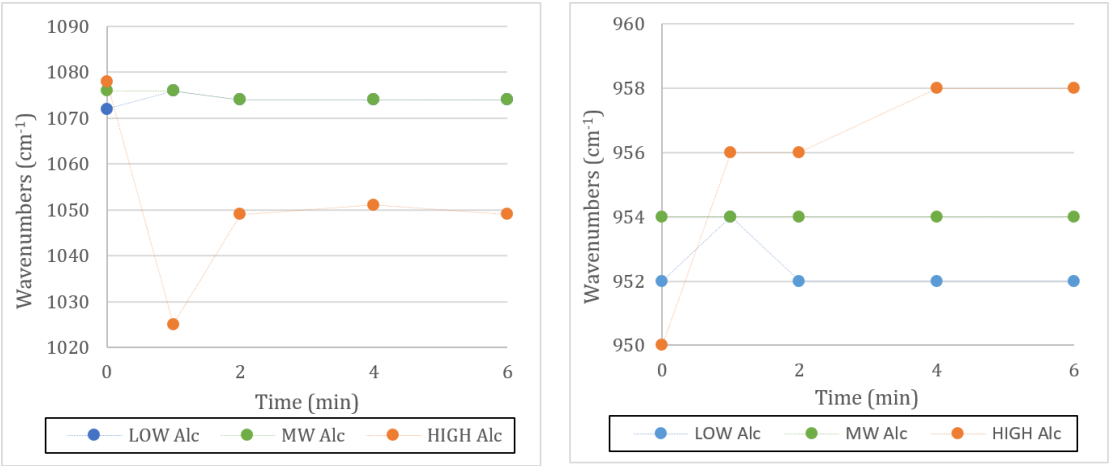

Figure 31 Changes of the BOx band position (a), changes of the NBOx band position (b) during the sol-gel process of OBA.

5.2.2 FTIR observations of BiTSAB organosilane

The enhanced thermal stability of the BiTSAB and BiTSAP precursors has facilitated an increase in the temperature during the sol-gel process to 90 °C. The improved stability of the precursors at higher temperatures likely contributes to a more efficient conversion of the starting materials into the desired structure and the system was observed on a minute basis.

In the FTIR analysis of the system *with low Alc* of BiTSAB (**Figure 32**), only minor changes were observed. Structure during the sol-gel process showed similar behaviour to BiTSAP when after a few minutes of the reaction initiation small particles at the bottom of the flask were observed. The lack of observed changes in the Si-O-Si, Si-OH, or Si-O-C regions within the system can likely be attributed to the rapid hydrolysis of the system (as evident from the sharp Si-OH peak at time 0), followed by accelerated condensation. As a result, short, intensely cross-linked structures likely formed early in the reaction and precipitated out of the system. During FTIR monitoring, only the liquid part of the system was analysed,

leading to a gradual decrease in the amount of organosilane precursor present. While hydrolysis continued rapidly, leading to a constant Si-OH region, condensation into Si-O-Si structures occurred concurrently but without observable changes in the Si-O-Si (BOx) region. Observations of particles precipitating out of the solution during the sol-gel process indicated a significant reduction in the number of molecules remaining in the solution, with only a minority participating in network formation. Additionally, the separation of organosilane molecules due to the loss of precursor increased the available space, hindering the formation of a sparsely branched network. Spectra with a focus on the range 1700 – 400 cm^{-1} can be seen in **Figure S12**. This behaviour is further supported by the observation of minimal changes in the positions of BOx and NBOx, with negligible deviations noted and failed electrospinning attempts (**Figure 35**).

Even within *the Alc parameter calculated as a ratio of the molecular weight* from a previously used organosilane precursor, the system did not yield in successful preparation of fibres. While FTIR analysis (**Figure 33**) detected changes in the ≡Si-O-Si≡ absorption area (BOx), the NBOx area (~ 950 cm^{-1}; Si-OH and $Si-O^-$) suggest a process of transformation within the system. However, this transformation has not led to a distinct peak, indicating that the changes in this region are more nuanced and complex. Alongside these changes, the intensity of area ~ 450 cm^{-1} (O-Si-O) which indicates possible cyclisation of the structure and ~ 580 cm^{-1} (NBOx) which indicates SiO_2 defects in the forming structure suggests the existence of additional structural elements within the system. These elements may include defects and cyclic units, which contribute to the overall composition and behaviour of the material. Analysis of the ratio of BOx and NBOx intensities supports this observation (**Figure 35;** spectra with a focus on the range 1700 – 400 cm^{-1} in 2D format can be seen in **Figure S13**). While there is an overall trend of a nearly linear increase in intensity ratios, a slight fluctuation is noticeable within the initial 30 minutes. This fluctuation suggests a significant influence of back reactions during the early stages of the process. As a result, the formed system may contain defective areas that hinder the development of a sol suitable for fibre formation.

Across the spectra of BiTSAB *with high Alc*, distinct changes in BOx and NBOx are meticulously recorded (**Figure 34**). A significant increase in the intensity of the ~1100 cm^{-1} area (corresponding to BOx; Si-O-Si bonds) was observed, nearly doubling its intensity over the monitored time period. Similarly, a notable increase in intensity was observed in the 750-800 cm^{-1} region (also associated with BOx, Si-O-Si bonds). Conversely, evidence of intensive polycondensation of the network was indicated by a decrease in the silanol region at 950 cm^{-1} (NBOx; Si-OH and $Si-O^-$) and a minimal presence of defects in the SiO_2 structure. This behaviour mirrors the observations made for the OBA precursor. The notable increase

in Si-O-Si absorption area suggests the formation of a siloxane network. However, the presence of hydrolysed silanol units persists, indicating that while the siloxane network formed is continuous, it is also minimally branched. These alterations consistently underscore the polycondensation of silicon species, contributing to the formation of a suitably polycondensed siloxane structure accompanied by the successful formation of hybrid fibres in 100 mol.%. Presenting the spectra of the initial and final stages of the sol-gel reaction of organosilanes in systems with high Alc parameters in a 2D format (**Figure S14**) enhances clarity and facilitates a more detailed analysis. When monitoring the formation of the organosilane structure according to the changes in intensities of BOx a NBOx, with high Alc similar behaviour was observed as in the system with MW Alc. As the intensities of BOx and NBOx were tracked, a linear increase was evident, signifying the formation of a suitable network for subsequent fibrous morphology.

The observations mentioned above can be further supported by monitoring the shifts in the defined BOx (**Figure 31a**) and NBOx (**Figure 31b**) absorption regions. *At low Alc*, the shifts in wavenumbers for both BOx and NBOx are minimal and do not exhibit any consistent trend in positioning. Some position changes are so subtle that they fall below the resolution capability of the device. By observing the system *with the MW parameter*, a notable shift in molecular behaviour became apparent. The shifts in positions further validate the effectiveness of the higher dilution as a modification of the parameters. A red shift in BOx indicates a loose structure of siloxanes, indicating a less dense, more linear arrangement. Conversely, a slight blue shift observed in NBOx suggests subtle alterations in molecular arrangements with crowding of the hydrolysed species in the structure, which again indicates a large number of uncondensed silanol units in the system and confirms the formation of a little branched, not-well-condensed linear network. Within the BiTSAB system *with a high Alc parameter*, the positions of the observed peaks trended in different directions, with BOx exhibiting a firstly red shift (after the first observed timepoint), followed by an intense blue shift (to the end of the measurement). Also, NBOx displaying a blue shift. The blue shift within the BOx indicates the thickening of the siloxane network. This shift suggests ongoing polycondensation reactions within the sol-gel process. If these reactions were to persist, leading to further cross-linking of the system, it would hinder the preparation of fibres. These findings contribute to a deeper understanding of monitoring the sol-gel process of organosilanes through FTIR analysis. By comparing the OBA and BiTSAB systems, it becomes evident that the presence of silanol groups within a certain range is crucial for achieving a fibre-making sol and further generation of fibres. However, the precise quantity of Si-OH groups within the system can vary within a defined interval. The assertions regarding the linking of silanol units are substantiated by ssNMR

(chapter 5.4.2) of the formed fibres, which were monitoring the degree of polycondensation with siloxane T^n units confirming a notably higher degree of polycondensation in BiTSAB fibres compared to OBA.

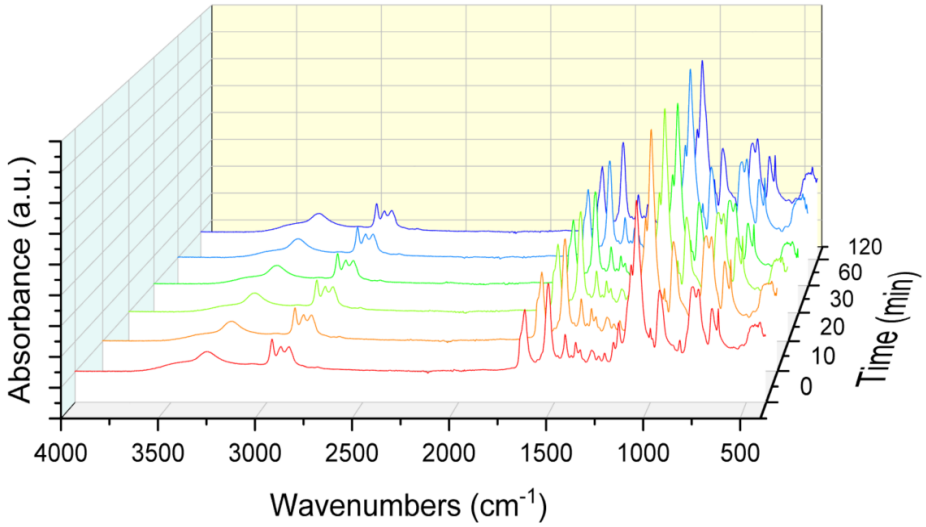

Figure 32 FTIR spectra of changes in the structure of BiTSAB precursor during the sol-gel process with low Alc parameter.

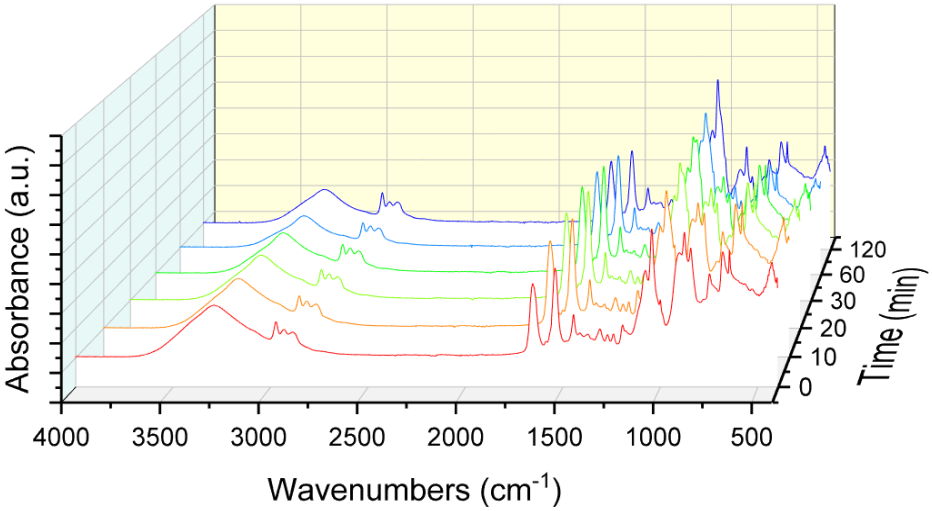

Figure 33 FTIR spectra of changes in the structure of BiTSAB precursor during the sol-gel process with Alc parameter calculated from molecular weight ratios from previous experiments.

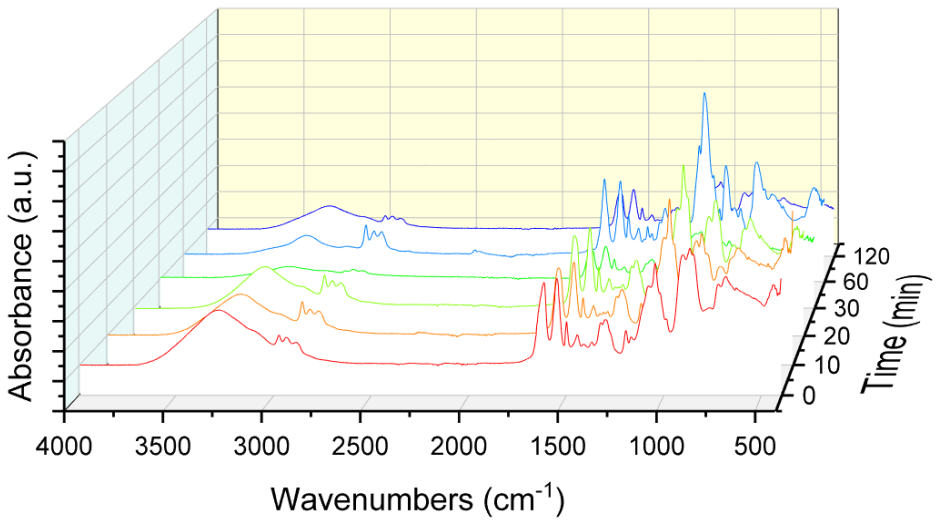

Figure 34 FTIR spectra of changes in the structure of BiTSAB precursor during the sol-gel process with high Alc.

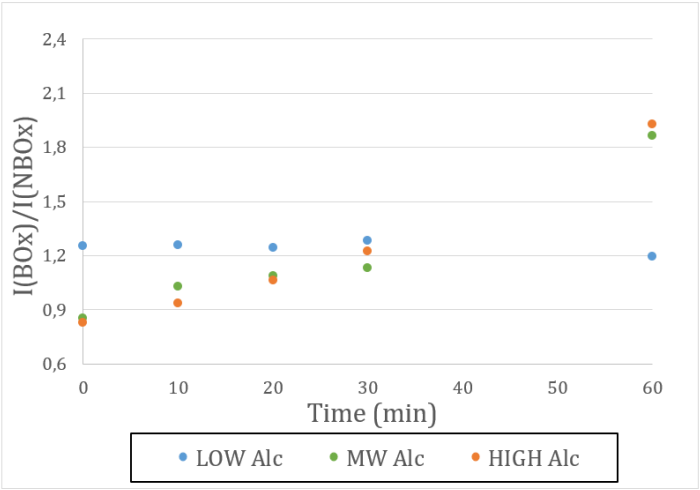

Figure 35 Changes in intensity of the ratio BOx/NBOx bands as a function of time during the sol-gel process of BiTSAB.

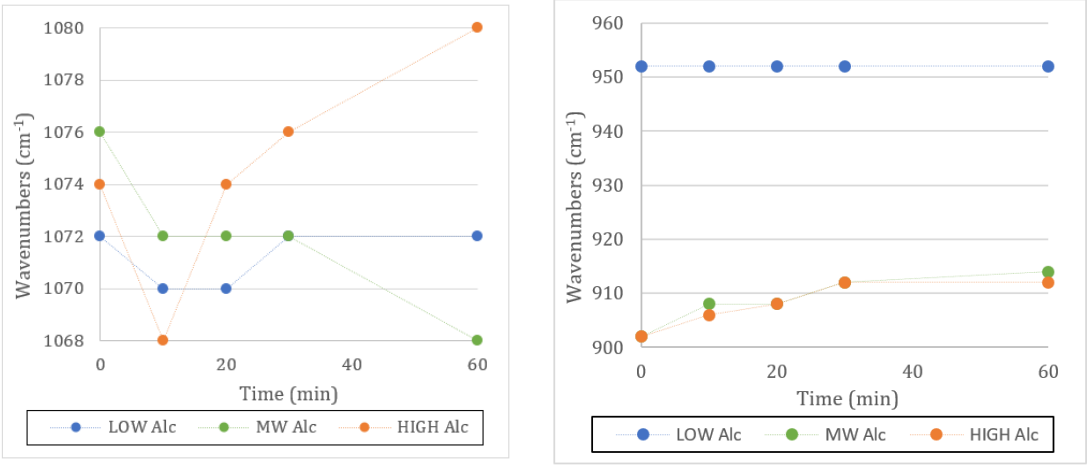

Figure 36 Changes of the BOx band position (a), changes of the NBOx band position (b) during the sol-gel process of BiTSAB.

5.2.3 FTIR observations of BiTSAP organosilane

In the FTIR analysis of the system *with low Alc* in the BiTSAP system, minor changes were observed as well as in the BiTSAB sol. Both structures during the sol-gel process showed similar behaviour when after a few minutes of the reaction initiation precipitation of small particles at the bottom of the flask was observed. Monitoring the FTIR spectra (**Figure 37 and S15**), an increase in BOx peak ~1100 cm^{-1} can be observed indicating the slow formation of the siloxane network. A decrease in the intensities of Si-OH and Si-O-C species can be also observed. Nevertheless, the intensity of this absorption band remains high even after 60 minutes. Contrary to the observations made for the precursor BiTSAB, slower hydrolysis is evident with the precursor BiTSAP. This is indicated by the gradual decrease in intensity of the absorption region around ~ 950 cm^{-1}, without an immediate formation of a single sharp absorption band. This disparity in hydrolysis rates corresponds to the differing behaviour of the systems in the formation of the siloxane network when the ratio of BOx and NBOx shows an almost linear increase (**Figure 40**). This behaviour could be attributed to a significant amount of the precursor being expelled from the system during the first minutes, thereby behaving as having gradually increased Alc which resulted in defected structure (high absorption in 750 – 460 cm^{-1}) and failed electrospinning attempts.

The BiTSAP system *with MW Alc* (**Figure 38 and S16**) parameters exhibits inconsistency in its behaviour over time in the absorption area BOx ~1100 cm^{-1}. There are visible fluctuations in the spectra describing the likely reverse reactions in the system. Although there was a noticeable decrease in the NBOx absorption regions ~950 cm^{-1} (Si-OH) and ~750 cm^{-1} (Si-O-C) and a decrease in the region 760 - 460 cm^{-1} (indicative of defective SiO_2), the parameters configured in this experimental setup did not yield successful spinning of the sol. Despite observed changes in the system, such as an increase in viscosity (to 20 mPas from the original 8 mPas), no interactions conducive to needle electrospinning were observed during experiments. This system displays also inconsistency in its behaviour over time concerning the ratio of BOx and NBOx intensities. These ratios do not exhibit a consistent trend of increase or decrease but oscillate over time. Within the sol-gel reactions, back reactions can occur, and these uncontrolled back reactions were probably captured in the spectra monitoring of the organosilane within the system *with MW Alc.* When examining the positions of the BOx and NBOx absorption regions, it becomes evident that these changes in the emerging structure occur, supporting the hypothesis of a notable influence of back reactions.

While preparing fibrous materials from the organosilane precursor BiTSAP *with high dilution* (**Figure 39 and S17**), the initial parameters were identical to those used in the successful preparation of fibres from the precursor BiTSAB. However, upon monitoring the

FTIR spectrum of the BiTSAP precursor under high dilution conditions, notable changes were observed in the monitored FTIR absorption regions compared to the BiTSAB precursor. The observation of the absorption region at 1100 cm^{-1} (BOx, Si-O-Si) reveals a notably high intensity of this band immediately from the beginning of the sol-gel reaction. This phenomenon may be attributed to the high reactivity of the system, which is exceptionally sensitive to environmental conditions. During the FTIR analysis, when excess ethanol needs to be removed from the measured droplet, the measurement can be influenced by the polycondensation reactions that may occur directly in the device. When examining other absorption regions, a distinct trend of polysiloxane network formation becomes apparent. Particularly in the regions of ~950 cm^{-1} (NBOx, Si-OH and $Si-O^-$) and ~800 cm^{-1}, significant changes occur during the sol-gel reaction, indicating active hydrolysis followed by condensation in the system. Concurrently, there is a reduction in absorption in the area of the defective SiO_2 network, suggesting the formation of a siloxane network. Nevertheless, analysis of the FTIR spectrum reveals that the condensation in the system is not as pronounced as observed with the BiTSAB precursor. There is an increasing presence of remaining silanol/ethoxy groups in the system, indicating incomplete condensation reactions. Subsequent confirmation of a lower representation of polycondensation reactions within BiTSAP was obtained through NMR analysis of electrospinned fibres. Involves the calculation of the percentage of unreacted ethoxy groups. Results showed that 3.2% and 4.6% of unreacted ethoxy groups were present for BiTSAB and BiTSAP, respectively. The parameters utilized for the BiTSAP precursor were established based on the successful fibre formation of the previously examined BiTSAB precursor. While some previously noted trends were not observed, the formation of fibre structures was achieved successfully. Monitoring the intensities of BOx and NBOx revealed a significant increase during the initial minutes, which remained relatively stable except for a fluctuation at 20 minutes.

The observations mentioned above can be further supported by monitoring the shifts in the defined BOx (**Figure 41a**) and NBOx (**Figure 41b**) absorption regions. Within the system with low Alc, no significant changes in BOx were observed within the first 20 minutes. However, at the 30-minute mark, there was a notable shift towards higher wavenumbers (blue shift), indicating the formation of a highly branched structure (which explains the subsequent falling out of the sieved particles from the system). Subsequently, no further changes in the BOx position were noted. In contrast, while monitoring the NBOx positions, no significant shifts in wavenumbers were observed, although there was a subtle trend indicating a slight increase towards higher wavenumbers. Nevertheless, these changes were minimal and could be considered negligible. This behaviour closely resembles

that observed in the previous BiTSAB system. The trend of precipitation of strongly condensed structures was consistent, likely coming from inadequate space within the reaction mixture. Consequently, the restricted molecular mobility hindered the optimal binding site search, leading to the formation of these densely packed structures. In the system with calculated MW Alc, there was a marked increase in the ratio of BOx and NBOx intensities, accompanied by a significant blue shift indicating structural organization together with a high degree of cross-linking. Subsequently, the impact of back reactions became apparent, leading to a decrease in the intensity of BOx and NBOx and a red shift suggesting a transition to defective, poorly branched short chains. However, in subsequent time intervals, the intensity of BOx and NBOx increased again, remaining consistent thereafter until the end of the measurement. Similar trends were observed for the positions of BOx at the high Alc system. In the initial stages of the reaction, a notable shift in the position of BOx towards higher wavenumbers is evident, suggesting the formation of a densely packed representation of siloxane units in the structure. However, after approximately 10 minutes, the BOx absorption region returns to its original position, indicating a subsequent loosening of bonds, akin to a red shift. This position persists for the remainder of the monitoring period. A similar trend is observed when tracking the position of NBOx. This sensitivity to temperature fluctuations in the reaction bath, heated to 90 °C, is likely reflected in the observed behaviour during the initial time interval before the system stabilizes entirely.

Considering the identical conditions set for both precursors and the distinct behaviour of the system concerning polycondensation reactions, future studies must account for not only the molecule's molecular weight but also its structural characteristics. The presence of nitrogen in the heterocyclic BiTSAP structure exerts a significant influence on the formation of the siloxane network, likely due to its partial charge effect. While the BiTSAP system was eventually spun successfully, in more complex structures, this effect may be even more pronounced and could potentially lead to failure. Hence, thorough investigation and understanding of the molecular structure's impact on the sol-gel process are imperative for future research endeavours.

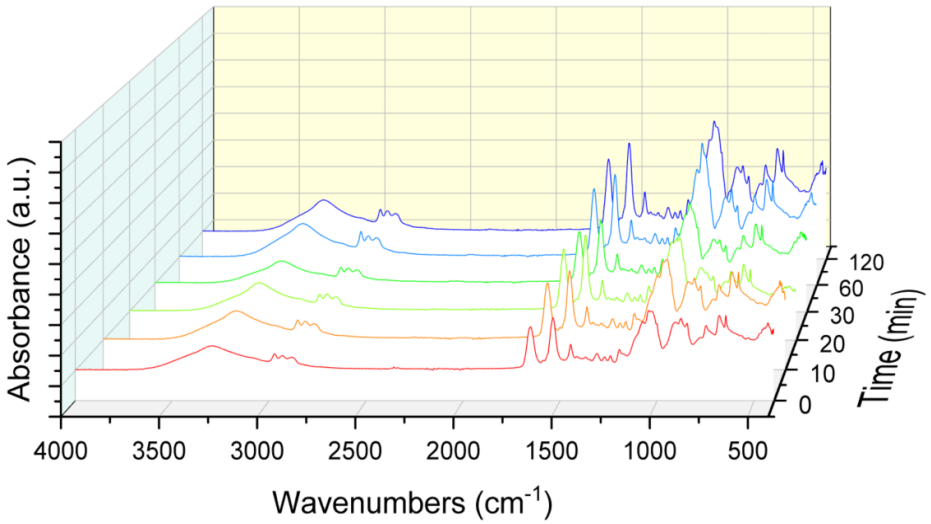

Figure 37 FTIR spectra of changes in the structure of BiTSAP precursor during the sol-gel process with low Alc parameter.

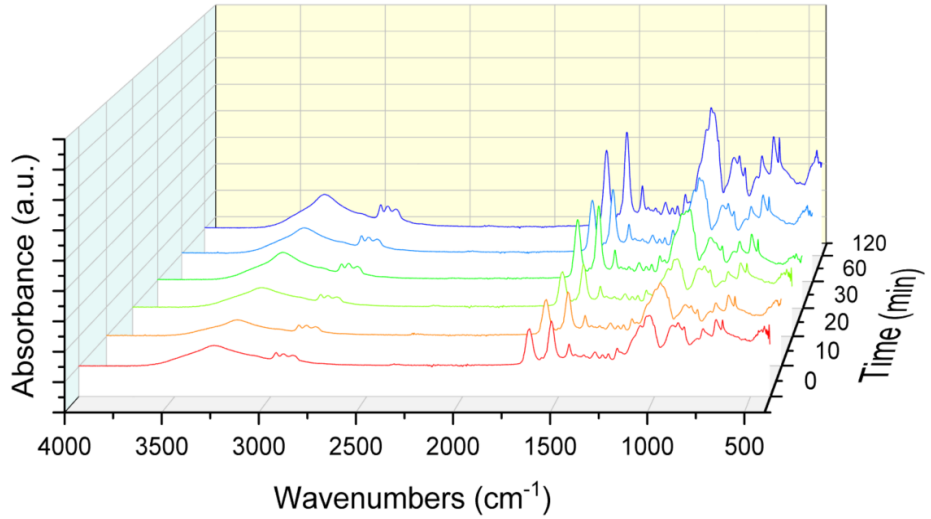

Figure 38 FTIR spectra of changes in the structure of BiTSAP precursor during the sol-gel process with Alc parameter calculated on the base of molecular weight ratios from previous experiments.

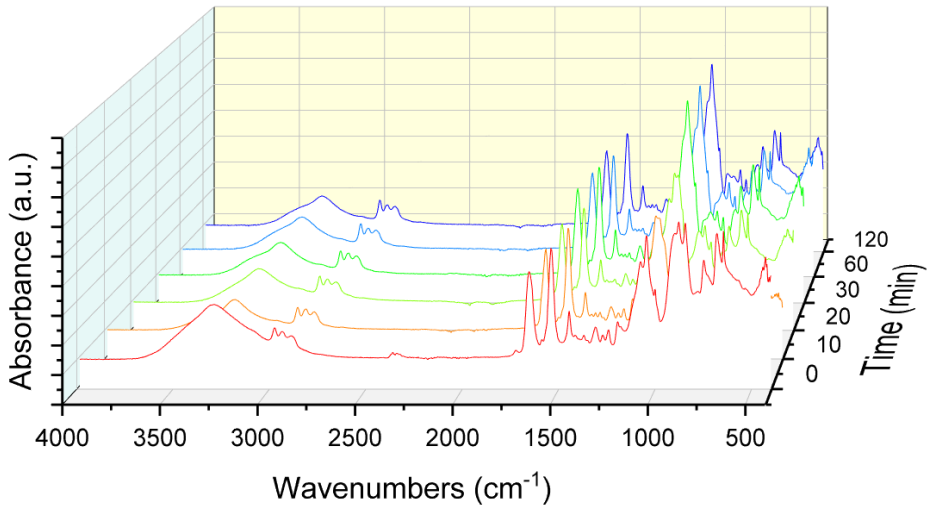

Figure 39 FTIR spectra of changes in the structure of BiTSAP precursor during the sol-gel process with high Alc.

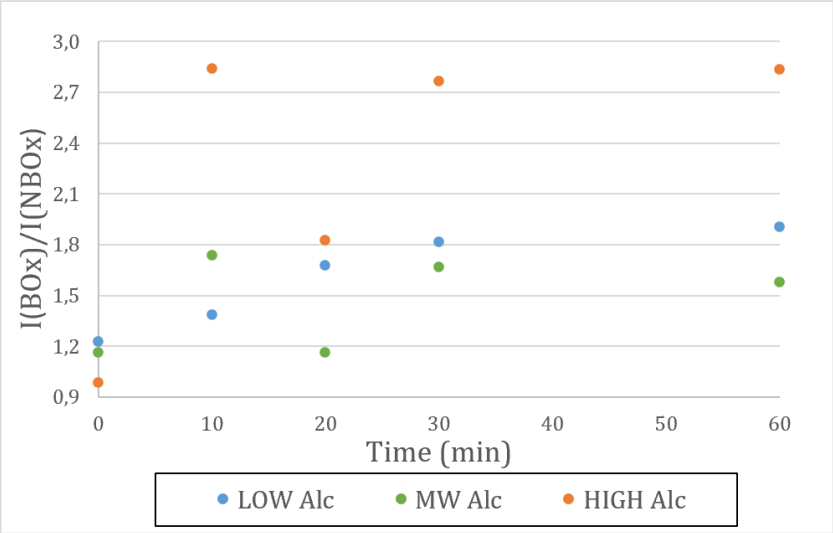

Figure 40 Changes in intensity of the ratio BOx/NBOx bands as a function of time during the sol-gel process of BiTSAP.

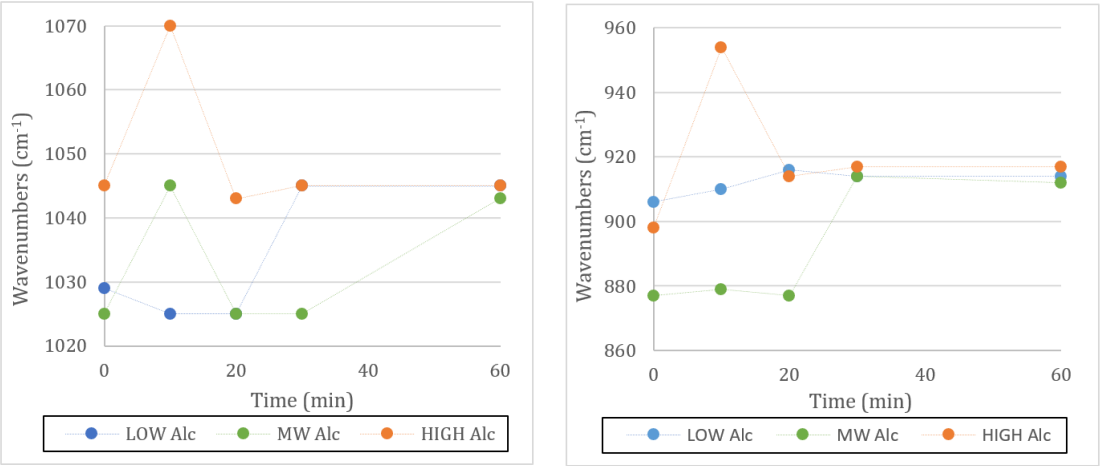

Figure 41 Changes of the BOx band position (a), changes of the NBOx band position (b) during the sol-gel process of BiTSAP.

The measurements of structural changes during the sol-gel process reveal certain trends; however, the complexity of the process and the influence of numerous factors make stabilization challenging. The sol-gel process is intricate, and influenced by variables such as reaction kinetics, temperature, concentration, and the nature of precursors. The dynamic nature of these factors over an extended period poses challenges to stabilization. As a result, it can be inferred that while FTIR measurements are valuable in providing insights into molecular changes, they cannot stand alone. A combination with other measurement techniques evaluating chemical nature becomes essential for a more comprehensive understanding.

Another method to observe condensation reactions is nuclear magnetic resonance (NMR). Within this method, the real structure of forming polymeric materials can be detected in the form of Q, T, D and M species. T^1, T^2, and T^3 units can be observed (**Figure 42**). However, a significant drawback is the need for relatively long measurement times,

which can pose challenges when studying systems that undergo rapid or dynamic changes. The dynamic nature of the system may outpace the time scale of NMR measurements, making it less suitable for capturing real-time or quickly evolving processes.

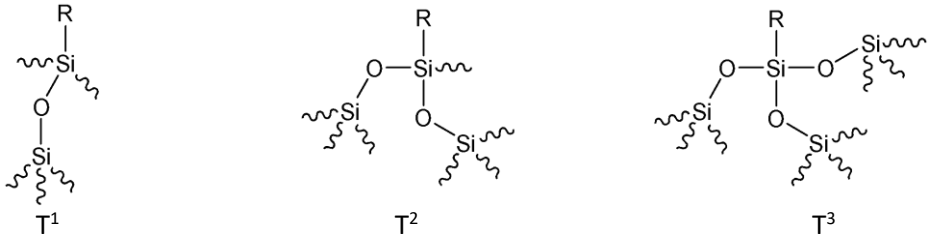

Figure 42 Structure of the siloxane structure marked as T^1, T^2 and T^3 units

Above mentioned sol-gel process is set in high dilution, which is not common in classic sol-gel chemistry. It was undertaken due to the sterically huge organic component of the organosilane. However, before the electrospinning process, the viscosity of the sol has to be modified to a spinnable capacity. Within insufficient surface tension, electric forces during the electrospinning would not be enough to withdraw fibres. For these reasons, the viscosity of the sol needs to be in a specific range which can be achieved by distillation of the solvent.

The final sol, concentrated to the suitable viscosity, contains linear, low-branched macromolecules of the organosilane matrix. The matrix still contains molecules of an alcohol-based solvent water and a trace amount of a catalyst. However, after the subsequent electrospinning process, they in the majority evaporate. Viscosity was determined as a crucial parameter in obtaining smooth homogenous fibres. When the viscosity is too low, the spinning process did not occur and films were detected on the collector or inhomogeneities distributed along the fibre were observed. When the viscosity is too high, the structure grows further in the 3D network or the sol enters the gel phase (**Figure 43**).

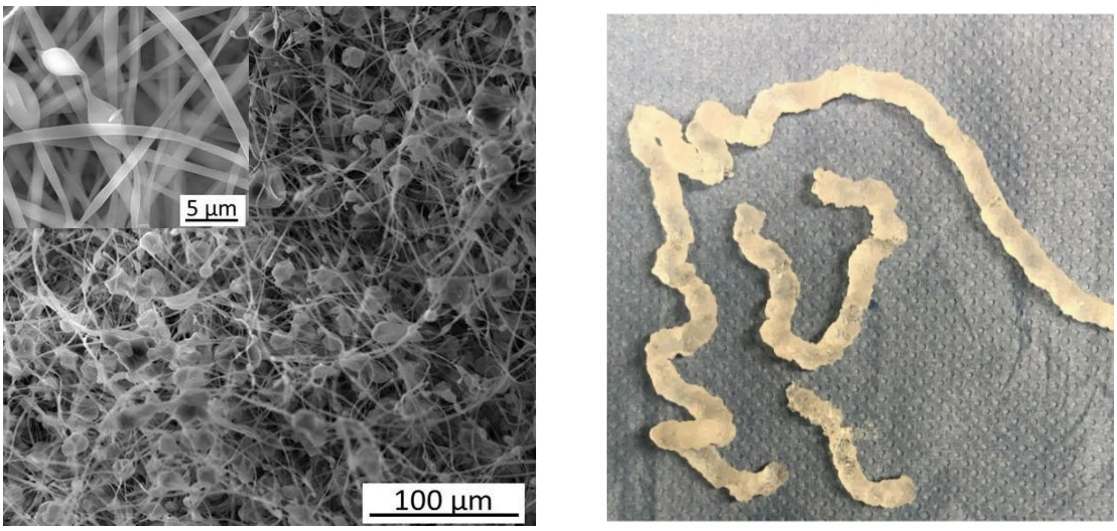

Figure 43 Representation of the result with inappropriate sol concentration before the electrospinning process a) viscosity too low; b) viscosity too high.

5.3 Electrospinning

Prepared solutions were first tested on small-scale needle-electrospinning equipment (**Figure 44**). For initial testing, only a small amount of sol was prepared, and such an amount is not sufficient for large-scale electrospinning instruments. However, the spinnability of the solution i.e., confirmation of liner, low branched macromolecules were observed. Using needle-electrospinning strong electrodynamics voltage to a polymer solution (metallic needle), where charge is induced in the polymer and charge repulsion occurs in the solution. Above a certain critical value of the applied electric field strength, which overcomes the solution capillary forces, the liquid surface self-organises on a mesoscopic scale. This instability is represented by growing stationary capillary waves with the formation of "Taylor cones" transitioning into jets of the polymer solution, which split under intense solvent evaporation. The formed nozzles move towards the electrically expressed collector, where fibres are deposited with a random orientation in the form of a planar structure. For better recognition, the formation of fibres was observed on a black paper attached to the collector. During the process, several parameters such as speed rate, voltage or distance between collector and solution were modified.

Figure 44 Observation of fibre formation on a paper attached to the collector.

Then, DC electrospinning was undertaken utilising a Nanospider™. The physical process of fibre formation is quite similar to needle electrospinning. However, using a Nanospider device, the polymeric solution is applied to the string, where thousands of Taylor cones can be formed at the same time. Upscaling to the industrial scale brought challenges to the stability of the sol. As mentioned before, the initiator of hydrolytic reactions is water, when the system is exposed to the air moisture in the spinning chamber, molecules of water can start hydrolysis again and change the viscosity parameters. At worst, polymeric reactions can occur fast and even before spinning all the solution, the network can grow that much to create an undesirable gel directly during the electrospinning process. Hence, environmental parameters during the spinning process need to be considered and monitored. Especially humidity in the chamber has to be kept as low as possible.

5.4 Characterisation

All electrospun fibrous materials prepared according to the above-mentioned sol-gel process and subsequent electrospinning techniques were analysed using various characterisation techniques with the aim of confirming the successful preparation of smooth homogenous fibres without any inhomogeneities (SEM) as well as their structure (ssNMR, Raman, FTIR). There were also several characterisation experiments determining their closer specification (TGA, contact angle, conductivity measurement, etc.).

5.4.1 Morphology characterisation

To observe the morphology of created fibrous layers, *scanning electron microscopy* (SEM) was used.

Fibres created from OBA precursors were confirmed. From **Figure 45a** can be observed morphologically compact and homogenous fibres from both electrospinning techniques. Depending on several parameters, the prepared organosilane fibres were long and continuously deposited on the collector. The fibrous diameters were evaluated statistically from several SEM images. The average size of fibres is 494.4 ± 160.1 nm. Although the fibres are relatively thin, they can be easily removed from the substrate and manipulated without cracking. A diagram of fibrous diameter distribution can be seen in **Figure 45b**.

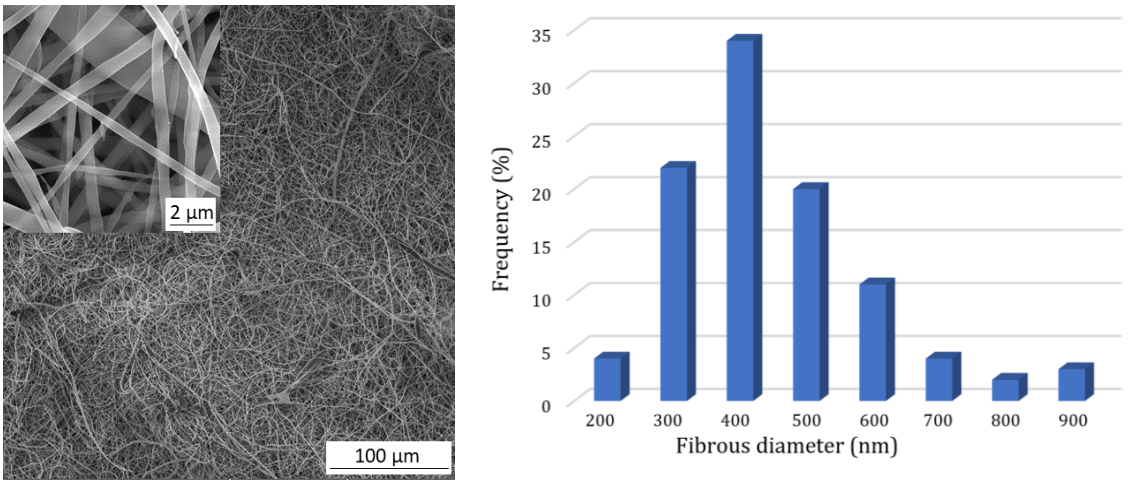

Figure 45 SEM images of the prepared OBA fibres in 100% mol. ratio (a) and diagram of a diameter distribution from 100 to 900 nm (b).

The homogenous morphology of created BiTSAB fibres was confirmed by SEM images (**Figure 46a**) from both electrospinning techniques. The distribution of fibrous diameter is wider than with OBA fibres. BiTSAB fibres were detected ranging from 100 nm to almost 2000 nm. With the highest representation around 1200 nm. The average diameter of these fibres is 1117.8 ± 348.9 nm. A diagram of fibrous diameter distribution can be seen in **Figure 46b**.

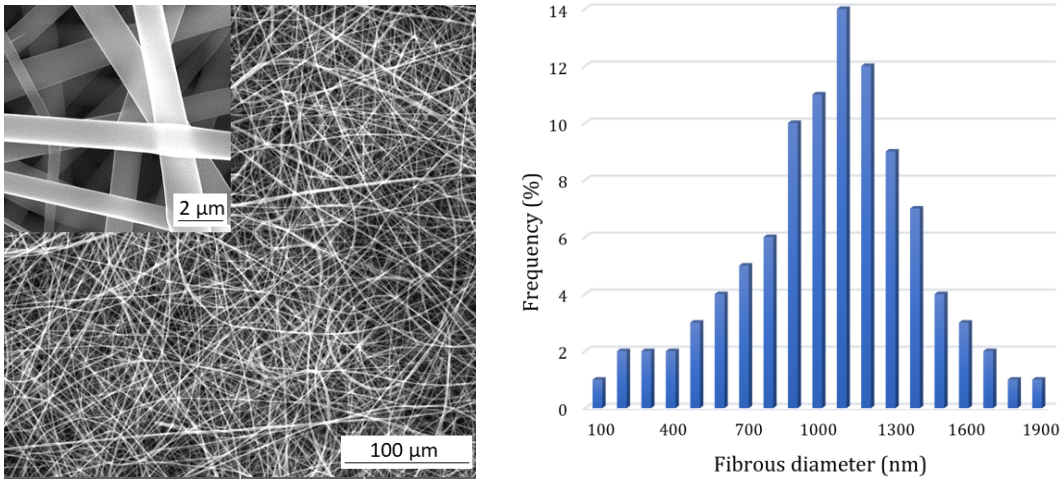

Figure 46 SEM images of the prepared BiTSAB fibres in 100% mol. ratio (a) and diagram of a diameter distribution from 100 to 1900 nm (b).

As well as with both previous layers, fibres created from BiTSAP precursors were detected deposited on the collector smooth and homogenous (**Figure 47a)**. The fibrous diameter was processed statistically from different SEM pictures and ranging from 200 to 1900 nm. The highest representation is around 900 nm with an average of 967.3 ± 322.9 nm. A diagram of fibrous diameter distribution can be seen in **Figure 47b**.

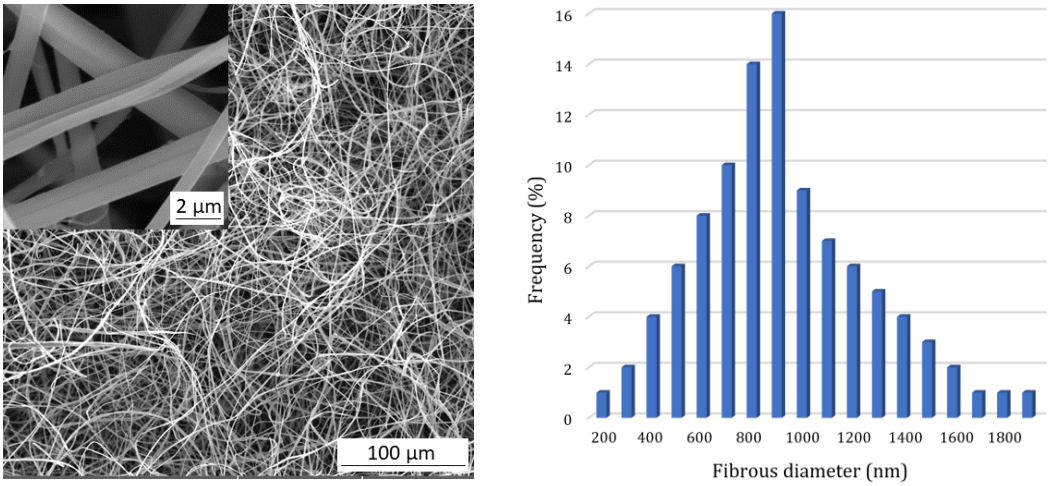

Figure 47 SEM images of the prepared BiTSAP fibres in 100% mol. ratio (a) and diagram of a diameter distribution from 200 to 1900 nm (b).

5.4.2 Structural characterisation

To characterise the structure of a newly created fibrous layer, several characterisation techniques were utilised. First of all, the solid-state nuclear magnetic resonance spectra were recorded. Regarding observing possible changes in the organic part of the molecule, the ^{13}C ssNMR was embraced as well as the ^{29}Si ssNMR for condensation of a polysiloxane network.

The ^{13}C spectra of electrospun organosilane fibrous materials (**Figure 48, S18 and S19**) indicate signals of -CH_2-Si≡ (10 ppm), -CH_2- (23 ppm), -CH_2-NH- (43 ppm), and

carbonyl (161 ppm) carbons. In addition, the signals at around 18 ppm (-CH_3 groups) and 59 ppm (-OCH_2- groups) were detected in all spectra. These signals reveal the presence of residual ethoxy groups. The relative molar content of unreacted ethoxy groups for each sample is summarised in **Table 12** as an average value of $I(\text{-CH}_3)_{exp}/I(\text{-CH}_3)_{Theor}$ and $I(\text{-OCH}_2\text{-})_{expt}/I(\text{-OCH}_2\text{-})_{Theor}$ ratios, where $I(\text{-CH}_3)_{exp}$ and $I(\text{-OCH}_2\text{-})_{expt}$ are integral intensities from experimental ^{13}C MAS NMR spectra of corresponding signals and $I(\text{-CH}_3)_{Theor}$, $I(\text{-OCH}_2\text{-})_{Theor}$ are theoretical integral intensities in a non-reacted mixture. The above-mentioned data of the investigated system confirmed the same structure of organic molecules before and after the sol-gel process.

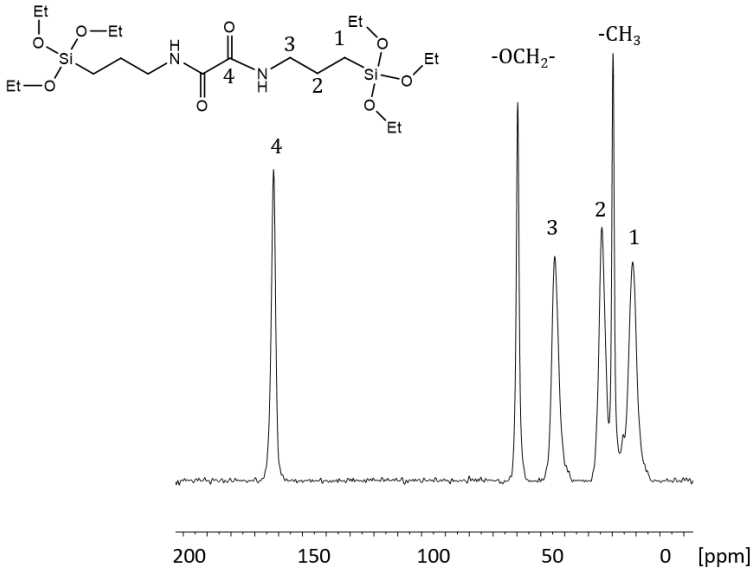

Figure 48 Spectrum of the ^{13}C liquid state NMR of the synthesised OBA fibres measured in DMSO-d_6.

The relative amount of the unreacted ethoxy group (**Table 12**) is an interesting result regarding the context of understanding the extent of chemical reaction or conversion in a system. In chemical processes involving ethoxy groups, such as hydrolysis or condensation, the presence of unreacted ethoxy groups can provide valuable insights into the completeness of the reaction. It is a valuable aspect of characterising chemical reactions, offering insights into the efficiency and completeness of the reaction process, and providing control parameters for optimising material properties in various applications. Depending on the application, the level of unreacted groups may be tailored to achieve specific material characteristics, such as porosity, surface reactivity, or mechanical strength.

Table 12 Relative amount of unreacted ethoxy groups (relative to the initial mixture) determined from ^{13}C ssNMR spectra.

Sample	x [%]
OBA	35.4
BiTSAB	3.2
BiTSAP	4.6

To determine the structure of electrospun fibres, the ^{29}Si ssNMR spectra were analysed. All types of fibres containing three signals in ^{29}Si CP/MAS NMR spectra originated from the three different polysiloxane species possible from the polycondensation reactions. Such units correspond to T^1 (-53 ppm), T^2 (-60 ppm) and T^3 (-68 ppm) structural motives. The molar content of each unit as well as the condensation degree were calculated using individual integral intensity of the signal. These results are noted in **Table 13**.

Table 13 Molar percentage of siloxane (T^n) units determined from ^{29}Si CP/MAS NMR together with calculated condensation degree q_i.

Sample	T^1	T^2	T^3	q_i
OBA	44.1	49.1	6.7	0.54
BiTSAB	9.0	76.2	14.8	0.69
BiTSAP	21.2	68.9	9.9	0.63

*Condensation degree (q_i) was calculated using the modified formula [157,158]: $q_i = \sum_{n=1}^{3} \left(\frac{nT^n}{3}\right)$ where T^n is a molar fraction of T^n units and n is the number of bridged oxygen atoms attached to the unit.

Fibres prepared from OBA are mainly linear/low-branched structures as they contain only 6.7 mol.% of branching T^3 units. The spectra from fibrous material produced by condensation of the OBA sample are characterised by the condensation degree of 0.54 and the number of unreacted ethoxy groups in the system (35.4%) also indicates the low cross-polymerisation and branching.

Quite different spectra regarding the degree of polycondensation can be observed with fibrous materials made from BiTSAB precursor. According to the ^{29}Si ssNMR, three signals can be recognized. As with the OBA spectra T^1 (-53 ppm), T^2 (-60 ppm) and T^3 (-68 ppm) structural motives can be seen. However, the relative amount of each species gives an awareness of a more condensed structure. The degree of polycondensation of BiTSAB fibres is 0.69 resp. 0.63 for BiTSAP and the relative amount of unreacted ethoxy groups is lower. From this point of view, this structure is not unduly branched (T^3 units = 14.8 resp. 9.9). In addition, the BiTSAB and BiTSAP materials contain aromatic systems and hence, the π-π stacking could be created during the sol-gel process. Non-covalent forces provide multiple advantages in the field of materials science. Such interactions have potential applications in a comprehensive range of biomedical and biotechnological fields [159]. From several studies of a benzene dimer and phenyl rings it is observed that π orbitals do not act as in conventional overlap-driven covalent bonding [160]. ^{29}Si CP/MAS NMR spectra can be seen in **Figure 49**.

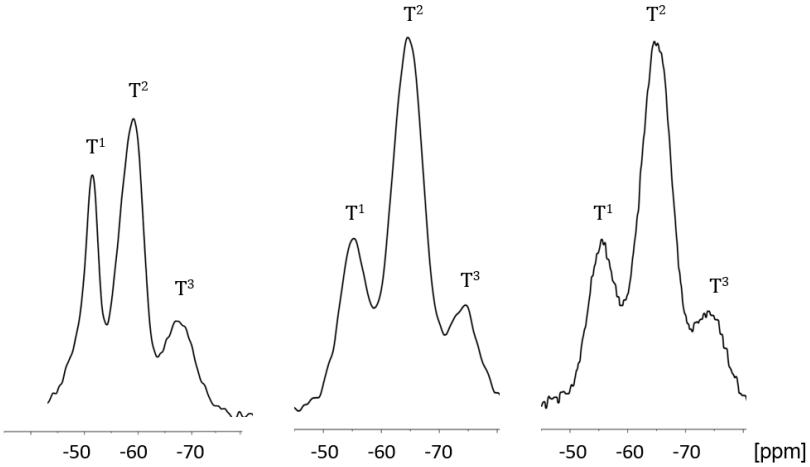

Figure 49. ^{29}Si CP/MAS ssNMR measurements of OBA, BiTSAB and BiTSAP fibres and the structure of the siloxane matrix marked as T^1, T^2 and T^3 units.

5.4.3 Fibrous features

5.4.3.1 Thermal stability

The thermal stability of prepared fibres corresponds to the thermal stability of synthesised organosilane precursors (**Figure 50**). Formed fibres show slightly higher thermal stability likely due to the induced cross-linking via the polycondensation reactions. Coupling TGA with FTIR proved only ethanol produced in the range of temperatures between 105 °C and 220 °C. Understanding the thermal stability of both the precursor and the resulting fibres is essential for determining the suitability of the fibres for specific applications. Therefore, the enhanced thermal stability of the prepared fibres is a significant advantage over currently used fibrous materials that are typically usable up to temperatures below 100 °C. It suggests that the new fibres have the potential to withstand higher temperatures which can be advantageous in various applications where exposure to elevated temperatures is a critical factor. High thermal stability may be desirable for applications where the fibres are exposed to elevated temperatures, such as in aerospace, automotive, or high-temperature industrial processes. Schemes regarding to thermal behaviour of BiTSAB and BiTSAB fibrous materials can be seen in **Figures S20** and **S21.**

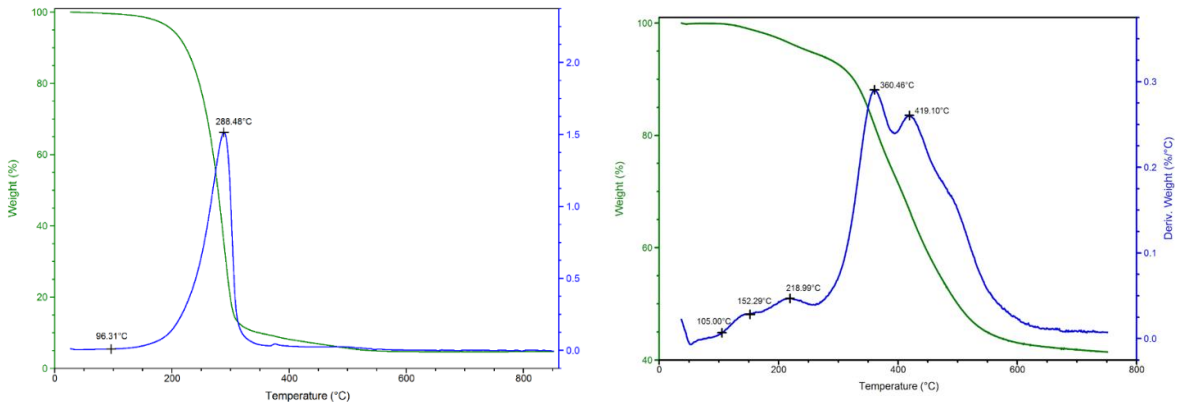

Figure 50 Scheme of thermal behaviour of organosilane precursor OBA (a) and fibres made of it (b).

5.4.3.2 Specific surface area

The Brunauer-Emmett-Teller method (BET) is commonly used to measure the specific surface area (SSA) of porous materials, including nanofibres. It is based on the adsorption of gas molecules onto the surface of the material at different pressures. From the resulting adsorption isotherm (**Figure S22-S24**), the specific surface area can be calculated. As evident from **Table 14** surface area of organosilane fibres is low compared to other published SSA values of polymer nanofibres [161]. However, it is important to note that the diameter of the fibres significantly influences the measurement. Considering the several times higher diameters of the compared organosilane materials and the necessity to correlate these values per unit weight, a low SSA value can be expected, especially considering that these are smooth, non-porous fibres. On the contrary, despite the lower SSA values, it is evident from the SEM image and subsequent cell tests that the surface of the organosilane fibres is suitable for cell colonies. This suggests that factors beyond SSA, such as surface chemistry and biocompatibility, play significant roles in determining cell response and adhesion. This highlights the importance of considering various aspects beyond SSA when assessing the suitability of nanofibres for specific applications, particularly in biological contexts.

Table 14 BET calculated the surface area of created organosilane fibres.

	Surface area [m^2/g]	C constant	Correlation coefficient
OBA	2.00	17.27	0.999
BiTSAB	4.32	27.88	0.999
BiTSAP	3.25	28.29	0.999

5.4.3.3 Conductivity

Conductivity in regenerative medicine plays a significant role in the development of a new biomaterial. The formation of a suitable and functional biomaterial for neuroregenerative purposes is a vital factor that should be closely interconnected by a combination of electrical conductivity and structural variability of the proposed material. Thus, the material can provide desirable physical conduits and support electrical signal transport together with communication between neurons [162].

The electrical conductivity of created fibres was observed. In previous research (with commercially available precursors), the potential conductivity was measured using impedance spectroscopy. The measurements were carried out in potentiation mode (voltage amplitude 0.2V) over the frequency from 0.1Hz to 1MHz at different temperatures and three relative humidities (44 %, 75 % and 100 %). It was observed that the conductivity exceeds the semiconductor limit (10^{-10} S/cm) in the case of fibres made of 50 mol.% BTESB and 25 mol.% BTESBP (**Figure 51**).

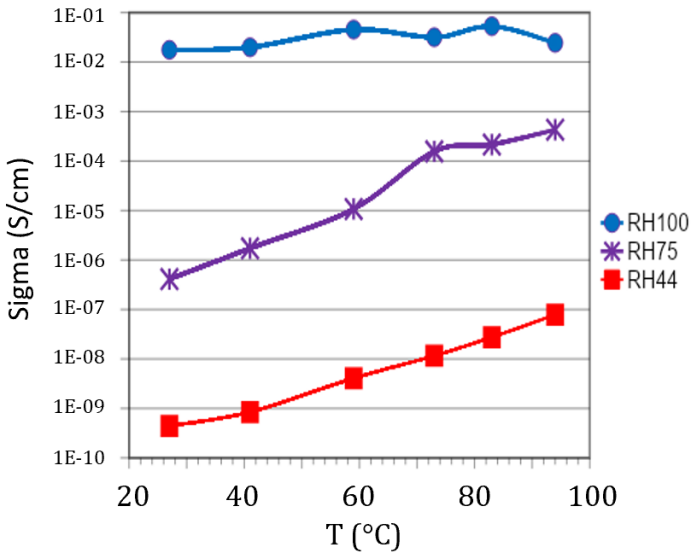

Figure 51 Spectra of electrical conductivity of fibrous layer made of BTESBP in dependence of different temperatures and humidity (RH = 29, 75 and 100 %).

An assumption has been made, when the precursors contain aromatic functional groups or conjugated multiple bonds, the new localised levels are formed in the forbidden band of the electronic structure, reducing the energy gap of the electron moving from the valence to the conduction band. However, measuring the conductivity of fibrous layers poses several notable challenges. The primary challenge lies in achieving accurate measurements at the nanoscale, where the dimensions of the fibres are often on the order of several hundred nanometres. Traditional macro-scale measurement techniques may lack the sensitivity required to capture the intricacies of conductivity in these fine structures. Ensuring consistent and reproducible contact between the measuring apparatus and the nanofibres presents another challenge, as the small size and flexibility of the fibres can make it difficult to establish reliable electrical connections. Moreover, the presence of insulating or dielectric components within the fibres can impact conductivity measurements, necessitating careful consideration of the overall material composition. Measuring conductivity in the presence of humidity also introduces additional complexities to the assessment of fibrous materials. Humidity can significantly impact the electrical properties of materials, influencing both the conductivity and the overall performance of conductive fibres. One major challenge lies in the need to account for the variable moisture content within the fibres, as water molecules can act as charge carriers and alter the electrical behaviour of the material. Additionally, humidity-induced changes in the physical structure of the fibres, such as swelling or alterations in surface morphology, can further affect conductivity measurements. Ensuring accurate and reproducible measurements under varying humidity conditions requires sophisticated instrumentation capable of maintaining controlled environmental conditions. Moreover, the potential for moisture absorption by

the fibres themselves necessitates careful consideration of the material's hygroscopic nature. Addressing these challenges is crucial for obtaining a comprehensive understanding of how fibrous materials behave in real-world conditions, especially when considering applications in electronics, sensors, or regenerative medicine, where environmental factors such as humidity play a critical role in material performance.

Although the required limit for the semi-conductive properties of the material was exceeded (**Figure 52**), due to the objections mentioned above, it is not possible to evaluate the conductive properties of these materials. Further research is going to be conducted in this area, with a series of samples having different parameters.

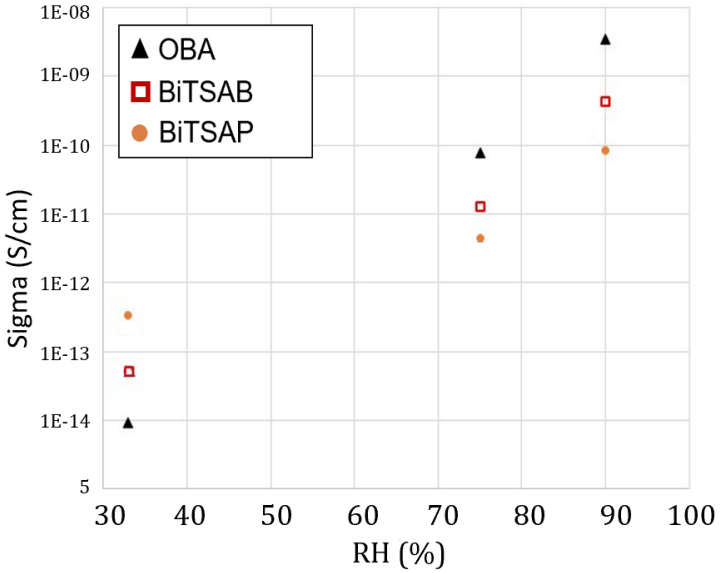

Figure 52 Dependence of the specific electrical conductivity on the temperature and relative humidity of the environment of synthesised organosilane fibres in 100 mol.% ratio.

5.4.3.4 Contact angle

Contact angle refers to the angle at which a liquid/vapour interface is in contact with a material's surface. It is a measure of the wettability of a solid surface by a liquid which quantifies the degree to which a liquid spread on a solid. Contact angle is determined by the balance of adhesive forces and cohesive forces which is usually measured by a contact angle goniometer. Hydrophobic behaviour is defined with a low wettability with angles from 0° to 90°. On the other hand, when angles from 90° to 180° are observed, tested material is defined as hydrophilic which indicates the high wettability. In the field of material science, contact angle plays an important role in the characterisation of the surface properties of a material. The hydrophobic or hydrophilic nature of a surface can affect further process parameters such as adhesion, friction or subsequent functionalization.

In biomedical applications, the contact angle is one of the crucial parameters. The interaction of cells with the surface of a biomaterial is one of the key importance for the successful long-term implantation of medical devices [62]. Cell adhesion is a fundamental

process directly involved in cell growth. Parameters such as surface energy, roughness and chemical composition of the surface of the tested material significantly influence cell interactions [77]. Therefore, the measurement and control of contact angles are essential in the designing of new materials and devices for regenerative medicine.

The hydrophobicity was tested in all prepared fibres (**Figure 53**). With fibres created from organosilane precursors OBA and BiTSAB, the hydrophobic character was observed. The average angle of a water droplet on the surface was 119° ± 7 for OBA and 108° ± 5° for BiTSAB. The hydrophobic nature can hinder the colonisation of the scaffold with cells which can negatively affect tissue regeneration. Although the hydrophobic character of biomaterial can have, in some cases, positive effects, neural tissue regeneration is not suitable and further development and optimization such as surface coating could be an alternative.

Opposite behaviour was observed within the BiTSAP fibres. The determination of the contact angle proved challenging as the droplet rapidly absorbed into the fibres within a few seconds. This phenomenon suggests a high degree of hydrophilicity, where the fibrous material exhibits a strong affinity for and rapid absorption of the liquid, preventing the formation of a distinct droplet shape. The inability to measure a discernible contact angle indicates a significant wetting behaviour, highlighting the hydrophilic nature of the fibres and their rapid interaction with the liquid phase. Such behaviour is advantageous within regenerative medicine because of the easy adhesion of cells. It is also very beneficial for their survival and further proliferation. Moreover, the hydrophilic nature of a material can enhance the interaction with a biological system by easier transport of nutrients and interaction with proteins and other biological molecules. On the other hand, the high water content in a material also poses several challenges. The presence of water in the material can lead to rapid degradation and loss of mechanical properties.

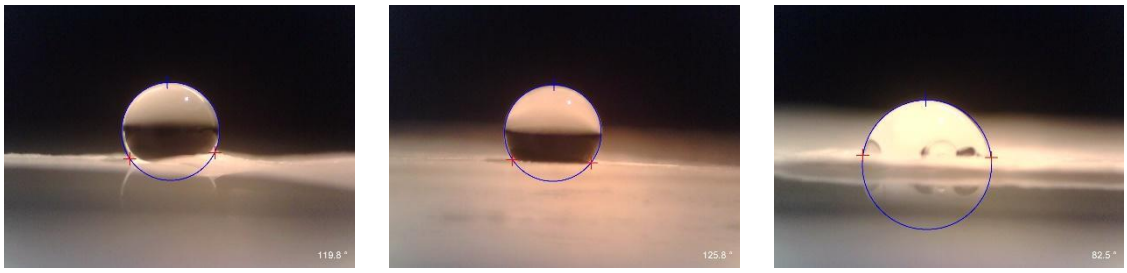

Figure 53 Contact angle of the created fibrous materials OBA (a), BiTSAB (b) and BiTSAP (c).

5.5 Biological assessment

5.5.1 Simulated Body Fluid

Simulated Body Fluid (SBF) is a solution designed for mimicking the ionic concentration of a human blood plasma. This solution is commonly used in the field of

biomaterials and regenerative medicine to assess the bioactivity of a material. Bioactivity indicates the ability of a material to trigger cellular and tissue responses when implanted in a human body. The indicator of bioactivity when immersed in SBF is the ability of a material to create a layer of HAp on its surface. Hydroxyapatite, a calcium phosphate compound, is a key component of natural bone and is often used in biomaterials due to its biocompatibility. The identification of HAp on the fibres suggests a potential bioactive response to the simulated physiological environment, where interactions with components in the solution led to the formation of this biologically relevant mineral. Such layers can then promote the integration of the implanted material with surrounding tissue.

All fibres were tested in the solution of SBF. After immersion for 30 days, the presence of a HAp layer was observed. Firstly, using SEM to detect any sights of a newly formed layer. To further characterise the nature of this newly identified layer, X-ray Diffraction (XRD) was employed. XRD analysis provides information about the presence of crystalline structure and composition of the detected crystalline layers.

When examining the OBA fibres immersed in SBF the presence of a new layer on the fibre surface was revealed (**Figure 54a**). The nature and composition of this newly formed layer could be indicative of interactions between the OBA fibres and the components present in the SBF. By subjecting the OBA fibres with the new layer to XRD, the diffraction patterns were examined to understand the crystallographic nature of the deposited material (**Figure 54b**). This additional analysis contributed to a more comprehensive understanding of the changes occurring on the surface of the OBA fibres during immersion in SBF. The results of the XRD characterisation confirmed the presence of HAp within the observed new layer on the fibres. Such findings are significant in the context of biomedical applications, as the presence of HAp on the fibres suggests the potential for enhanced bioactivity and compatibility with biological systems.

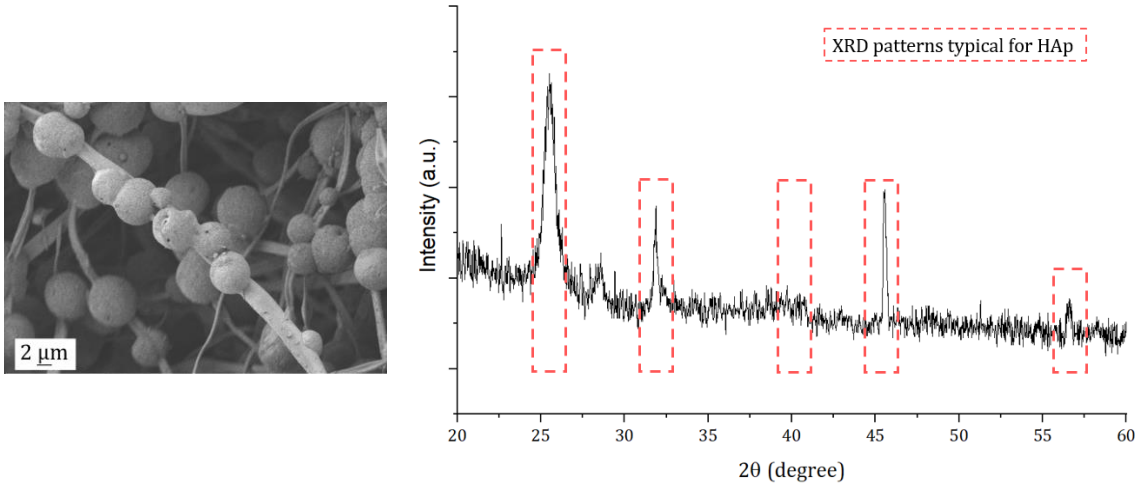

Figure 54 SEM images of the prepared OBA fibres after immersion in SBF for 30 days (a), XRD analysis of newly formed layer on OBA fibres (b).

When subjecting BiTSAB and BiTSAP fibres to the SBF environment, no signs of newly created layers were observed. The absence of a discernible new layer suggests that the fibres may not have undergone significant changes or reactions during exposure to the SBF environment. This observation confirmed through testing and analysis, is valuable information for understanding the material's behaviour in a simulated physiological environment. The lack of a new layer may imply that these fibres have a stable and less reactive response to the SBF conditions. It is essential to consider these results in the context of the intended applications of BiTSAB and BiTSAP fibres, as their stability in physiological environments may be advantageous for certain biomedical or regenerative medicine applications.

5.5.2 Protein adhesion

Process adhesion describes the first contact of material within the body fluids in a process where proteins bind or adhere to the surface. In the context of a biomedical application, the protein adhesion process is very important and the result is essential to presume the behaviour of a newly designed material in a human body. Depending on the application, promoting protein adhesion combined with surface adjustment can be desirable. Especially in the case of medical implants such as artificial joints or heart valves, excessive protein adhesion can lead to problems like biofouling or the formation of blood clots. On the other hand, in applications such as tissue engineering or wound healing, the promotion of protein adhesion can be beneficial. Certain proteins can prompt cell adhesion and proliferation, which can support tissue regeneration. Understanding and controlling the protein adhesion is also a crucial parameter in the drug delivery area. Protein-surface interactions can impact the delivery as well as the release of a drug. Therefore, protein adhesion testing plays a major role in the development of biomaterials and biomedical devices.

Adsorption of BSA was analysed based on strengths of interaction with the fibrous materials whereby the amount of protein released with PBS (Wash 1 and Wash 2) or with SDS (desorption) indicated the relative amounts of soft-bound or hard-bound proteins respectively. OBA nanofibres contained the highest concentration of BSA in the PBS from Wash 1 compared with fibres from TEOS and PCL (**Figure 55a**), attributed to OBA fibres having a relatively high degree of soft-bound protein adsorbed with a significant difference from PCL (**Figure 55b, Wash 1**). Furthermore, as there is a downward trend in the concentration of adsorbed protein with Wash 2 and subsequently with SDS desorption, the predominant interaction on OBA material can be described as the weaker soft-bound proteins. In contrast, TEOS displayed a lower quantity of BSA after Wash 1 compared to

OBA, however, it contained a significantly higher concentration of hard-bound protein after desorption. PCL on the contrary, was able to bind significantly lower amounts of soft-bound proteins compared to OBA, but near equal quantities of hard-bound proteins (with desorption compared to washes).

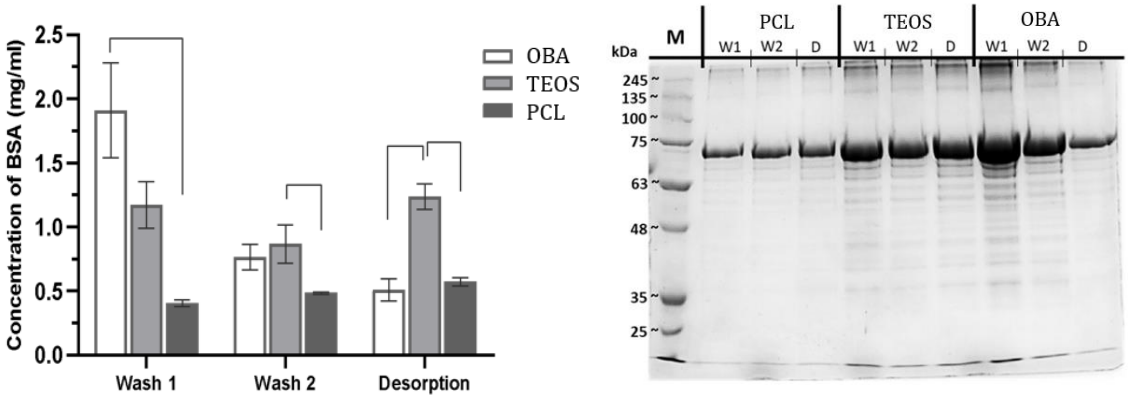

Figure 55 BSA concentration in tested solutions from PBS (Wash 1 and Wash 2) and 1% SDS (Desorption) after protein adsorption with various fibrous materials. *Denotes significant difference between samples within groups at the time point ($p < 0.05$).

5.5.3 Cell viability, morphology and distribution of 3T3 fibroblasts

Cell viability is a fast method which indicates the nature of the biomaterial in contact with human tissue. This is the basic method of *in vitro* testing using cell lines which helps to understand the impact of a material on the cell's health and function. It can also give an insight into the behaviour of cells and growth under certain conditions. Cell viability refers to the number of healthy and living cells after contact with a tested material. There are various methods to observe cell viability, including examining the cells under a microscope or testing a certain function by staining the cells. Such a method is usually used for the evaluation of the cytotoxicity or effectiveness of a drug treatment. Cell morphology is usually used to determine the physiological characteristics of a cell after contact with tested material. It includes the evaluation of size, shape and structure.

The morphology of cells is an important overview of the behaviour of cells as differences in cell morphology can indicate different cell types and stages of growth. Distribution of cells refers to how cells are arranged or dispersed on the sample. It can describe the spatial arrangement of the cells in a tissue, the proportion of different cell types or how the cells spread out on the surface. Both cell morphology and distribution can provide important information about cell health, function and behaviour of a tested biomaterial. Therefore, monitoring such parameters is a crucial part of *in vitro* biology testing which can provide important information about cellular responses to the different conditions or treatments.

All fibres were tested for their cytotoxic effects in comparison to already well-known PCL biodegradable polyester currently employed in many biomedical applications [163–

165] and TEOS fibres which are often employed for forming robust networks with the silica-based networks possessing tunable properties that have provided a basis for many applications, including biomedical and bioactive substrates [166,167]. OBA fibres display a high cell viability, being comparable to PCL and outperforming TEOS **(Figure 56a)**. Both OBA and PCL materials displayed cell viability nearing 100 % survival over 72 h, indicating negligible cytotoxic effects from the materials. The cytotoxic results for OBA indicate that this material could be a promising alternative to PCL.

Staining of the cells on the OBA was undertaken, with all visible cells displaying the expected morphology and distribution associated with viable cells along with good cell proliferation and distribution on the material **(Figure 56b)**.

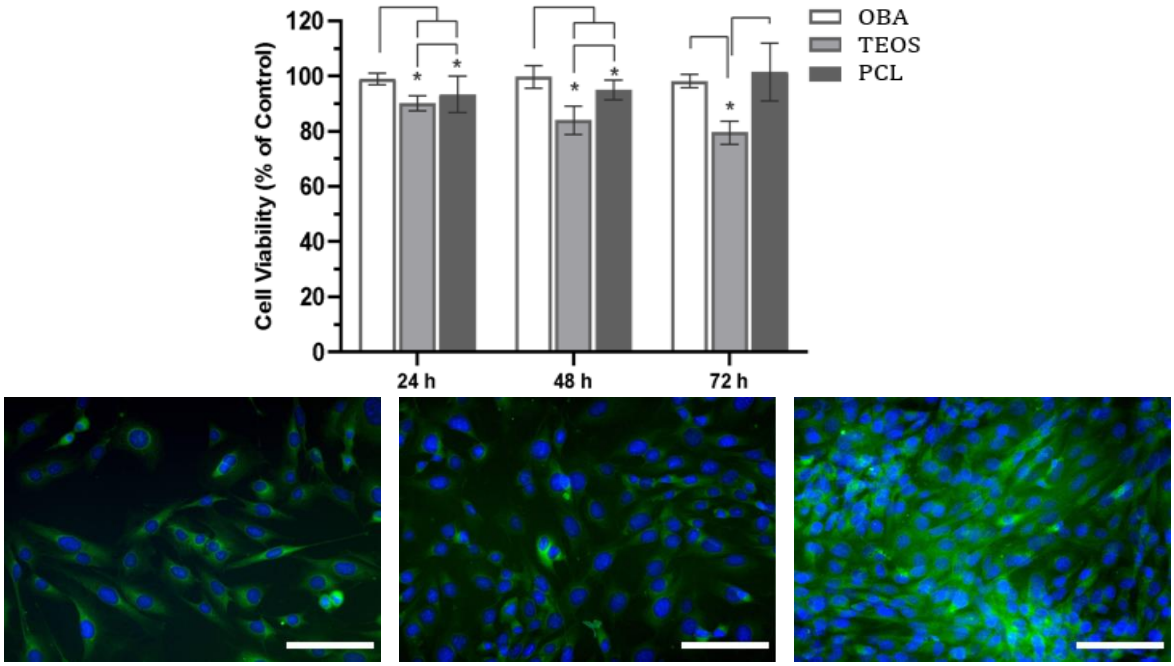

Figure 56 Cell viability (a) of prepared OBA fibres and morphology of cells (b) observed by using 3T3-A31 cell line compared to already well-studied PCL and TEOS fibres. Scale bars are 100 µm.

The initial biocompatibility screening on 3T3 fibroblasts comprised of cell viability evaluation after 24, 48 and 72 hours of exposure combined with a cell membrane disruption test (LDH leak). As evident from **Figure 57a**, the tested samples exhibited significantly higher cell viability in comparison to the positive control (PC) in all time points. Both samples, BiTSAP and BiTSAB showed an increase in cell viability within 72 hours of exposure. The BiTSAP sample can be considered biocompatible for the testing period as it has exceeded the 70 % viability threshold by exhibiting 74.81 ± 4.79 % viability after 24 hours and 84.13 ± 4.50 % after 72 hours.

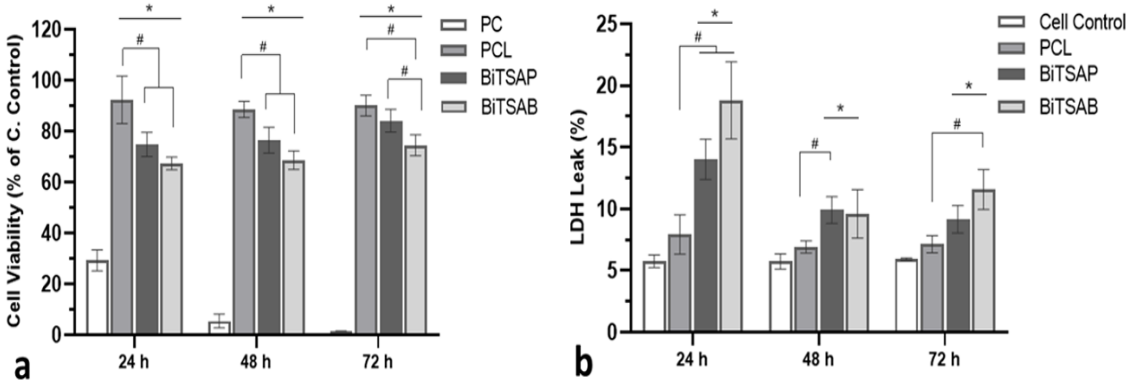

Figure 57 Impact of fibres (PCL, BiTSAP, BiTSAB) on 3T3 fibroblasts (a) cell viability and (b) membrane disruption (LDH leak). Exposure in direct contact for 24, 48 and 72 hours. Mean ± SD, ANOVA (*) with statistically significant difference to positive control/cell control ($p \leq 0.05$) and (#) between tested fibres ($p \leq 0.01$) within the time point.

The BiTSAP viability showed no significant difference to PCL control after 72 hours. The BiTSAB sample exhibited 67.32 ± 2.49 % viability after 24 hours and 74.52 ± 4.16 % after 72 hours. These results can be correlated to the LDH leak results shown in **Figure 57b**. Both the tested samples caused significantly increased LDH leak in the first 24 hours (14.02 ± 1.6 % BiTSAP, 18.81 ± 3.12 % BiTSAB) compared to cell control (CC, 5.75 ± 0.51 %) and PCL control (7.92 ± 1.61 %). As evident, the initial cell membrane disruption was stabilised after longer exposure periods and decreased to 9.17 ± 1.12 % in the case of BiTSAP after 72 hours, and eventually 11.58 ± 1.63 % for BiTSAB. The membrane disruption caused by BiTSAP nanofibres after 72 hours showed no significant difference to PCL nanofibres control at the same time point. None of the values obtained exceeded 20 % of the LDH leak level. The fluorescent microscopy analysis, see **Figure 58**, correlated with the previous quantitative results. Exposure to the BiTSAP nanofibres for 72 hours led to higher cell numbers compared to BiTSAB fibres. The 3T3 cells exhibited a normal spindle-like morphology typical for fibroblastic cells. The appearance was not disrupted after 72 hours of exposure to any tested sample. The obtained results can be related to the surface chemistry and reactivity of the organosilane nanofibres close to the silica surface chemistry. The LDH release is associated with the membrane integrity of cells, and the membrane lytic potential of certain silane materials was described previously and is often attributed to the surface silanol groups [168,169]. Although the organosilane nanomaterial´s surface chemistry is close to the one of silica, the biocompatibility of organosilane nanomaterials is improved compared for example to amorphous silica nanoparticles [170]. For example, Shinto et al. documented up to 90 % LDH release caused by 2 hours of exposure of Jurkat cells to silica nanoparticles. This toxic effect was strongly size and concentration-dependent [86].

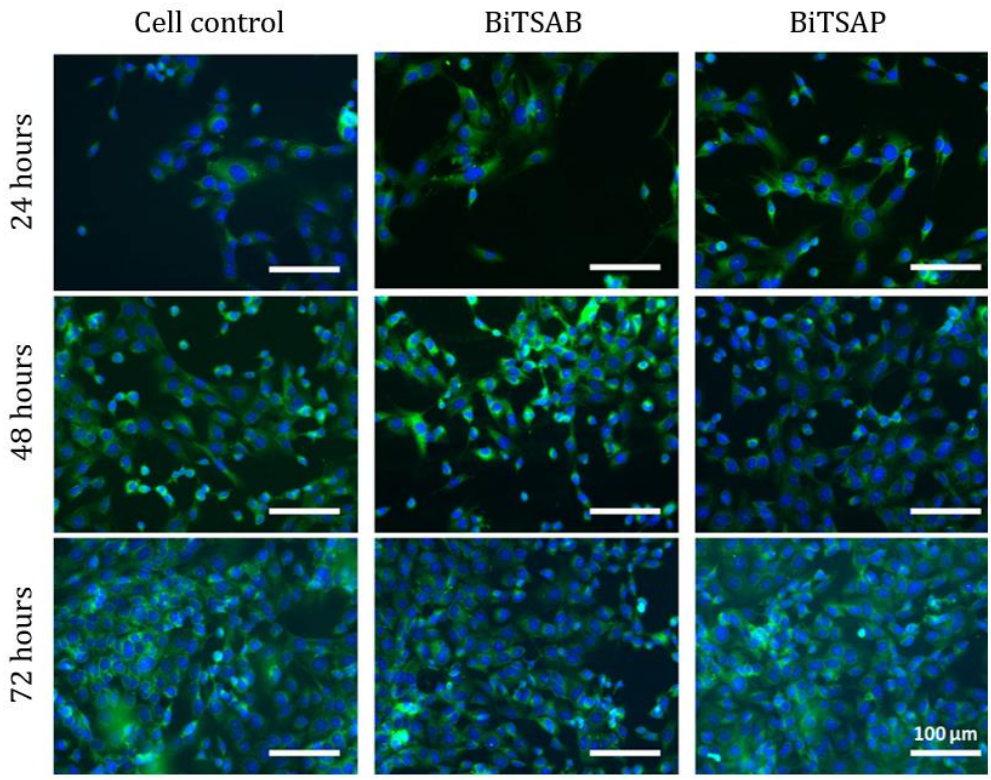

Figure 58 Fluorescent staining of 3T3 cells morphology development in up to 72 hours exposure. Comparison of untreated cell control BiTSAB and BiTSAP nanofibres. Visualized by intracellular membrane staining by DiOC6(3) (green) with nuclei counterstained by DAPI (blue). Acquired by Microscope Leica DMi8. Scale bars 100 µm.

5.5.4 *In vitro* evaluation using ADSC and HUVEC

In this study, the characterisation of fibrous materials was undertaken through the interaction with stem cells (Adipose-Derived Stem Cells - ADSC) and Human Umbilical Vein Endothelial Cells (HUVEC), crucial steps in assessing their biocompatibility and regenerative potential for applications in tissue engineering. The evaluation encompassed various aspects, including cell adhesion and morphology, viability, proliferation rates, and differentiation potential in the case of stem cells. Immunofluorescence staining and gene expression analysis were employed to visualise cellular markers and understand the molecular responses of the cells to the fibrous material. Cytotoxicity assays were performed to ensure the safety of the fibrous material, and the overall cell-material interactions, encompassing attachment, spreading, and migration, were thoroughly investigated. The study also explored the release of signalling molecules and the material's biocompatibility, contributing comprehensive insights into its suitability for diverse biomedical applications. This thorough characterisation employing both stem cells and HUVEC is pivotal in advancing our understanding of the fibrous material's cellular interactions, guiding its potential use in regenerative medicine and biomaterial development.

Within this investigation, comprehensive testing was conducted on all three fibrous materials (OBA, BiTSAB and BiTSAP). However, it was discerned that OBA fibres were not conducive to the specific testing procedures employed in this study. Consequently, the

presented results and analyses are focused on BiTSAB and BiTSAP fibres. The decision to exclude OBA fibres from the testing analysis underscores the importance of tailoring testing methodologies to the unique characteristics of each fibrous material (Figures regarding testing OBA can be found in Supplementary materials – **Figures S25-S30**). The subsequent findings about BiTSAB and BiTSAP fibres provide targeted insights into their suitability for the specific testing parameters employed, offering valuable contributions to the understanding of these materials for potential applications in regenerative medicine and biomaterial development.

On day 3 post-seeding, the cell population density (**Figure 59**), calculated as the number of cells per cm^2 of the tested materials, served as a crucial metric for assessing material toxicity and cell spreading characteristics. The results revealed a notable disparity not only between the tested materials but also among the different cell types. Particularly, the cell population density on BiTSAP was nearly twice as high as that on BiTSAB. In alignment with the initial seeding density of 25,000 cells/cm^2, adipose-derived stem cells (ADSC) on BiTSAP exhibited a relatively stable population on day 3. In contrast, on BiTSAB, a significant reduction in cell population was evident. This disparity in cell behaviour between the two materials underscores the potential influence of material composition on cell viability and spreading. The accompanying images in **Figure 60** depicting cell population density, were derived from a meticulous analysis of 26 to 36 microphotographs for each experimental point, and the calculated cell numbers are presented as mean ± SD. These findings offer valuable insights into the material-cell interactions and contribute to understanding the dynamic response of ADSCs to BiTSAP and BiTSAB, crucial for the material´s suitability in regenerative medicine.

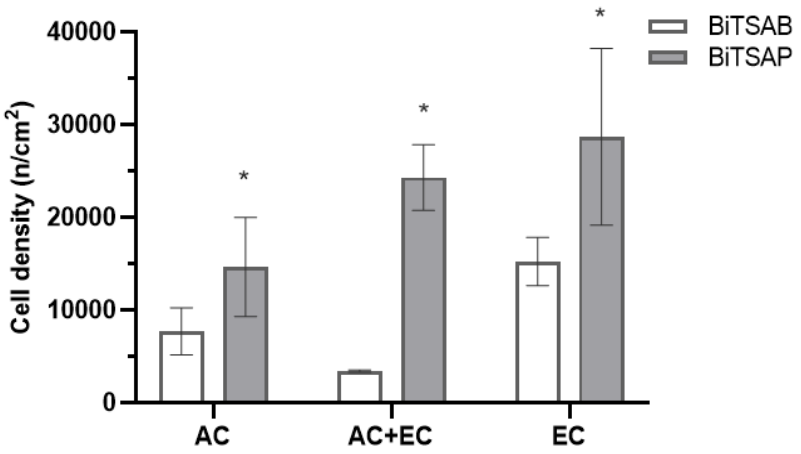

Figure 59 The cell population density of ADSC, HUVEC and their cocultivation on materials: BiTSAB and BiTSAP on day 3 after seeding. Each experimental point is calculated as mean ± S.D. from 4 independent samples (26 to 36 microphotographs). ANOVA, Student–Newman–Keuls method. Statistical significance ($p \leq 0.05$) in comparison with another group of samples is marked above the columns (*).

The visualisation of ADSC population density on the materials is presented in **Figure 60**. The figure captures the morphology and distribution of cells on the material surface. Notably, counting cells proved challenging due to the layered arrangement, and the figure's clarity may be compromised. The cells are observed to form distinct layers, making precise enumeration difficult. The figure's resolution may be compromised, impacting the sharpness of the cell boundaries and hindering a detailed quantification of the cell population. Despite these challenges, the qualitative assessment of cell morphology and distribution remains valuable for understanding the interactions between ADSCs and the materials, offering insights into their behaviour and potential applications in regenerative medicine.

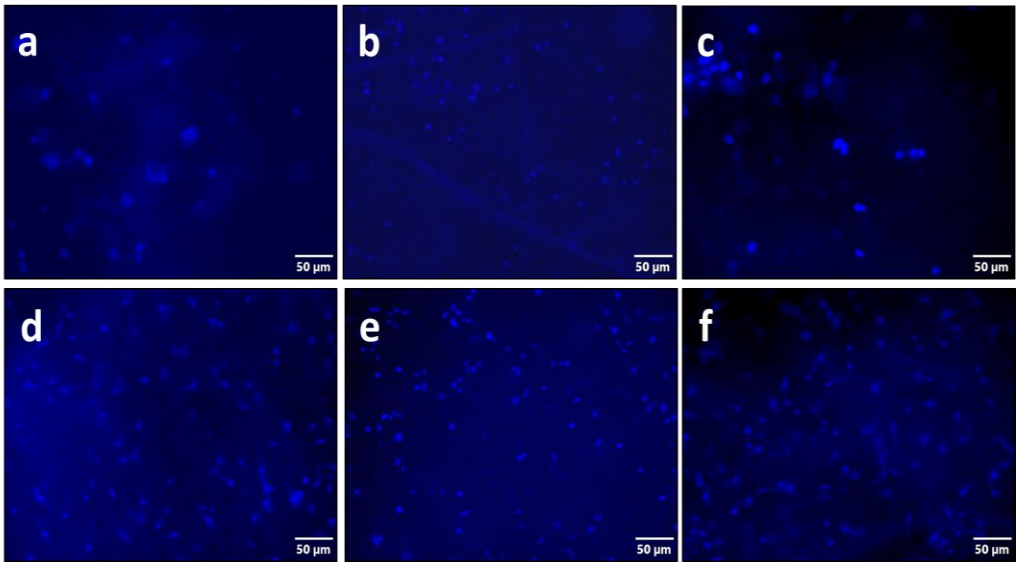

Figure 60 Visualisation of the cell population density of ADSC (a, d) and HUVEC (b, e) and their coculture (c, f) on materials: BTT (a, b, c) and BTP (d, e, f) on day 3 after seeding. Cell nuclei stained by DAPI (blue). Fluorescent images were acquired by Microscope Olympus IX71 (digital camera DP71, obj. 20x). Scale bars 50 µm.

Fibrous samples, cultivated for 3 days and subjected to the application of ADSC and iMR-90 neural stem cells, were meticulously assessed through specific staining techniques. ADSC were visualised using phalloidin staining for F-actin, while iMR-90 neural stem cells were identified through specific markers nestin and GFAP. Additionally, cell nuclei were counterstained with DAPI. The biocompatibility assessment revealed a marked difference between BiTSAP and BiTSAB. Specifically, the ADSC exhibited significantly higher biocompatibility with BiTSAP, as evidenced by a denser cell population with polygonal and elongated shapes (**Figure 61b**). In contrast, ADSC on BiTSAB displayed a less favourable response, presenting round and poorly adhered characteristics with lower cell density (**Figure 61a**). Moreover, iMR-90 neural stem cells colonised BiTSAB in small groups (**Figure 62a)**, while on BiTSAP, the fibres were uniformly covered coherently (**Figure 62b)**. These observations underscore the distinct biocompatibility profiles of BiTSAP and BiTSAB,

highlighting the potential of BiTSAP for enhanced cell colonisation and interaction, which is pivotal for its consideration in regenerative medicine applications.

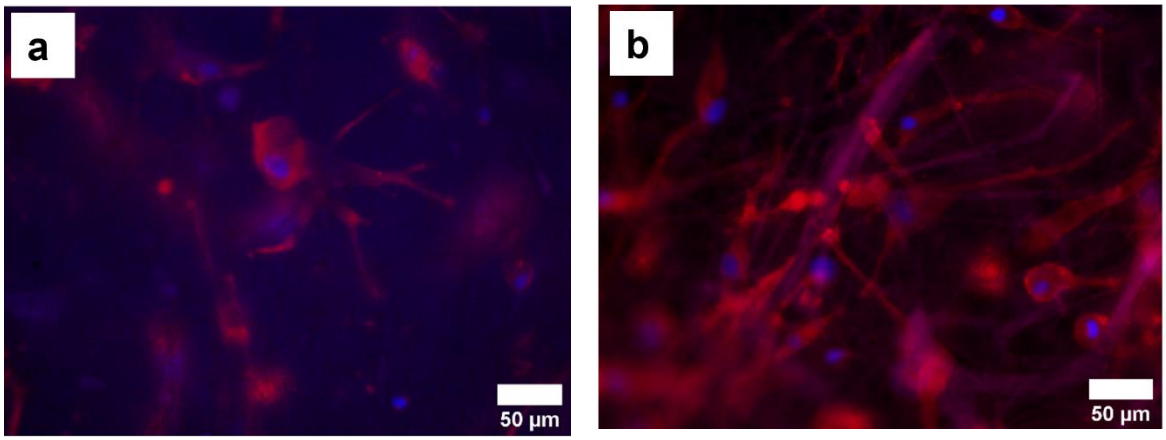

Figure 61 Morphology of ADSC seeded on materials: BiTSAB (a) and BiTSAP (b) visualised by F-actin staining (red) and Cell nuclei counterstained by DAPI (blue). Fluorescent images were acquired by Microscope Olympus IX71 (digital camera DP71, obj. 20x).

The application of cells on organosilane fibres resulted in the formation of cohesive cell groups with notable proliferative capabilities (**Figure 63a**). Remarkably, BiTSAP fibres demonstrated superior outcomes, particularly in terms of the attachment of neural stem cells to the surface. In **Figure 63b**, a striking depiction is observed, wherein cells are evenly distributed across the surface of the BiTSAP sample. Furthermore, the cells exhibited the ability to extend processes, adopting a neural-like morphology. These findings underscore the favourable interaction between neural stem cells and BiTSAP fibres, showcasing not only successful cell attachment but also the propensity for cells to adopt a neural-like phenotype. Such characteristics are pivotal in the context of regenerative medicine, suggesting the potential suitability of BiTSAP for neural tissue engineering applications.

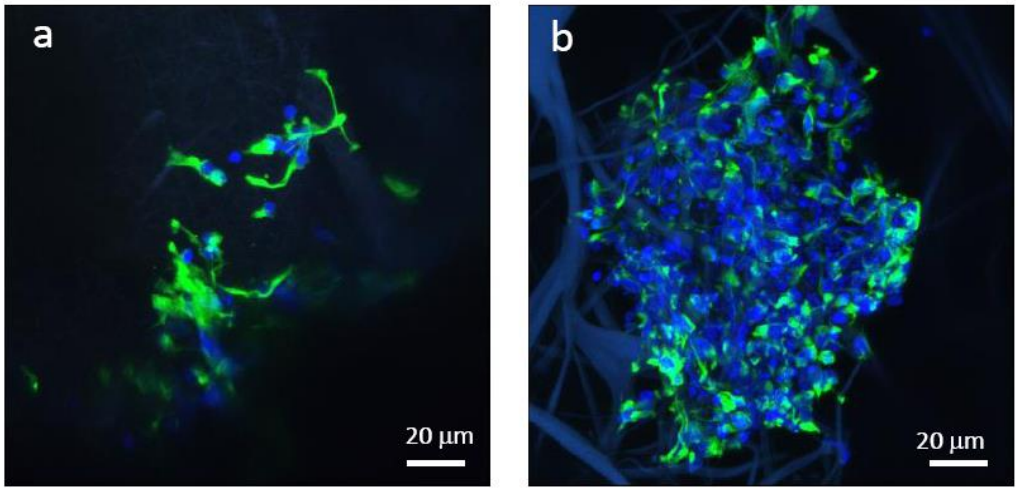

Figure 62 Morphology of iMR-90 seeded on materials: BiTSAB (a) and BiTSAP (b) visualised by specific marker nestin (green). Cell nuclei counterstained by DAPI (blue). Fluorescent images were acquired by LSM 810 DUO laser scanning confocal microscope (Zeiss).

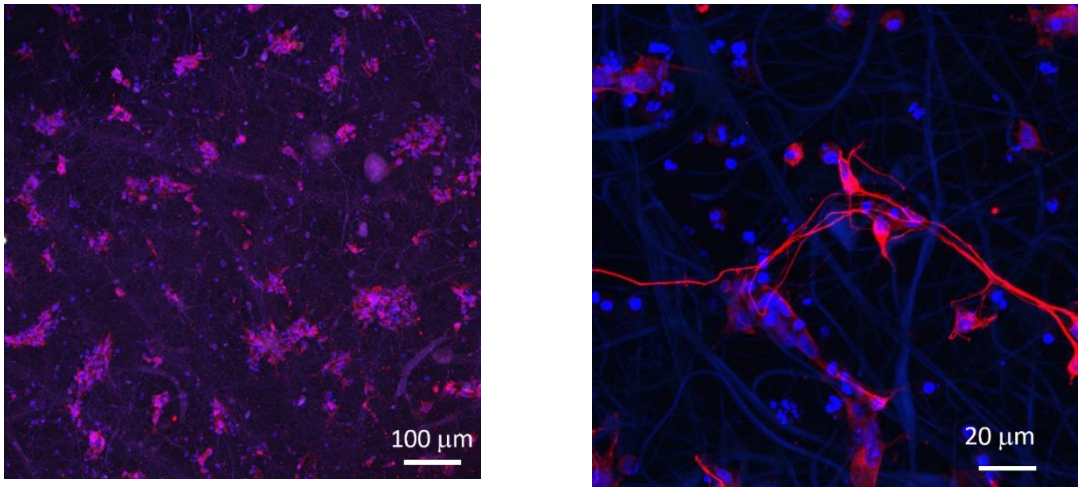

Figure 63 Morphology of iMR-90 seeded on BiTSAP material visualised by specific marker GFAP (red). Cell nuclei counterstained by DAPI (blue). Fluorescent images were acquired by LSM 810 DUO laser scanning confocal microscope (Zeiss).

The metabolic activity of both ADSC and HUVEC in the two sample groups was assessed at 24 hours, 48 hours, and 72 hours to monitor cell growth and survival over this period (**Figure 64**). On BiTSAP fibres, the metabolic activity of both ADSC and HUVEC exhibited a continuous increase, peaking on day 3 after achieving partial confluence. In contrast, the metabolic activity on BiTSAB remained mostly stabilised at lower values throughout the same time frame, with only endothelial cells showing increased viability after 72 hours of cultivation. Cocultivation of ADSC with endothelial cells proved successful, indicating potential applications in soft tissue engineering. In prostheses for soft tissues, the juxtaposition of smooth muscle cells with endothelial cells or the vascularisation of soft tissues by the endothelial cell system is crucial. The scaffold's influence extends beyond individual cell types, influencing their coexistence and interactions. Notably, the metabolic test results align closely with the cell number estimates obtained through cell counting on these samples, reinforcing the consistency of findings across different evaluation methods. These insights contribute valuable information for the potential utilisation of BiTSAP and BiTSAB in regenerative medicine, specifically in the context of soft tissue engineering.

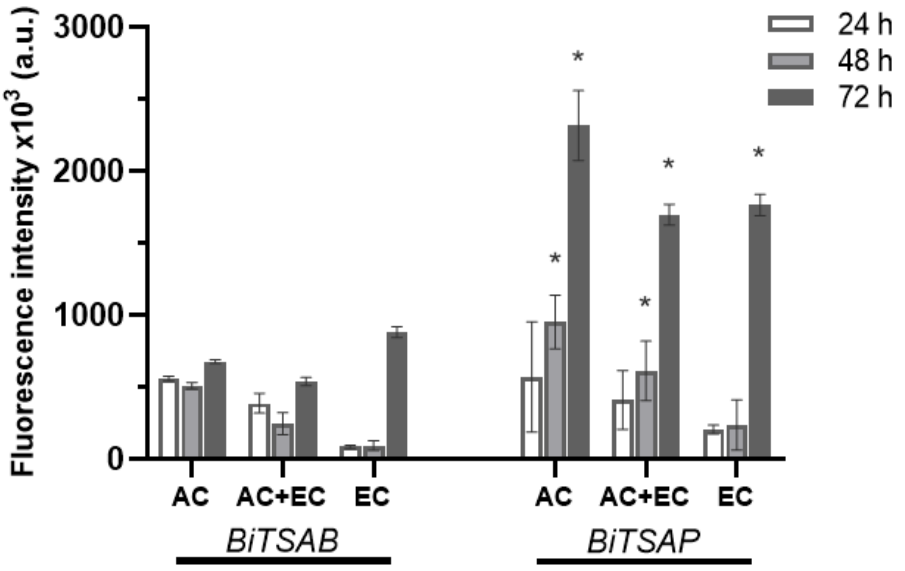

Figure 64 Metabolic activity of ADSC (AC) and HUVEC endothelial cells (EC), measured by resazurin assay in 72 hours after seeding on materials: BiTSAB, and BiTSAP. Mean ± SD from 4 independent samples. ANOVA, Student–Newman–Keuls method. Statistical significance ($p \leq 0.05$) in comparison of both sample groups (*).

The comprehensive characterisation of fibrous materials, particularly BiTSAP and BiTSAB, through various cell-based assays, has provided valuable insights into their biocompatibility and potential applications in regenerative medicine. The differential responses observed in the interactions with adipose-derived stem cells (ADSC), Human Umbilical Vein Endothelial Cells (HUVEC), and neural stem cells underscore the material-specific effects on cell behaviour. The visualisation of ADSC and iMR-90 neural stem cells on these materials revealed distinct differences in cell population density, morphology, and distribution. Notably, BiTSAP demonstrated superior biocompatibility, with higher cell population density and more favourable cell spreading compared to BiTSAB. The successful colonisation of BiTSAP by iMR-90 neural stem cells in coherent layers further highlights its potential in neural tissue engineering. The metabolic activity assessments confirmed the cell counting estimates, emphasising the sustained growth and viability of ADSC and HUVEC on BiTSAP, especially after 72 hours. In contrast, BiTSAB exhibited stabilised metabolic activity, with endothelial cells displaying enhanced viability. Furthermore, the successful cocultivation of ADSC with endothelial cells on these materials suggests their potential utilisation in soft tissue engineering. This is particularly relevant in the context of soft tissue prostheses, where the scaffold's influence extends beyond individual cell types, impacting their coexistence and interactions. These findings collectively contribute to a deeper understanding of the biocompatibility and cellular responses of BiTSAP and BiTSAB, offering promising avenues for their application in regenerative medicine, particularly in the domains of neural tissue engineering and soft tissue prostheses.

6 OUTLOOK/FUTURE PROSPECTIVES

As already stated above, the results of this work show high potential in regenerative medicine. Especially regarding the regeneration of neural tissue. For further work, there is also the aim to study animal models *in vivo*. There is already ongoing cooperation between the Department of Nanochemistry and the Physiological Institute of the Academy of Sciences of the Czech Republic and *in vivo* experiments are planned after approval from the Animal Welfare Body of the Institute of Physiology, Czech Academy of Science by the Czech legislation on the protection of animals which complies with Directive 2010/63/EU of the European Parliament and Council. The whole research is planned as a complex study of peripheral nerve regeneration based on multi-criteria approaches (**Figure 65**). The goal of the planned experiments will be devoted to creating an implant construct that will contain a supporting biocompatible material – medically grade silicone. This material will create a support matrix that will be suitable for its mechanical properties but will also serve as a part of the structure that will cover the endings of the severed nerves and keep them in close contact without the need to create a large number of sutures. This construct (in various shapes) will be supplemented with hybrid, organosilane fibres designed to promote the differentiation of stem cells into fetal neuroblasts. It is intended to create and test several shapes of the supporting silicone matrix with different types of organosilane fibres. The final construct tested in terms of shape and mechanical properties supplemented with the most suitable form of organosilane fibres will then be tested *in vivo* on a laboratory rat model.

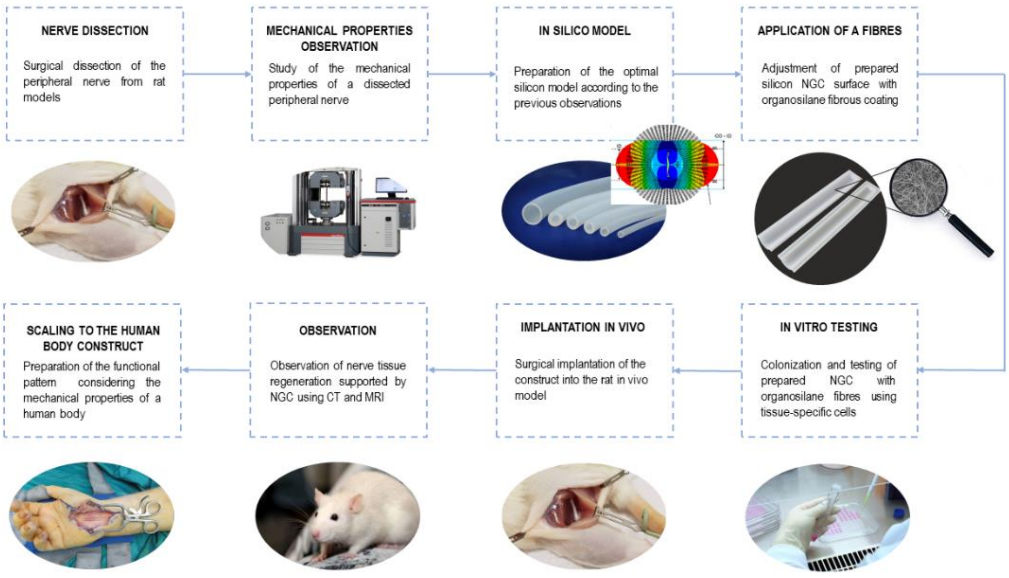

Figure 65 Graphical abstract of planned work in continuing research.

Further research with organosilane fibres is also ongoing in the field of analytical chemistry. Together with the Faculty of Textile Engineering TU Liberec are fibres tested as

potential innovative material for micro-extraction. The sample pre-treatment aims at selective and quantitative isolation of an analyte from the matrix resulting in minimization or even elimination of matrix interferences. Hence, organosilanes could play a major role in this research. They are fulfilling many demands such as chemical stability in many solvents, selectivity, versatility and low financial costs. Due to various chemical properties of organosilanes (depending on their structures), different extraction characteristics can be provided and they can be used for a wide field of analyte extractions.

Research regarding the chemical base of the whole study to stabilise the sol during further processing. The current concept is based on the precise calculation of the amount of water added to the solution during the sol-gel process, which hydrolyses one of the six ethoxy groups in the organosilane molecule. Water molecule is the initiator of the hydrolytic reaction, and in the case of an excess of water, all available ethoxy groups are hydrolysed very quickly, which leads to undesirable gel formation. In such cases, the system is very unstable and prone to gelation even under different environmental conditions, which is a factor that can hardly be influenced. By reducing the number of ethoxy groups in the original organosilane structure to methyl groups or other non-reactive groups, the kinetics of the sol-gel reaction will be slowed down which is a suitable parameter for the different types of electrospinning techniques whereby the change in the morphology occurs. Above mentioned changes in the structure can be seen in **Figure 66**.

Figure 66 Methylated structures of BiTSAB synthesised organosilane precursors.

7 CONCLUSION

Due to the limited ability of the human body to regenerate, the development of materials able to support regeneration or replace permanently damaged parts of the body is desirable. Therefore, today's modern material science requires a comprehensive approach and combination of numerous scientific disciplines to appease the needs of the general population.

The aim of this work was to prepare several types of hybrid fibres from synthesised precursors using the sol-gel process and subsequent electrospinning techniques for applications in medicine. This unique method is described in European patent PS4427EP (Máková, Holubová, Kulhánková; 2021) as well as in Czech PV 2021-160 (Máková, Holubová, Kulhánková; 31.3.2021).

This thesis describes the follow-up research of Assoc. Prof. Máková, PhD and was focused on the synthesis, formation and characterisation of new organosilanes with sterically huge organic components. The aim of the work was also to prepare fibrous structures in 100 mol.% representation of organosilane precursors, i.e. without the need for the addition of tetraethyl orthosilicate (TEOS) to supplement the silica network. The elimination of TEOS has not only simplified the synthetic pathway but has also changed the way for the creation of materials with unique properties tailored for regenerative applications. The comprehensive testing and evaluation conducted on these novel fibrous materials have demonstrated promising results, particularly in the context of regenerative purposes.

Created fibrous materials have proven excellent results in the formation of biomimetic scaffolds, showcasing exceptional biocompatibility and interacting harmoniously with various cell lines, including stem cells. The fibrous structures, synthesised through a sol-gel process with subsequent electrospinning techniques, exhibit properties crucial for regenerative medicine with the ability to provide a supportive microenvironment for cellular proliferation and differentiation.

The outcomes of this research hold great promise for the development of next-generation materials. The success in achieving a 100 mol.% ratio in the creation of these fibrous materials not only represents a significant contribution to the field of material science but also opens new pathways for tailored solutions in tissue engineering and regenerative therapies. The work does not end here; rather, it sets the stage for further exploration and refinement of these materials, with the ultimate goal of translating these advancements into transformative regenerative treatments for the benefit of human health and well-being.

8 REFERENCES

[1] S.V. Bhat, Biomaterials, Alpha Science International, 2002.

[2] B. Ratner, A. Hoffman, F. Schoen, J. Lemons, Biomaterials Science; An Introduction to Materials in Medicine, 3rd ed., Academic Press, 2012.

[3] L. Nair, C. Laurencin, Polymers as biomaterials for tissue engineering and controlled drug delivery., Polymers 102 (2006) 47–90. https://doi.org/10.1007/B137240.

[4] D.F. Williams, On the mechanisms of biocompatibility, Biomaterials 29 (2008) 2941–2953. https://doi.org/10.1016/j.biomaterials.2008.04.023.

[5] J.M. Chai, T.S.M. Amelia, G.K. Mouriya, K. Bhubalan, A.-A.A. Amirul, S. Vigneswari, S. Ramakrishna, Surface-Modified Highly Biocompatible Bacterial-poly(3-hydroxybutyrate-co-4-hydroxybutyrate): A Review on the Promising Next-Generation Biomaterial, Polymers 13 (2021) 51. https://doi.org/10.3390/polym13010051.

[6] M. Faustini, L. Nicole, E. Ruiz-Hitzky, C. Sanchez, History of Organic–Inorganic Hybrid Materials: Prehistory, Art, Science, and Advanced Applications, Advanced Functional Materials 28 (2018) 1704158. https://doi.org/10.1002/adfm.201704158.

[7] J.V. Alemán, A.V. Chadwick, J. He, M. Hess, K. Horie, R.G. Jones, P. Kratochvíl, I. Meisel, I. Mita, G. Moad, S. Penczek, R.F.T. Stepto, Definitions of terms relating to the structure and processing of sols, gels, networks, and inorganic-organic hybrid materials (IUPAC Recommendations 2007), Pure and Applied Chemistry 79 (2007) 1801–1829. https://doi.org/10.1351/pac200779101801.

[8] S. Kalia, Y. Haldorai, Organic-Inorganic Hybrid Nanomaterials, Springer, 2014.

[9] M.F. Ashby, Y.J.M. Bréchet, Designing hybrid materials, Acta Materialia 51 (2003) 5801–5821. https://doi.org/10.1016/S1359-6454(03)00441-5.

[10] M. Iurzhenko, Electrical, thermomechanical and sorption properties of hybrid organic-inorganic systems based on urethane oligomers and silicates, (2009).

[11] G. Kickelbick, Hybrid Materials: Synthesis, Characterization, and Applications, Hoboken, NJ: JohnWiley&Sons, 2007.

[12] Y. Chujo, Organic—inorganic hybrid materials, Current Opinion in Solid State and Materials Science 1 (1996) 806–811. https://doi.org/10.1016/S1359-0286(96)80105-7.

[13] B.F.G. Johnson, Nanoparticles in catalysis, Top. Catal. 24 (2003) 147–159. https://doi.org/10.1023/B:TOCA.0000003086.83434.b6.

[14] A.J. Hart, Hybrid Nanostructure Array, US2013260113 (A1), 2013.

[15] H. Schroeder, Oxide Layers Deposited from Organic Solutions. Physics of Thin Films, in: Physics of Thin Films: Advances in Research and Development, 1969: pp. 80–140.

[16] F. Guo, J. Gao, X. Li, Research progress on titanium-containing organic–inorganic hybrid protective coatings, Surf. Rev. Lett. 26 (2019) 1930002. https://doi.org/10.1142/S0218625X19300028.

[17] X.L. Guével, C. Palazzesi, P. Prosposito, G.D. Giustina, G. Brusatin, Influence of chelating agents on the photopolymerization of hybrid Ti-based waveguides, J. Mater. Chem. 18 (2008) 3556–3562. https://doi.org/10.1039/B802257G.

[18] C. Liu, Y.-Q. Cao, D. Wu, A.-D. Li, Simulation of Biologic Synapse Through Organic-Inorganic Hybrid Memristors Using Novel Ti-Based Maleic Acid/TiO2 Ultrathin Films, IEEE Electron Device Letters 41 (2020) 155–158. https://doi.org/10.1109/LED.2019.2956282.

[19] O. Nilsen, K. Klepper, H. Nielsen, H. Fjellvaåg, Deposition of Organic- Inorganic Hybrid Materials by Atomic Layer Deposition, ECS Trans. 16 (2008) 3–14. https://doi.org/10.1149/1.2979975.

[20] H. Moshe, G. Levi, D. Sharon, Y. Mastai, Atomic layer deposition of enantioselective thin film of alumina on chiral self-assembled-monolayer, Surf. Sci. 629 (2014) 88–93. https://doi.org/10.1016/j.susc.2014.03.027.

[21] J. Hu, L. Yan, W. You, Two-Dimensional Organic–Inorganic Hybrid Perovskites: A New Platform for Optoelectronic Applications, Advanced Materials 30 (2018) 1802041. https://doi.org/10.1002/adma.201802041.

[22] Y.-J. Cao, L. Zhou, L. He, P.-P. Shi, Q. Ye, D.-W. Fu, Phase Transition and Band Gap Regulation by Halogen Substituents on the Organic Cation in Organic–Inorganic Hybrid Perovskite Semiconductors, Chemistry – A European Journal 26 (2020) 14124–14129. https://doi.org/10.1002/chem.202001266.

[23] T. Chang, Y. Dai, Q. Wei, X. Xu, S. Cao, B. Zou, Q. Zhang, R. Zeng, Temperature-Dependent Reversible Optical Properties of Mn-Based Organic–Inorganic Hybrid (C8H20N)2MnCl4 Metal Halides, ACS Appl. Mater. Interfaces 15 (2023) 5487–5494. https://doi.org/10.1021/acsami.2c20885.

[24] E.G. Barrera, P.R. Livotto, J.H.Z. dos Santos, Hybrid silica bearing different organosilanes produced by the modified Stöber method, Powder Technology 301 (2016) 486–492. https://doi.org/10.1016/j.powtec.2016.04.025.

[25] X.M. He, K.L. Xie, Dyeing Properties of Chitosan-Sulfamic Acid Solution Treated Wool with Silane Coupling Agent, Advanced Materials Research 331 (2011) 377–381. https://doi.org/10.4028/www.scientific.net/AMR.331.377.

[26] D. Zhao, F. Wang, P. Liu, S. Hu, C. Hu, L. Yang, Enhanced mechanical properties of polymer-modified cementitious materials via organosilane fly ash hybrid–polyvinyl pyrrolidone crosslink network, Construction and Building Materials 330 (2022) 127119. https://doi.org/10.1016/j.conbuildmat.2022.127119.

[27] L. Huang, R.A. Zingaro, E.A. Meyers, P.K. Nair, M.T.S. Nair, Chemical Deposition of Thin Films of Copper Sulfide on Glass Surfaces Modified with Organosilanes, Phosphorus, Sulfur, and Silicon and the Related Elements 105 (1995) 175–185. https://doi.org/10.1080/10426509508042061.

[28] J. Lee, J.-H. Ha, I.-H. Song, Improving the antifouling properties of ceramic membranes via chemical grafting of organosilanes, Separation Science and Technology 51 (2016) 2420–2428. https://doi.org/10.1080/01496395.2016.1209218.

[29] The use of organosilanes to inhibit metal corrosion. A review, Int. J. Corros. Scale Inhib. 8 (2019). https://doi.org/10.17675/2305-6894-2019-8-4-6.

[30] S. Carli, M. Di Lauro, M. Bianchi, M. Murgia, A. De Salvo, M. Prato, L. Fadiga, F. Biscarini, Water-Based PEDOT:Nafion Dispersion for Organic Bioelectronics, ACS Appl. Mater. Interfaces 12 (2020) 29807–29817. https://doi.org/10.1021/acsami.0c06538.

[31] S. Karamikamkar, H.E. Naguib, C.B. Park, Advances in precursor system for silica-based aerogel production toward improved mechanical properties, customized morphology, and multifunctionality: A review, Adv Colloid Interface Sci 276 (2020) 102101. https://doi.org/10.1016/j.cis.2020.102101.

[32] Y. Hu, Y. Wang, F. Li, C. Ma, J. Wang, Design and expeditious synthesis of organosilanes as potent antivirals targeting multidrug-resistant influenza A viruses, European Journal of Medicinal Chemistry 135 (2017) 70–76. https://doi.org/10.1016/j.ejmech.2017.04.038.

[33] T. Linhares, M.T.P. de Amorim, L. Durães, Silica aerogel composites with embedded fibres: a review on their preparation, properties and applications, J. Mater. Chem. A 7 (2019) 22768–22802. https://doi.org/10.1039/C9TA04811A.

[34] V. Alimardani, S.S. Abolmaali, G. Yousefi, Z. Rahiminezhad, M. Abedi, A. Tamaddon, S. Ahadian, Microneedle Arrays Combined with Nanomedicine Approaches for Transdermal Delivery of Therapeutics, J Clin Med 10 (2021) 181. https://doi.org/10.3390/jcm10020181.

[35] N.P.S. Chauhan, K. Meghwal, Orthopedic Implants, Polymers for, in: 2015.

[36] J.A. González Calderón, D. Contreras López, E. Pérez, J. Vallejo Montesinos, Polysiloxanes as polymer matrices in biomedical engineering: their interesting properties as the reason for the use in medical sciences, Polym. Bull. 77 (2020) 2749–2817. https://doi.org/10.1007/s00289-019-02869-x.

[37] A. Francis, Biological evaluation of preceramic organosilicon polymers for various healthcare and biomedical engineering applications: A review, Journal of Biomedical Materials Research Part B: Applied Biomaterials 109 (2021) 744–764. https://doi.org/10.1002/jbm.b.34740.

[38] A. Simchi, E. Tamjid, F. Pishbin, A.R. Boccaccini, Recent progress in inorganic and composite coatings with bactericidal capability for orthopaedic applications, Nanomedicine: Nanotechnology, Biology and Medicine 7 (2011) 22–39. https://doi.org/10.1016/j.nano.2010.10.005.

[39] K.-H. Haas, S. Amberg-Schwab, K. Rose, G. Schottner, Functionalized coatings based on inorganic–organic polymers (ORMOCER®s) and their combination with vapor deposited inorganic thin films, Surface and Coatings Technology 111 (1999) 72–79. https://doi.org/10.1016/S0257-8972(98)00711-7.

[40] V. Máková, B. Holubová, I. Krabicová, J. Kulhánková, M. Řezanka, Hybrid organosilane fibrous materials and their contribution to modern science, 228 (2021). https://doi.org/10.1016/j.polymer.2021.123862.

[41] B. Holubová, V. Máková, J. Müllerová, J. Brus, K. Havlíčková, V. Jenčová, A. Michalcová, J. Kulhánková, M. Řezanka, Novel chapter in hybrid materials: One-pot synthesis of purely organosilane fibers, Polymer 190 (2020) 122234. https://doi.org/10.1016/j.polymer.2020.122234.

[42] S. Fujita, S. Inagaki, Self-Organization of Organosilica Solids with Molecular-Scale and Mesoscale Periodicities, Chem. Mater. 20 (2008) 891–908. https://doi.org/10.1021/cm702271v.

[43] F. Tama, F.X. Gadea, O. Marques, Y.-H. Sanejouand, Building-block approach for determining low-frequency normal modes of macromolecules, Proteins: Structure, Function, and Bioinformatics 41 (2000) 1–7. https://doi.org/10.1002/1097-0134(20001001)41:1<1::AID-PROT10>3.0.CO;2-P.

[44] D.G. Wilkinson, In Situ Hybridization: A Practical Approach, OUP Oxford, 1998.

[45] J.B. Helmont, Opuscula medica inaudita. I. De lithiasi. II. De febribus. III. De humoribus Galeni. IV. De peste. Editio secunda multò emendatior. ed., (1648).

[46] J.J. Ebelmen, Untersuchungen über die Verbindungen der Borsäure und Kieselsäure mit Aether, Annalen der Chemie und Pharmacie 57 (1846) 319–355.

[47] P. Cheben, M.L. Calvo, A photopolymerizable glass with diffraction efficiency near 100% for holographic storage, Appl. Phys. Lett. 78 (2001) 1490–1492. https://doi.org/10.1063/1.1354665.

[48] J.J. Petkowski, W. Bains, S. Seager, On the Potential of Silicon as a Building Block for Life, Life 10 (2020) 84. https://doi.org/10.3390/life10060084.

[49] Web of Science, Www.Webofscience.Com (n.d.).

[50] B. Findik, V. Cinquin, F. Gyppaz, C. Carrot, V. Bounor-Legaré, Solvent free sol-gel based synthesis of soft magnesium silicate, J Sol-Gel Sci Technol 103 (2022) 921–934. https://doi.org/10.1007/s10971-022-05852-7.

[51] C.J. Brinker, Hydrolysis and condensation of silicates: Effects on structure, Journal of Non-Crystalline Solids 100 (1988) 31–50. https://doi.org/10.1016/0022-3093(88)90005-1.

[52] M. Guglielmi, G. Carturan, Precursors for sol-gel preparations, Journal of Non-Crystalline Solids 100 (1988) 16–30. https://doi.org/10.1016/0022-3093(88)90004-X.

[53] A. Chládová, J. Wiener, J. Luthuli, V. Máková, Dyeing of glass fibres by the sol gel method, Autex Research Journal 11 (2011).

[54] X. Cheng, D. Chen, Y. Liu, Mechanisms of Silicon Alkoxide Hydrolysis–Oligomerization Reactions: A DFT Investigation, ChemPhysChem 13 (2012) 2392–2404. https://doi.org/10.1002/cphc.201200115.

[55] J. Livage, M. Henry, C. Sanchez, Sol-gel chemistry of transition metal oxides, Progress in Solid State Chemistry 18 (1988) 259–341. https://doi.org/10.1016/0079-6786(88)90005-2.

[56] A.C. Pierre, G.M. Pajonk, Chemistry of Aerogels and Their Applications, Chem. Rev. 102 (2002) 4243–4266. https://doi.org/10.1021/cr0101306.

[57] T.W. Zerda, G. Hoang, High-pressure raman study of the hydrolysis reaction in tetramethylorthosilicate (TMOS), Journal of Non-Crystalline Solids 109 (1989) 9–17. https://doi.org/10.1016/0022-3093(89)90435-3.

[58] M. Pantoja, F. Velasco, D. Broekema, J. Abenojar, J.C. del Real, The Influence of pH on the Hydrolysis Process of γ-Methacryloxypropyltrimethoxysilane, Analyzed by FT-IR, and the Silanization of Electrogalvanized Steel, Journal of Adhesion Science and Technology 24 (2010) 1131–1143. https://doi.org/10.1163/016942409X12586283821559.

[59] R. Aelion, A. Loebel, F. Eirich, Hydrolysis of Ethyl Silicate, 72 (1950) 5707–5712.

[60] E.J.A. Pope, J.D. Mackenzie, Sol-gel processing of silica: II. The role of the catalyst, Journal of Non-Crystalline Solids 87 (1986) 185–198. https://doi.org/10.1016/S0022-3093(86)80078-3.

[61] W.T. Grubb, A Rate Study of the Silanol Condensation Reaction at 25° in Alcoholic Solvents1, ACS Publications (2002). https://doi.org/10.1021/ja01642a014.

[62] G. Engelhardt, W. Altenburg, D. Hoebbel, W. Wieker, 29Si-NMR-Spektroskopie an Silicatlösungen. IV. Untersuchungen zur Kondensation der Monokieselsäure, Zeitschrift für anorganische und allgemeine Chemie 428 (1977) 43–52. https://doi.org/10.1002/zaac.19774280105.

[63] D. Stoye, Solvents, in: Wiley-VCH Verlag GmbH & Co. KGaA (Ed.), Ullmann's Encyclopedia of Industrial Chemistry, Wiley-VCH Verlag GmbH & Co. KGaA, Weinheim, Germany, 2000: p. a24_437. https://doi.org/10.1002/14356007.a24_437.

[64] I. Artaki, T.W. Zerda, J. Jonas, Solvent effects on the condensation stage of the sol-gel process, Journal of Non-Crystalline Solids 81 (1986) 381–395. https://doi.org/10.1016/0022-3093(86)90504-1.

[65] J.S. Lee, K.H. Choi, H.D. Ghim, S.S. Kim, D.H. Chun, H.Y. Kim, W.S. Lyoo, Role of molecular weight of atactic poly(vinyl alcohol) (PVA) in the structure and properties of PVA nanofabric prepared by electrospinning, Journal of Applied Polymer Science 93 (2004) 1638–1646. https://doi.org/10.1002/app.20602.

[66] J.C. Pouxviel, J.P. Boilot, Kinetic simulations and mechanisms of the sol-gel polymerization, Journal of Non-Crystalline Solids 94 (1987) 374–386. https://doi.org/10.1016/S0022-3093(87)80072-8.

[67] P.M. Glaser, C.G. Pantano, Effect of the H2O/TEOS ratio upon the preparation and nitridation of silica sol/gel films, Journal of Non-Crystalline Solids 63 (1984) 209–221. https://doi.org/10.1016/0022-3093(84)90400-9.

[68] C. Bogatu, THE INFLUENCE OF PARAMETERS IN SILICA SOL-GEL PROCESS, Bull. Transilv. Univ. Bras. 2011 (2011) 53.

[69] K. Vogel, T. Greinert, H. Harms, G. Sadowski, C. Held, T. Maskow, Influence of cytosolic conditions on the reaction equilibrium and the reaction enthalpy of the enolase reaction accessed by calorimetry and van ‘t HOFF, Biochimica et Biophysica Acta (BBA) - General Subjects 1864 (2020) 129675. https://doi.org/10.1016/j.bbagen.2020.129675.

[70] J. Rodenburg, M. Dijkstra, R. van Roij, Van’t Hoff’s law for active suspensions: the role of the solvent chemical potential, Soft Matter 13 (2017) 8957–8963. https://doi.org/10.1039/C7SM01432E.

[71] J.H. Hoff, Studies in Chemical Dynamics, Chemical publishing Company, 1896.

[72] A.A. Issa, A.S. Luyt, Kinetics of Alkoxysilanes and Organoalkoxysilanes Polymerization: A Review, Polymers 11 (2019) 537. https://doi.org/10.3390/polym11030537.

[73] I.S. Ignatyev, M. Montejo, J.J.L. González, Theoretical study of the mechanisms of the hydrolysis and condensation reactions of silicon and titanium alkoxides: similarities and differences, Dalton Trans. 39 (2010) 6967–6973. https://doi.org/10.1039/C002397C.

[74] S. Okumoto, N. Fujita, S. Yamabe, Theoretical Study of Hydrolysis and Condensation of Silicon Alkoxides, J. Phys. Chem. A 102 (1998) 3991–3998. https://doi.org/10.1021/jp980705b.

[75] D.E. Resasco, L. Balzano, J.E. Herrera, O. Matarredona, L. Zheng, Controlled growth of SWCNT on solid catalysts with narrow (n,m) distribution, in: H. Kuzmany, J. Fink, M. Mehring, S. Roth (Eds.), Electronic Properties of Synthetic Nanostructures, Amer Inst Physics, Melville, 2004: pp. 27–31.

[76] A.A. Issa, M.S. Elazazy, A.S. Luyt, Polymerization of 3-cyanopropyl (triethoxy) silane: A kinetic study using gas chromatography, International Journal of Chemical Kinetics 50 (2018) 846–855. https://doi.org/10.1002/kin.21219.

[77] S. Sakka, K. Kamiya, The sol-gel transition in the hydrolysis of metal alkoxides in relation to the formation of glass fibers and films, Journal of Non-Crystalline Solids 48 (1982) 31–46. https://doi.org/10.1016/0022-3093(82)90244-7.

[78] A.E. Danks, S.R. Hall, Z. Schnepp, The evolution of 'sol–gel' chemistry as a technique for materials synthesis, Mater. Horiz. 3 (2016) 91–112. https://doi.org/10.1039/C5MH00260E.

[79] R.A. Assink, B.D. Kay, Sol-gel kinetics I. Functional group kinetics, Journal of Non-Crystalline Solids 99 (1988) 359–370. https://doi.org/10.1016/0022-3093(88)90441-3.

[80] B.D. Kay, R.A. Assink, Sol-gel kinetics: II. Chemical speciation modeling, Journal of Non-Crystalline Solids 104 (1988) 112–122. https://doi.org/10.1016/0022-3093(88)90189-5.

[81] R.A. Assink, B.D. Kay, Sol-gel kinetics III. Test of the statistical reaction model, Journal of Non-Crystalline Solids 107 (1988) 35–40. https://doi.org/10.1016/0022-3093(88)90089-0.

[82] N. Bhardwaj, S.C. Kundu, Electrospinning: A fascinating fiber fabrication technique, Biotechnology Advances 28 (2010) 325–347. https://doi.org/10.1016/j.biotechadv.2010.01.004.

[83] J. Xue, T. Wu, Y. Dai, Y. Xia, Electrospinning and Electrospun Nanofibers: Methods, Materials, and Applications, Chem Rev 119 (2019) 5298–5415. https://doi.org/10.1021/acs.chemrev.8b00593.

[84] W. Ali, R. Gadkari, S. Arora, V. Somkuwar, A. Chowdhury, Antibacterial Electrospun Nanofibres, in: Inamuddin, M.I. Ahamed, R. Prasad (Eds.), Advanced Antimicrobial Materials and Applications, Springer, Singapore, 2021: pp. 239–255. https://doi.org/10.1007/978-981-15-7098-8_10.

[85] A. Formhals, Process and apparatus for preparing artificial threads, US 1975504A, 1934.

[86] D.P. Dowling, I.S. Miller, M. Ardhaoui, W.M. Gallagher, Effect of Surface Wettability and Topography on the Adhesion of Osteosarcoma Cells on Plasma-modified Polystyrene, J Biomater Appl 26 (2011) 327–347. https://doi.org/10.1177/0885328210372148.

[87] F.-L. Zhou, R.-H. Gong, I. Porat, Needle and needleless electrospinning for nanofibers, Journal of Applied Polymer Science 115 (2010) 2591–2598. https://doi.org/10.1002/app.31282.

[88] O. Jirsák, F. Sanetrník, D. Lukáš, V. Kotek, L. Martinová, J. Chaloupek, Method of nanofibres production from a polymer solution using electrostatic spinning and a device for carrying out the method, US 7585437 B2, n.d.

[89] H.S. SalehHudin, E.N. Mohamad, W.N.L. Mahadi, A. Muhammad Afifi, Multiple-jet electrospinning methods for nanofiber processing: A review, Materials and Manufacturing Processes 33 (2018) 479–498. https://doi.org/10.1080/10426914.2017.1388523.

[90] P. Pokorny, E. Kostakova, F. Sanetrnik, P. Mikes, J. Chvojka, T. Kalous, M. Bilek, K. Pejchar, J. Valtera, D. Lukas, Effective AC needleless and collectorless electrospinning for yarn production, Phys. Chem. Chem. Phys. 16 (2014) 26816–26822. https://doi.org/10.1039/C4CP04346D.

[91] Z.-F. Ren, B.-Z. Liu, G.-Q. Liu, Y.-X. Kang, H.-Y. Fan, H.-M. Li, Effect of magnetic force on stability of the electrospinning process, The Journal of The Textile Institute 101 (2010) 571–574. https://doi.org/10.1080/00405000802605072.

[92] C. Lawson, A. Stanishevsky, M. Sivan, P. Pokorny, D. Lukáš, Rapid fabrication of poly(ε-caprolactone) nanofibers using needleless alternating current electrospinning, Journal of Applied Polymer Science 133 (2016). https://doi.org/10.1002/app.43232.

[93] D. Lukáš, A. Sarkar, L. Martinová, K. Vodsed'álková, D. Lubasová, J. Chaloupek, P. Pokorný, P. Mikeš, J. Chvojka, M. Komárek, Physical principles of electrospinning (Electrospinning as a nano-scale technology of the twenty-first century), Textile Progress 41 (2009) 59–140. https://doi.org/10.1080/00405160902904641.

[94] Q. Yang, X. Jiang, F. Gu, Z. Ma, J. Zhang, L. Tong, Polymer micro or nanofibers for optical device applications, Journal of Applied Polymer Science 110 (2008) 1080–1084. https://doi.org/10.1002/app.28716.

[95] X. Geng, O.-H. Kwon, J. Jang, Electrospinning of chitosan dissolved in concentrated acetic acid solution, Biomaterials 26 (2005) 5427–5432. https://doi.org/10.1016/j.biomaterials.2005.01.066.

[96] C.S. Ki, D.H. Baek, K.D. Gang, K.H. Lee, I.C. Um, Y.H. Park, Characterization of gelatin nanofiber prepared from gelatin–formic acid solution, Polymer 46 (2005) 5094–5102. https://doi.org/10.1016/j.polymer.2005.04.040.

[97] A. Atala, Regenerative medicine strategies, Journal of Pediatric Surgery 47 (2012) 17–28. https://doi.org/10.1016/j.jpedsurg.2011.10.013.

[98] A.S. Mao, D.J. Mooney, Regenerative medicine: Current therapies and future directions, Proceedings of the National Academy of Sciences 112 (2015) 14452–14459. https://doi.org/10.1073/pnas.1508520112.

[99] I.A. Ansari, A.K. Datta, An Overview of Sterilization Methods for Packaging Materials Used in Aseptic Packaging Systems, Food and Bioproducts Processing 81 (2003) 57–65. https://doi.org/10.1205/096030803765208670.

[100] J.-I. Sasaki, S. Imazato, Autoclave sterilization of dental handpieces: A literature review, Journal of Prosthodontic Research 64 (2020) 239–242. https://doi.org/10.1016/j.jpor.2019.07.013.

[101] G. Panta, A.K. Richardson, I.C. Shaw, Effectiveness of autoclaving in sterilizing reusable medical devices in healthcare facilities, The Journal of Infection in Developing Countries 13 (2019) 858–864. https://doi.org/10.3855/jidc.11433.

[102] M. Sadeque, S.K. Balachandran, 10 - Overview of medical device processing, in: P.S. Timiri Shanmugam, L. Chokkalingam, P. Bakthavachalam (Eds.), Trends in Development of Medical Devices, Academic Press, 2020: pp. 177–188. https://doi.org/10.1016/B978-0-12-820960-8.00010-1.

[103] V.R. Sastri, 4 - Material Requirements for Plastics Used in Medical Devices, in: V.R. Sastri (Ed.), Plastics in Medical Devices (Third Edition), William Andrew Publishing, 2022: pp. 65–112. https://doi.org/10.1016/B978-0-323-85126-8.00008-4.

[104] J. Koller, EFFECTS OF RADIATION ON THE INTEGRITY AND FUNCTIONALITY OF AMNION AND SKIN GRAFTS, in: J.F. Kennedy, G.O. Phillips, P.A. Williams (Eds.), Sterilisation of Tissues Using Ionising Radiations, Woodhead Publishing, 2005: pp. 197–220. https://doi.org/10.1533/9781845690779.3.197.

[105] R. Brinston, A. Miller, C. Deeley, Developments in radiation sterilisation, Med Device Technol 19 (2008) 36–37.

[106] E. Stoffels, R.E.J. Sladek, I.E. Kieft, Gas Plasma Effects on Living Cells, Phys. Scr. 2004 (2004) 79. https://doi.org/10.1238/Physica.Topical.107a00079.

[107] D. Śladowski, I. Grabska-Liberek, J. Olkowska-Truchanowicz, K. Lipski, G. Gut, An Evaluation of Sterilisation Processes, Altern Lab Anim 36 (2008) 585–590. https://doi.org/10.1177/026119290803600513.

[108] M. Berovic, Sterilisation in biotechnology, in: Biotechnology Annual Review, Elsevier, 2005: pp. 257–279. https://doi.org/10.1016/S1387-2656(05)11008-4.

[109] D. Rohanová, D. Horkavcová, A. Helebrant, A.R. Boccaccini, Assessment of in vitro testing approaches for bioactive inorganic materials, Journal of Non-Crystalline Solids 432 (2016) 53–59. https://doi.org/10.1016/j.jnoncrysol.2015.03.016.

[110] T. Kokubo, H. Takadama, How useful is SBF in predicting in vivo bone bioactivity?, Biomaterials 27 (2006) 2907–2915. https://doi.org/10.1016/j.biomaterials.2006.01.017.

[111] T. Kokubo, Bioactive glass ceramics: properties and applications, Biomaterials 12 (1991) 155–163. https://doi.org/10.1016/0142-9612(91)90194-F.

[112] M. Ogino, F. Ohuchi, L.L. Hench, Compositional dependence of the formation of calcium phosphate films on bioglass, J. Biomed. Mater. Res. 14 (1980) 55–64. https://doi.org/10.1002/jbm.820140107.

[113] J.M. Anderson, 9.19 - Biocompatibility, in: K. Matyjaszewski, M. Möller (Eds.), Polymer Science: A Comprehensive Reference, Elsevier, Amsterdam, 2012: pp. 363–383. https://doi.org/10.1016/B978-0-444-53349-4.00229-6.

[114] B. Huzum, B. Puha, R.M. Necoara, S. Gheorghevici, G. Puha, A. Filip, P.D. Sirbu, O. Alexa, Biocompatibility assessment of biomaterials used in orthopedic devices: An overview (Review), Exp Ther Med 22 (2021) 1315. https://doi.org/10.3892/etm.2021.10750.

[115] F.A. Barile, Introduction to In Vitro Cytotoxicology: Mechanisms and Methods, CRC Press, 2019.

[116] A. Bruinink, R. Luginbuehl, Evaluation of Biocompatibility Using In Vitro Methods: Interpretation and Limitations, in: C. Kasper, F. Witte, R. Pörtner (Eds.), Tissue Engineering III: Cell - Surface Interactions for Tissue Culture, Springer, Berlin, Heidelberg, 2012: pp. 117–152. https://doi.org/10.1007/10_2011_111.

[117] S.K. Bhatia, A.B. Yetter, Correlation of visual in vitro cytotoxicity ratings of biomaterials with quantitative in vitro cell viability measurements, Cell Biol Toxicol 24 (2008) 315–319. https://doi.org/10.1007/s10565-007-9040-z.

[118] B. Hexig, R. Nakaoka, T. Tsuchiya, Safety evaluation of surgical materials by cytotoxicity testing, J Artif Organs 11 (2008) 204–211. https://doi.org/10.1007/s10047-008-0429-0.

[119] W. LI, J. ZHOU, Y. XU, Study of the in vitro cytotoxicity testing of medical devices, Biomed Rep 3 (2015) 617–620. https://doi.org/10.3892/br.2015.481.

[120] B. Alberts, D. Bray, K. Hopkin, A.D. Johnson, J. Lewis, M. Raff, K. Roberts, P. Walter, Essential Cell Biology, Garland Science, 2015.

[121] S.E. DiCarlo, Cell biology should be taught as science is practised, Nat Rev Mol Cell Biol 7 (2006) 290–296. https://doi.org/10.1038/nrm1856.

[122] K.M. Marks, G.P. Nolan, Chemical labeling strategies for cell biology, Nat Methods 3 (2006) 591–596. https://doi.org/10.1038/nmeth906.

[123] Y. Dudai, Universal learning mechanisms: From genes to molecular switches, in: A. Goldbeter (Ed.), Cell to Cell Signalling, Academic Press, 1989: pp. 99–108. https://doi.org/10.1016/B978-0-12-287960-9.50014-9.

[124] R.L.P. Adams, Cell Culture for Biochemists, Elsevier, 1990.

[125] L. Hertz, B.H.J. Juurlink, S. Szuchet, Cell Cultures, in: A. Lajtha (Ed.), Neurochemical Systems, Springer US, Boston, MA, 1985: pp. 603–661. https://doi.org/10.1007/978-1-4684-7018-5_23.

[126] G. Kaur, J.M. Dufour, Cell lines, Spermatogenesis 2 (2012) 1–5. https://doi.org/10.4161/spmg.19885.

[127] J.-P. Gillet, S. Varma, M.M. Gottesman, The Clinical Relevance of Cancer Cell Lines, JNCI: Journal of the National Cancer Institute 105 (2013) 452–458. https://doi.org/10.1093/jnci/djt007.

[128] D.M. Peehl, Primary cell cultures as models of prostate cancer development, Endocrine-Related Cancer 12 (2005) 19–47. https://doi.org/10.1677/erc.1.00795.

[129] G. Stacey, Primary Cell Cultures and Immortal Cell Lines, in: Encyclopedia of Life Sciences, John Wiley & Sons, Ltd, 2006. https://doi.org/10.1038/npg.els.0003960.

[130] L. Margulis, The Origin of Plant and Animal Cells: The serial symbiosis view of the origin of higher cells suggests that the customary division of living things into two kingdoms should be reconsidered, American Scientist 59 (1971) 230–235.

[131] R. Langer, D.A. Tirrell, Designing materials for biology and medicine, Nature 428 (2004) 487–492. https://doi.org/10.1038/nature02388.

[132] J.M. Anderson, Biological Responses to Materials, Annual Review of Materials Research 31 (2001) 81–110. https://doi.org/10.1146/annurev.matsci.31.1.81.

[133] G. Chan, D.J. Mooney, New materials for tissue engineering: towards greater control over the biological response, Trends in Biotechnology 26 (2008) 382–392. https://doi.org/10.1016/j.tibtech.2008.03.011.

[134] S. Saeidnia, A. Manayi, M. Abdollahi, From in vitro Experiments to in vivo and Clinical Studies; Pros and Cons, Current Drug Discovery Technologies 12 (2015) 218–224.

[135] M. Szycher, A.M. Reed, A.A. Siciliano, In vivo Testing of a Biostable Polyurethane, J Biomater Appl 6 (1991) 110–130. https://doi.org/10.1177/088532829100600202.

[136] C. Kilkenny, W. Browne, I.C. Cuthill, M. Emerson, D.G. Altman, Animal research: Reporting in vivo experiments: The ARRIVE guidelines, Br J Pharmacol 160 (2010) 1577–1579. https://doi.org/10.1111/j.1476-5381.2010.00872.x.

[137] C.A. Vilela, C. Correia, J.M. Oliveira, R.A. Sousa, J. Espregueira-Mendes, R.L. Reis, Cartilage Repair Using Hydrogels: A Critical Review of in Vivo Experimental Designs, ACS Biomater. Sci. Eng. 1 (2015) 726–739. https://doi.org/10.1021/acsbiomaterials.5b00245.

[138] D. p. Lovell, G. Thomas, R. Dubow, Issues related to the experimental design and subsequent statistical analysis of in vivo and in vitro comet studies, Teratogenesis, Carcinogenesis, and Mutagenesis 19 (1999) 109–119. https://doi.org/10.1002/(SICI)1520-6866(1999)19:2<109::AID-TCM4>3.0.CO;2-5.

[139] S. Tao, G. Li, J. Yin, Fluorescent nanofibrous membranes for trace detection of TNT vapor, J. Mater. Chem. 17 (2007) 2730–2736. https://doi.org/10.1039/B618122H.

[140] C. Schramm, B. Rinderer, R. Tessadri, Synthesis and characterization of novel ultrathin polyimide fibers via sol–gel process and electrospinning, Journal of Applied Polymer Science 128 (2013) 1274–1281. https://doi.org/10.1002/app.38543.

[141] C. Schramm, B. Rinderer, R. Tessadri, Synthesis and characterization of hydrophobic, ultra-fine fibres based on an organic–inorganic nanocomposite containing a polyimide functionality, Polymers and Polymer Composites 27 (2019) 268–278. https://doi.org/10.1177/0967391119832408.

[142] M. Travnickova, J. Pajorova, J. Zarubova, N. Krocilova, M. Molitor, L. Bacakova, The Influence of Negative Pressure and of the Harvesting Site on the Characteristics of Human Adipose Tissue-Derived Stromal Cells from Lipoaspirates, Stem Cells International 2020 (2020) e1016231. https://doi.org/10.1155/2020/1016231.

[143] J. Yu, M.A. Vodyanik, K. Smuga-Otto, J. Antosiewicz-Bourget, J.L. Frane, S. Tian, J. Nie, G.A. Jonsdottir, V. Ruotti, R. Stewart, I.I. Slukvin, J.A. Thomson, Induced Pluripotent Stem Cell Lines Derived from Human Somatic Cells, Science 318 (2007) 1917–1920. https://doi.org/10.1126/science.1151526.

[144] J. Polentes, P. Jendelova, M. Cailleret, H. Braun, N. Romanyuk, P. Tropel, M. Brenot, V. Itier, C. Seminatore, K. Baldauf, K. Turnovcova, D. Jirak, M. Teletin, J. Côme, J. Tournois, K. Reymann, E. Sykova, S. Viville, B. Onteniente, Human induced pluripotent stem cells improve stroke outcome and reduce secondary degeneration in the recipient brain, Cell Transplant 21 (2012) 2587–2602. https://doi.org/10.3727/096368912X653228.

[145] J. Lin, C. Peng, S. Ravi, A.K.M.N.A. Siddiki, J. Zheng, K.J. Balkus, Biphenyl Wrinkled Mesoporous Silica Nanoparticles for pH-Responsive Doxorubicin Drug Delivery, Materials 13 (2020) 1998. https://doi.org/10.3390/ma13081998.

[146] Y. Cao, Y. Duan, L. Han, S. Che, Hierarchical chirality transfer in the formation of chiral silica fibres with DNA-porphyrin co-templates, Chem. Commun. 53 (2017) 5641–5644. https://doi.org/10.1039/c7cc02382k.

[147] Â. Novais, A.R. Freitas, C. Rodrigues, L. Peixe, Fourier transform infrared spectroscopy: unlocking fundamentals and prospects for bacterial strain typing, Eur J Clin Microbiol Infect Dis 38 (2019) 427–448. https://doi.org/10.1007/s10096-018-3431-3.

[148] P. Innocenzi, Infrared spectroscopy of sol–gel derived silica-based films: a spectra-microstructure overview, Journal of Non-Crystalline Solids 316 (2003) 309–319. https://doi.org/10.1016/S0022-3093(02)01637-X.

[149] R. Al-Oweini, H. El-Rassy, Synthesis and characterization by FTIR spectroscopy of silica aerogels prepared using several Si(OR)4 and R″Si(OR′)3 precursors, Journal of Molecular Structure 919 (2009) 140–145. https://doi.org/10.1016/j.molstruc.2008.08.025.

[150] M.E. Lynch, D.C. Folz, D.E. Clark, Use of FTIR reflectance spectroscopy to monitor corrosion mechanisms on glass surfaces, Journal of Non-Crystalline Solids 353 (2007) 2667–2674. https://doi.org/10.1016/j.jnoncrysol.2007.05.012.

[151] C.T. Lee, D.E. Clark, Characterization of glass surfaces, Applications of Surface Science 20 (1985) 397–412. https://doi.org/10.1016/0378-5963(85)90164-3.

[152] G. Lelong, Detecting non-bridging oxygens: non-resonant inelastic X-ray scattering in crystalline lithium borates, Inorganic Chemistry (2014).

[153] M.P. Huber, S. Kelch, H. Berke, FTIR investigations on hydrolysis and condensation reactions of alkoxysilane terminated polymers for use in adhesives and sealants, International Journal of Adhesion and Adhesives 64 (2016) 153–162. https://doi.org/10.1016/j.ijadhadh.2015.10.014.

[154] A. Fidalgo, L.M. Ilharco, The defect structure of sol–gel-derived silica/polytetrahydrofuran hybrid films by FTIR, Journal of Non-Crystalline Solids 283 (2001) 144–154. https://doi.org/10.1016/S0022-3093(01)00418-5.

[155] H. Jiang, Z. Zheng, X. Wang, Kinetic study of methyltriethoxysilane (MTES) hydrolysis by FTIR spectroscopy under different temperatures and solvents, Vibrational Spectroscopy 1 (2008) 1–7. https://doi.org/10.1016/j.vibspec.2007.07.002.

[156] M.I. Tejedor-Tejedor, L. Paredes, M.A. Anderson, Evaluation of ATR−FTIR Spectroscopy as an “in Situ” Tool for Following the Hydrolysis and Condensation of Alkoxysilanes under Rich H2O Conditions, Chem. Mater. 10 (1998) 3410–3421. https://doi.org/10.1021/cm980146l.

[157] H. Dong, Z. Zhang, M.-H. Lee, D.W. Mueller, R.F. Reidy, Sol-gel polycondensation of methyltrimethoxysilane in ethanol studied by 29Si NMR spectroscopy using a two-step acid/base procedure, J Sol-Gel Sci Technol 41 (2007) 11–17. https://doi.org/10.1007/s10971-006-0115-8.

[158] J. Brus, J. Karhan, P. Kotlík, ^{29}Si NMR Study of Distribution of Oligomers in Polycondensation of Tetraethoxysilane, Collect. Czech. Chem. Commun. 61 (1996) 691–703. https://doi.org/10.1135/cccc19960691.

[159] W.-R. Zhuang, Y. Wang, P.-F. Cui, L. Xing, J. Lee, D. Kim, H.-L. Jiang, Y.-K. Oh, Applications of π-π stacking interactions in the design of drug-delivery systems, Journal of Controlled Release 294 (2019) 311–326. https://doi.org/10.1016/j.jconrel.2018.12.014.

[160] S. Grimme, Do Special Noncovalent π–π Stacking Interactions Really Exist?, Angewandte Chemie International Edition 47 (2008) 3430–3434. https://doi.org/10.1002/anie.200705157.

[161] J. Širc, R. Hobzová, N. Kostina, M. Munzarová, M. Juklíčková, M. Lhotka, Š. Kubinová, A. Zajícová, J. Michálek, Morphological Characterization of Nanofibers:

Methods and Application in Practice, Journal of Nanomaterials 2012 (2012) e327369. https://doi.org/10.1155/2012/327369.

[162] J.G. Roth, M.S. Huang, T.L. Li, V.R. Feig, Y. Jiang, B. Cui, H.T. Greely, Z. Bao, S.P. Paşca, S.C. Heilshorn, Advancing models of neural development with biomaterials, Nat Rev Neurosci 22 (2021) 593–615. https://doi.org/10.1038/s41583-021-00496-y.

[163] A. Abdal-hay Ali, F. A.Sheikh, N. Gómez-Cerezo, A. Alneairi, M. Luqman, H. Pant, S. Ivanovski, A Review of Protein Adsorption and Bioactivity Charzxczacteristics of Poly ε-caprolactone Scaffolds in Regenerative Medicine, European Polymer Journal 162 (2021) 110892. https://doi.org/10.1016/j.eurpolymj.2021.110892.

[164] M. Mochane, T. Motsoeneng, R. Sadiku, M. Teboho, J. Sefadi, Morphology and Properties of Electrospun PCL and Its Composites for Medical Applications: A Mini Review, Applied Sciences 9 (2019) 2205. https://doi.org/10.3390/app9112205.

[165] S. Agarwal, J.H. Wendorff, A. Greiner, Use of electrospinning technique for biomedical applications, Polymer 49 (2008) 5603–5621. https://doi.org/10.1016/j.polymer.2008.09.014.

[166] S. Sakai, Y. Yamada, T. Yamaguchi, K. Kawakami, Prospective use of electrospun ultra-fine silicate fibers for bone tissue engineering, Biotechnology Journal 1 (2006) 958–962. https://doi.org/10.1002/biot.200600054.

[167] R. Ciriminna, A. Fidalgo, V. Pandarus, F. Béland, L.M. Ilharco, M. Pagliaro, The sol-gel route to advanced silica-based materials and recent applications, Chem Rev 113 (2013) 6592–6620. https://doi.org/10.1021/cr300399c.

[168] C. Pavan, M. Delle Piane, M. Gullo, F. Filippi, B. Fubini, P. Hoet, C. Horwell, F. Huaux, D. Lison, C. Lo Giudice, G. Martra, E. Montfort, R. Schins, M. Sulpizi, K. Wegner, M. Wyart-Remy, C. Ziemann, F. Turci, The puzzling issue of silica toxicity: are silanols bridging the gaps between surface states and pathogenicity?, Particle and Fibre Toxicology 16 (2019). https://doi.org/10.1186/s12989-019-0315-3.

[169] R. Morais, S. Hochheim, C. Camargo de Oliveira, I. Riegel-Vidotti, C. Marino, Skin interaction, permeation, and toxicity of silica nanoparticles: Challenges and recent therapeutic and cosmetic advances, International Journal of Pharmaceutics 614 (2022) 121439. https://doi.org/10.1016/j.ijpharm.2021.121439.

[170] H. Shinto, T. Fukasawa, K. Yoshisue, M. Tezuka, M. Orita, Cell membrane disruption induced by amorphous silica nanoparticles in erythrocytes, lymphocytes, malignant melanocytes, and macrophages, Advanced Powder Technology 25 (2014). https://doi.org/10.1016/j.apt.2014.09.002.

The following AI-based programs were used to check the grammatical correctness of the text in the English language: Writefull, Grammarly, ChatGPT 3.5

9 SUPPLEMENTARY MATERIALS

9.1 ^{1}H liquid state NMR spectra of synthesised precursor

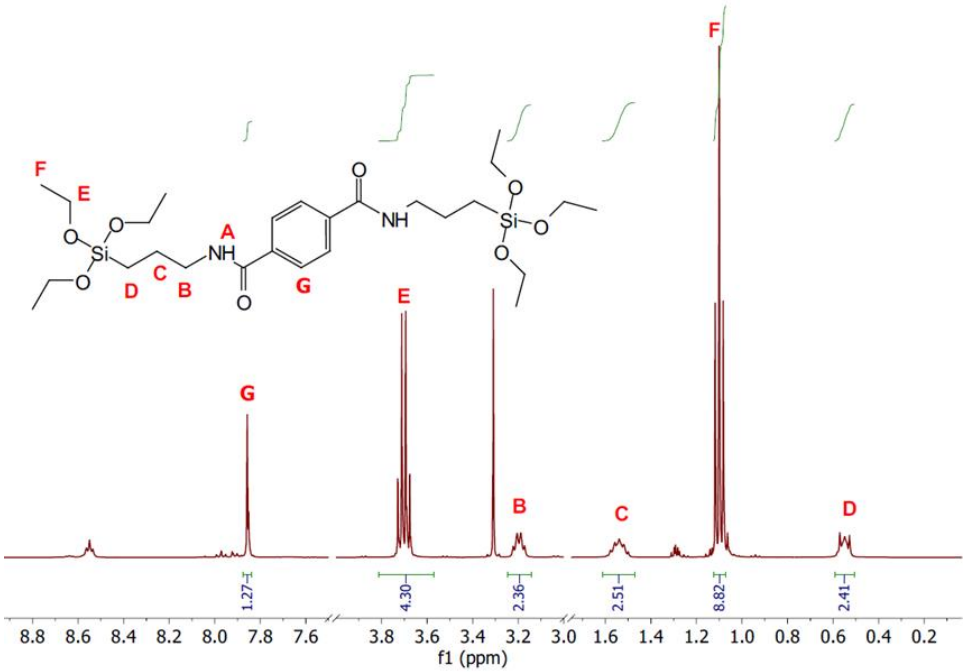

Figure S1 Spectrum of the ^{1}H liquid state NMR of the synthesised BiTSAB precursor measured in DMSO-d_6.

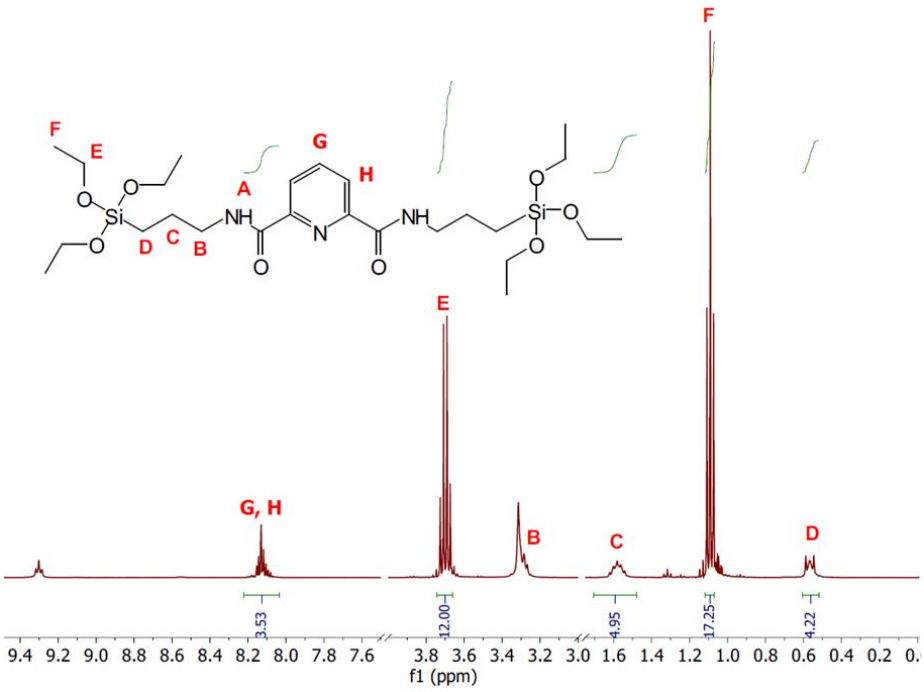

Figure S2 Spectrum of the ^{1}H liquid state NMR of the synthesised BiTSAP precursor measured in DMSO-d_6.

9.2 ^{13}C liquid state NMR spectra of synthesised precursor

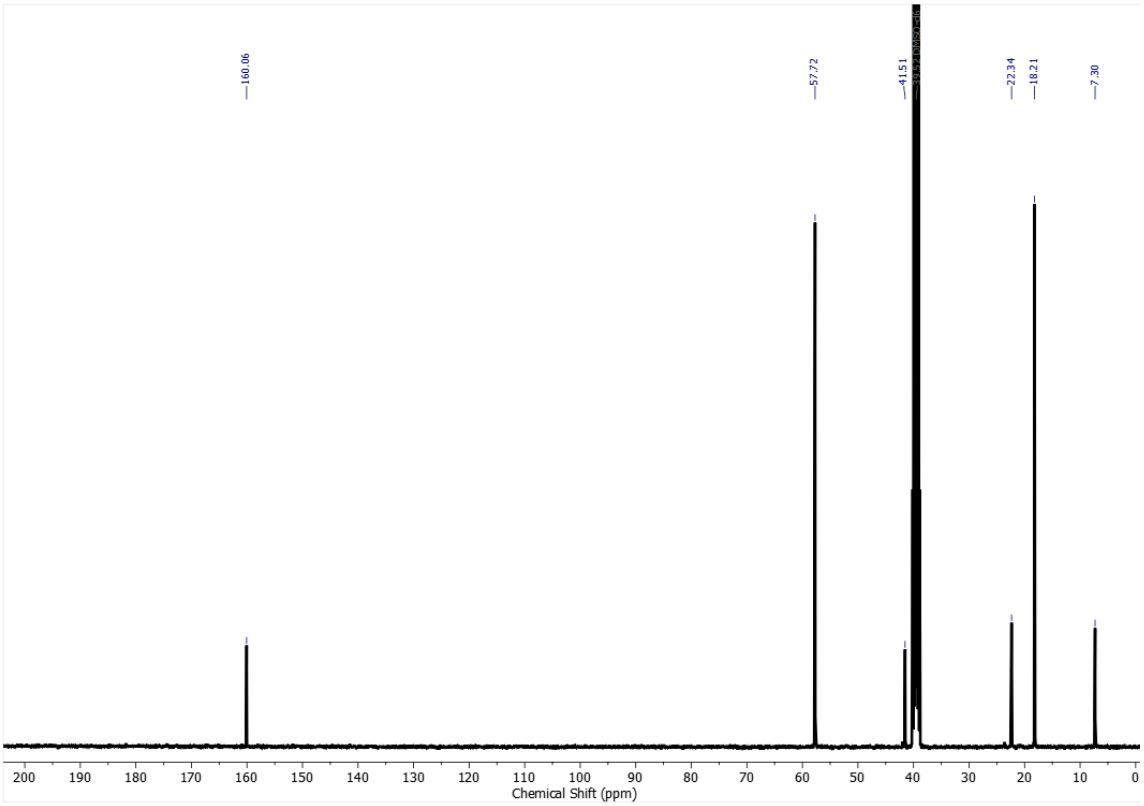

Figure S3 Spectrum of the ^{13}C liquid state NMR of the synthesised OBA precursor measured in DMSO-d_6.

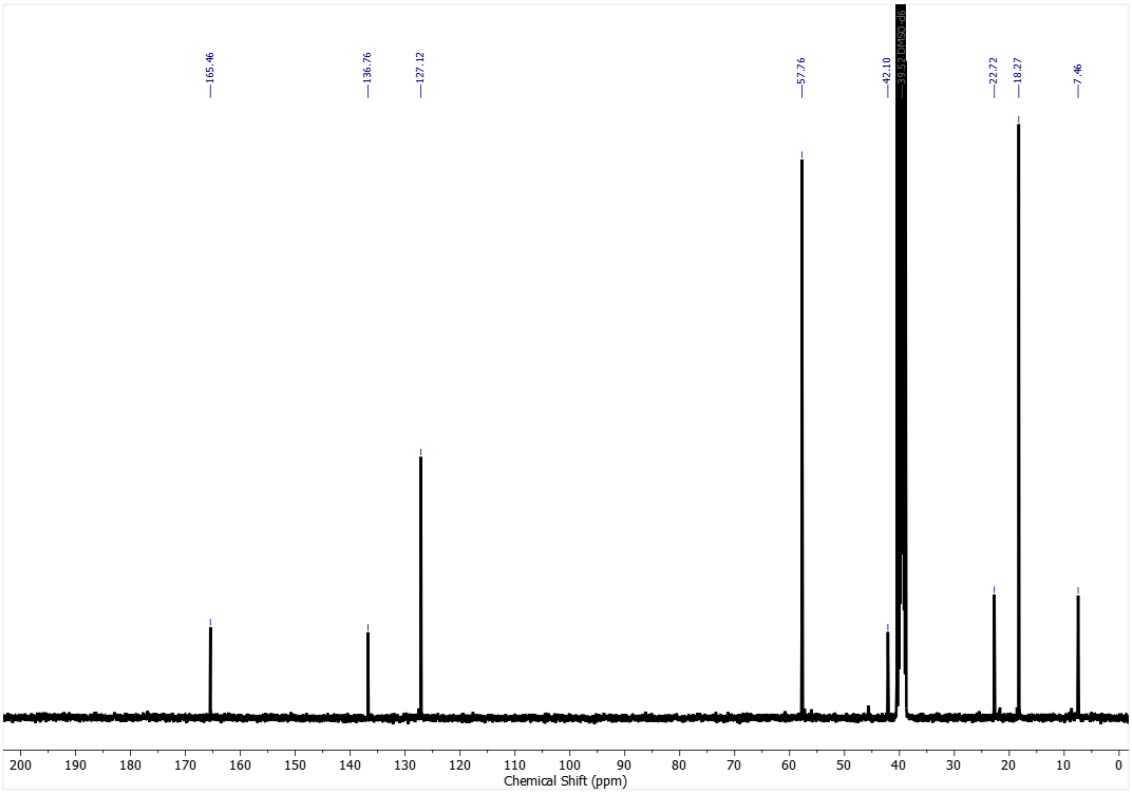

Figure S4 Spectrum of the ^{13}C liquid state NMR of the synthesised BiTSAB precursor measured in DMSO-d_6.

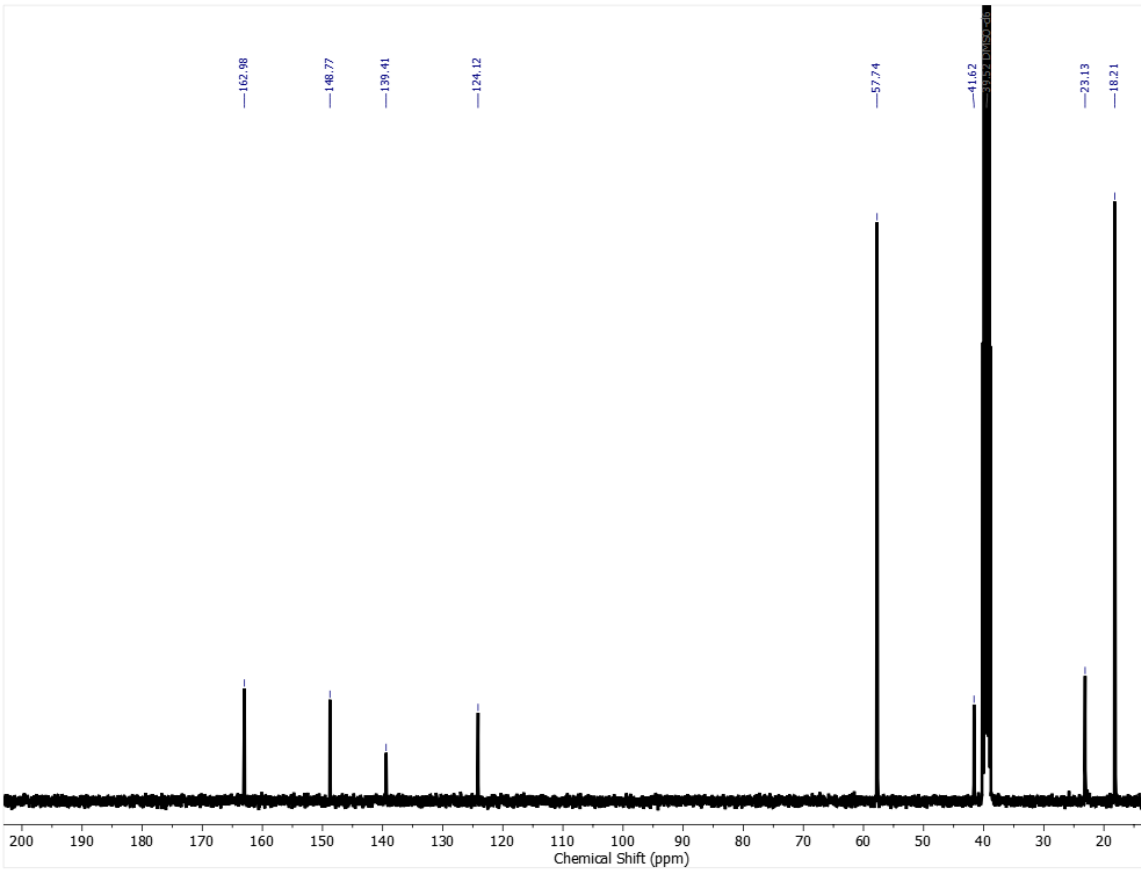

Figure S5 Spectrum of the ^{13}C liquid state NMR of the synthesised BiTSAP precursor measured in DMSO-d_6.

9.3 Thermal stability of synthesised precursors

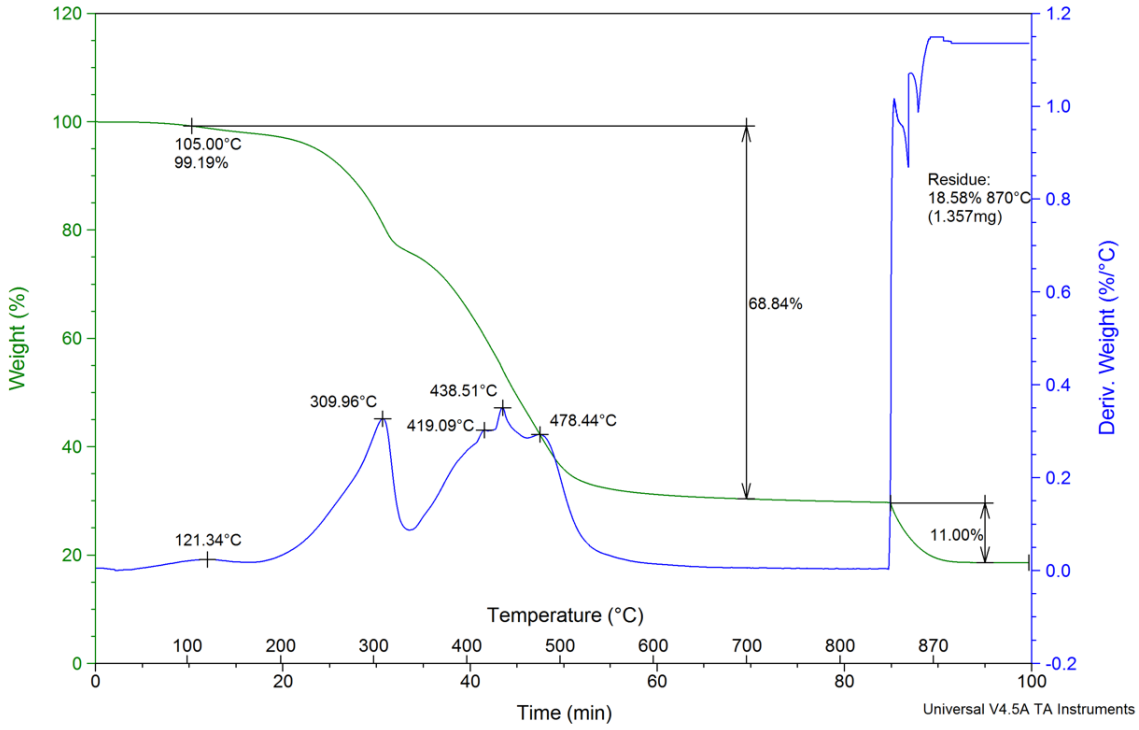

Figure S6 Scheme of thermal behaviour of synthesised precursor BiTSAB.

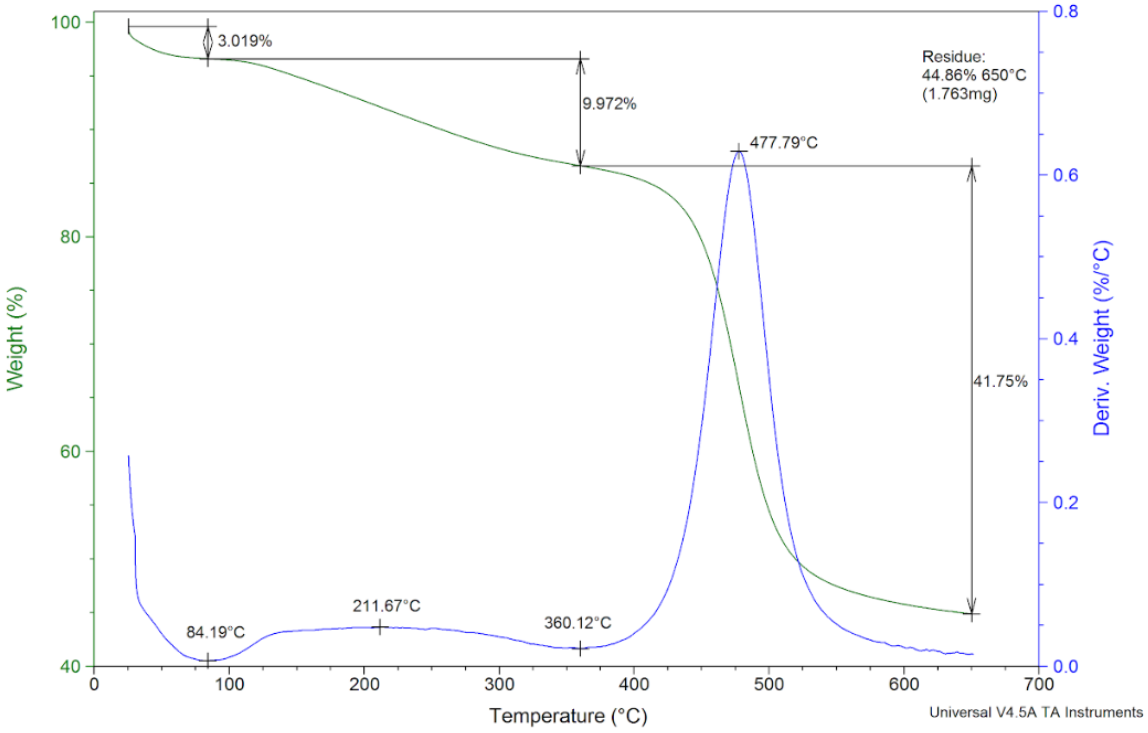

Figure S7 Scheme of thermal behaviour of synthesised precursor BiTSAP.

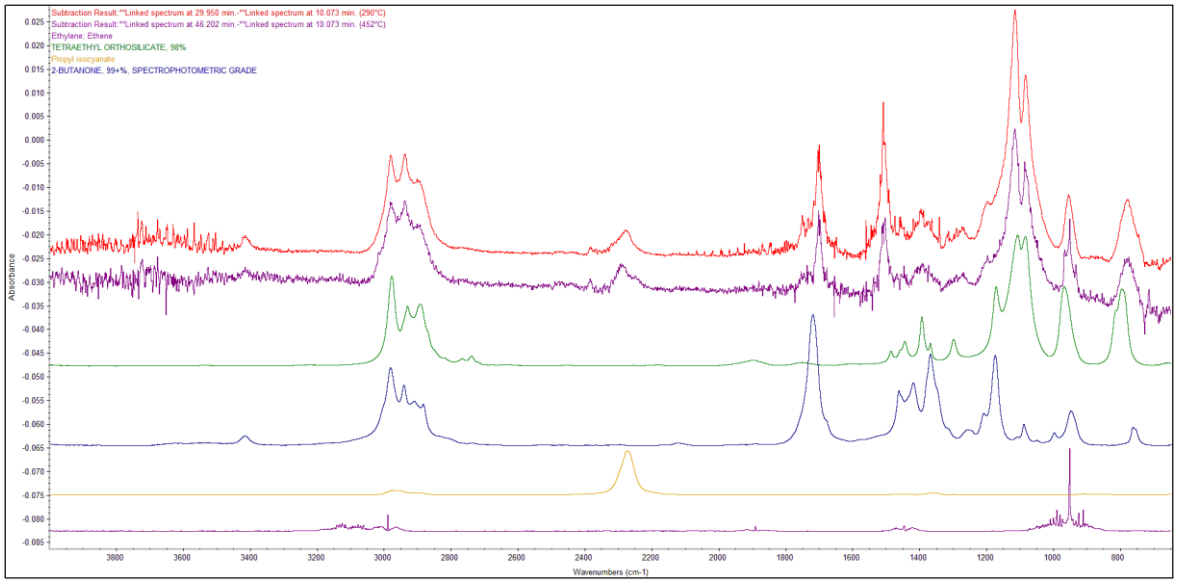

Figure S8 FT-IR spectra at chosen data points (temperatures) from tandem TGA compared with reference spectra for assigning major products of OBA precursor thermal degradation.

9.4 FTIR spectra of sol-gel reactions with focus on the range 1700 – 400 cm^{-1}

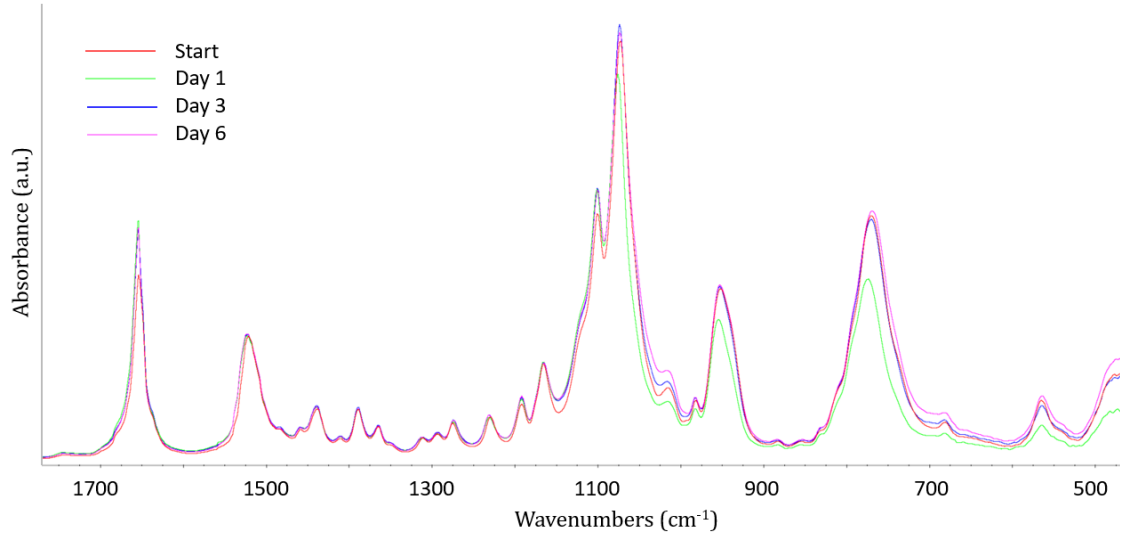

Figure S9 FTIR spectra of sol-gel reaction of OBA precursor in low Alc system.

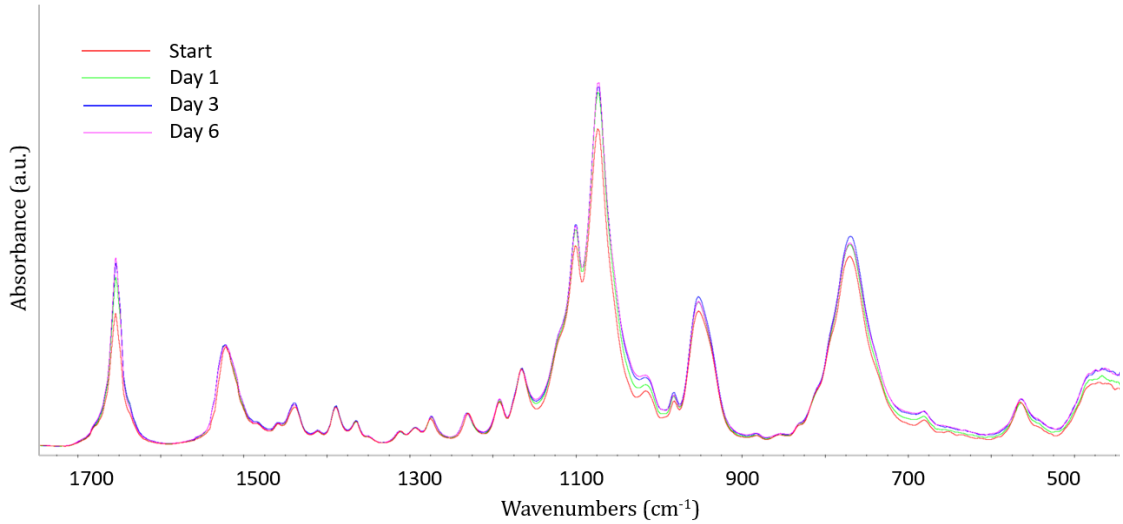

Figure S10 FTIR spectra of sol-gel reaction of OBA precursor in calculated MW Alc system.

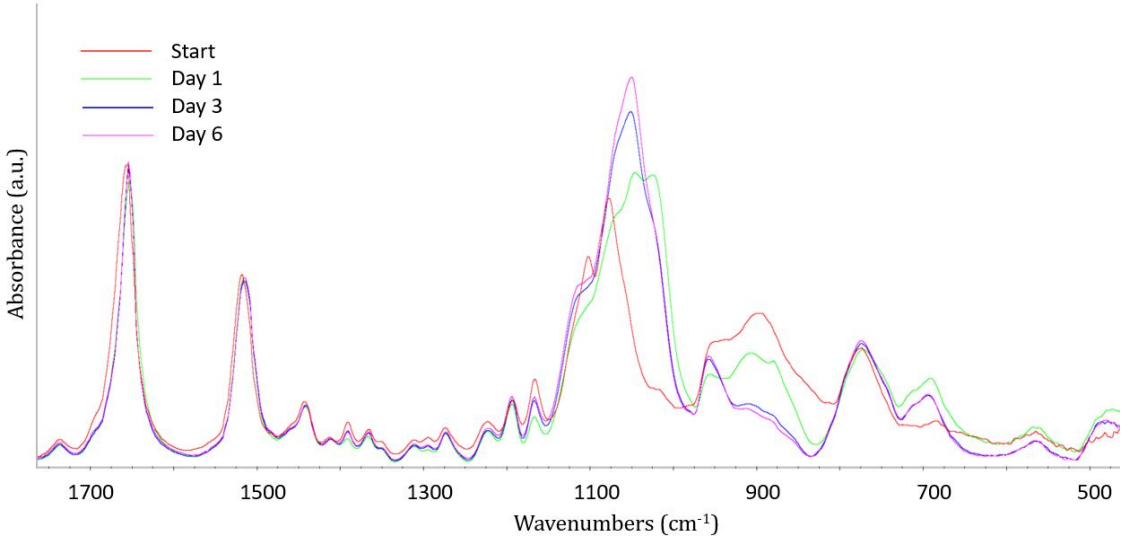

Figure S11 FTIR spectra of sol-gel reaction of OBA precursor in high Alc system.

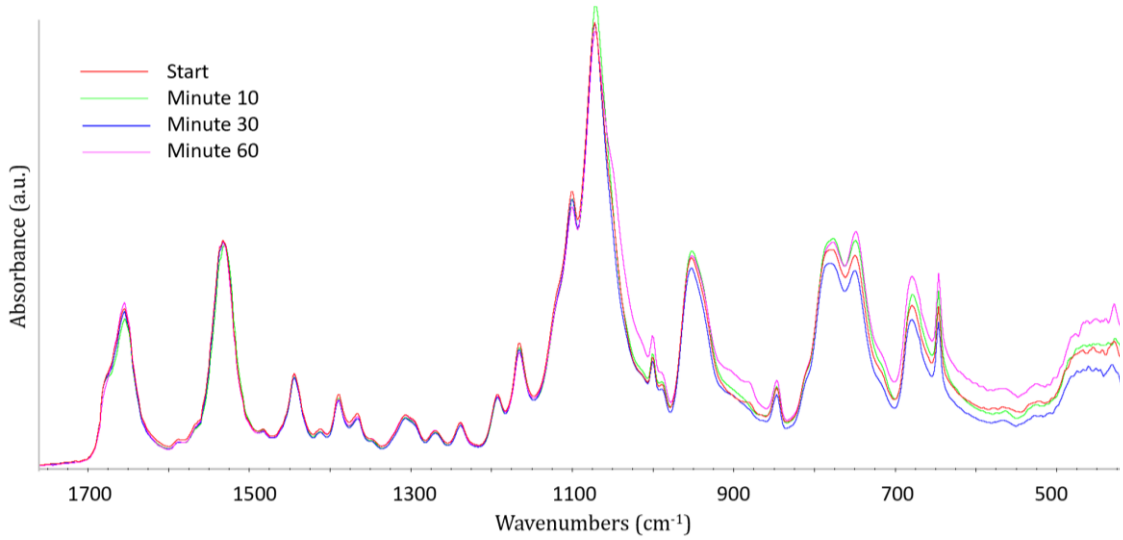

Figure S12 FTIR spectra of sol-gel reaction of BiTSAB precursor in low Alc system.

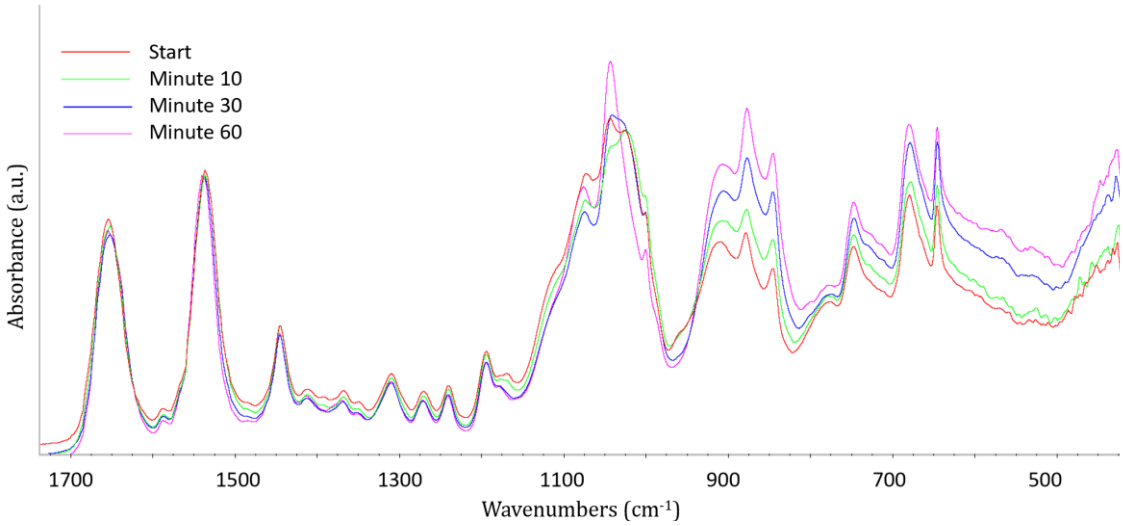

Figure S13 FTIR spectra of sol-gel reaction of BiTSAB precursor in calculated MW Alc system.

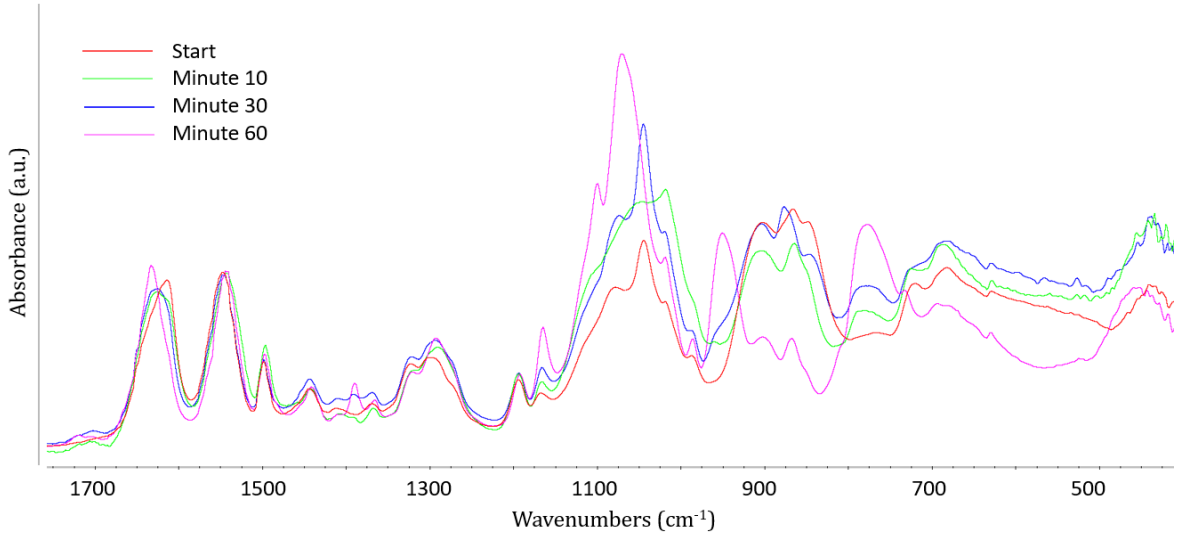

Figure S14 FTIR spectra of sol-gel reaction of BiTSAB precursor in high Alc system.

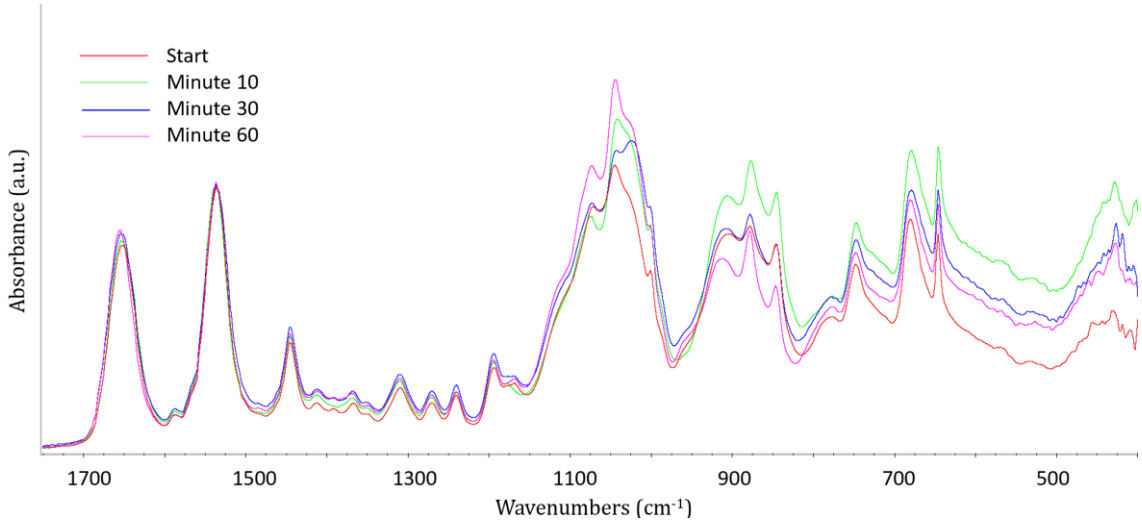

Figure S15 FTIR spectra of sol-gel reaction of BiTSAP precursor in low Alc system.

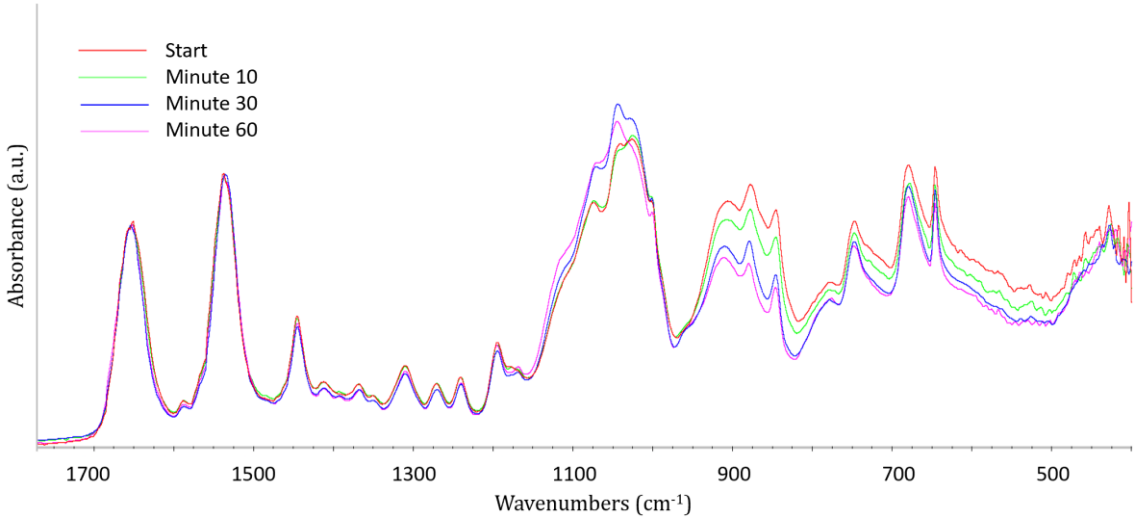

Figure S16 FTIR spectra of sol-gel reaction of BiTSAP precursor in calculated MW Alc system.

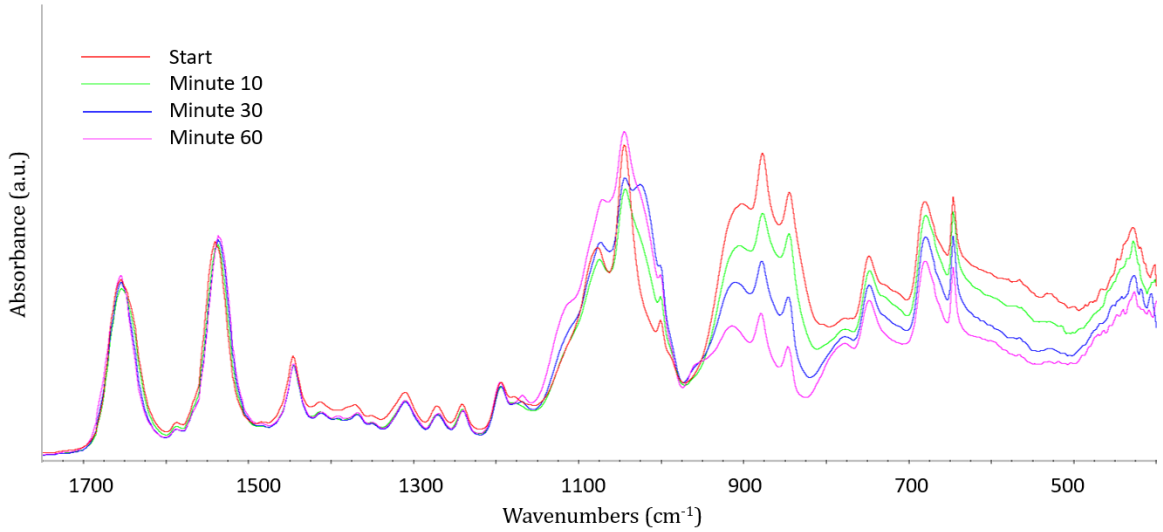

Figure S17 FTIR spectra of sol-gel reaction of BiTSAP precursor in high Alc system.

9.5 ^{13}C solid state NMR spectra of created fibres

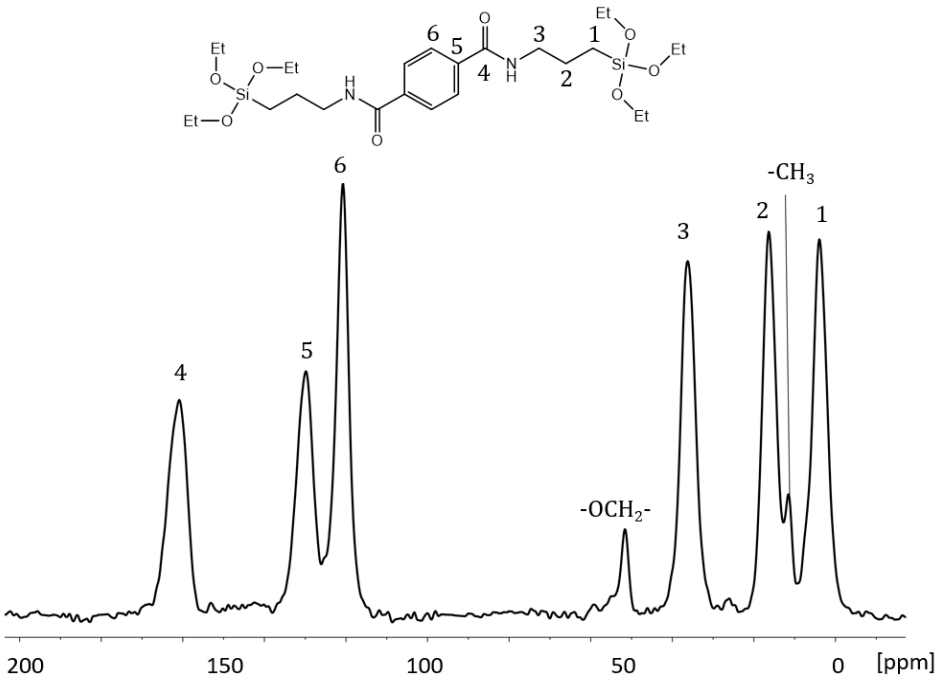

Figure S18 Spectrum of the ^{13}C liquid state NMR of the created BiTSAB fibres measured in DMSO-d_6.

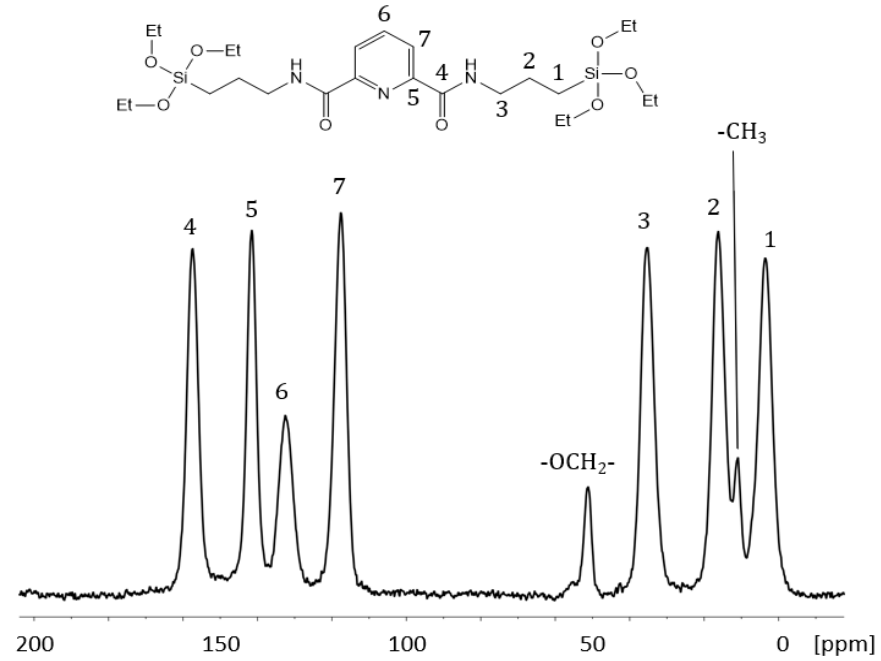

Figure S19 Spectrum of the ^{13}C liquid state NMR of the created BiTSAP fibres measured in DMSO-d_6.

9.6 Thermal stability of produced fibrous materials

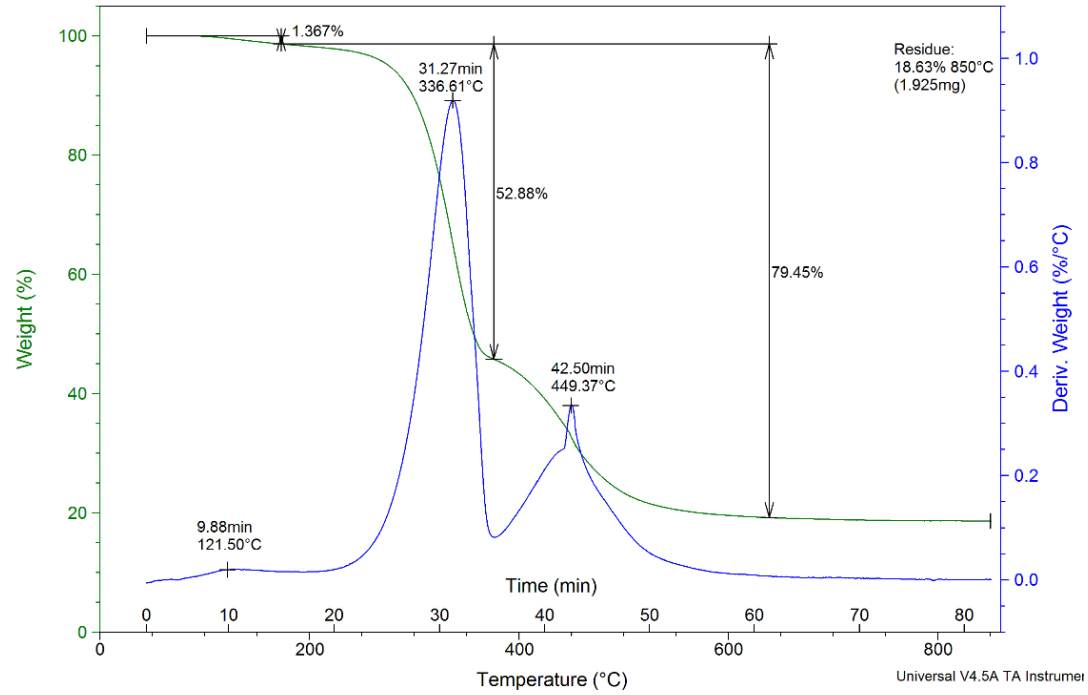

Figure S20 Scheme of thermal behaviour of created fibrous materials made from BiTSAB.

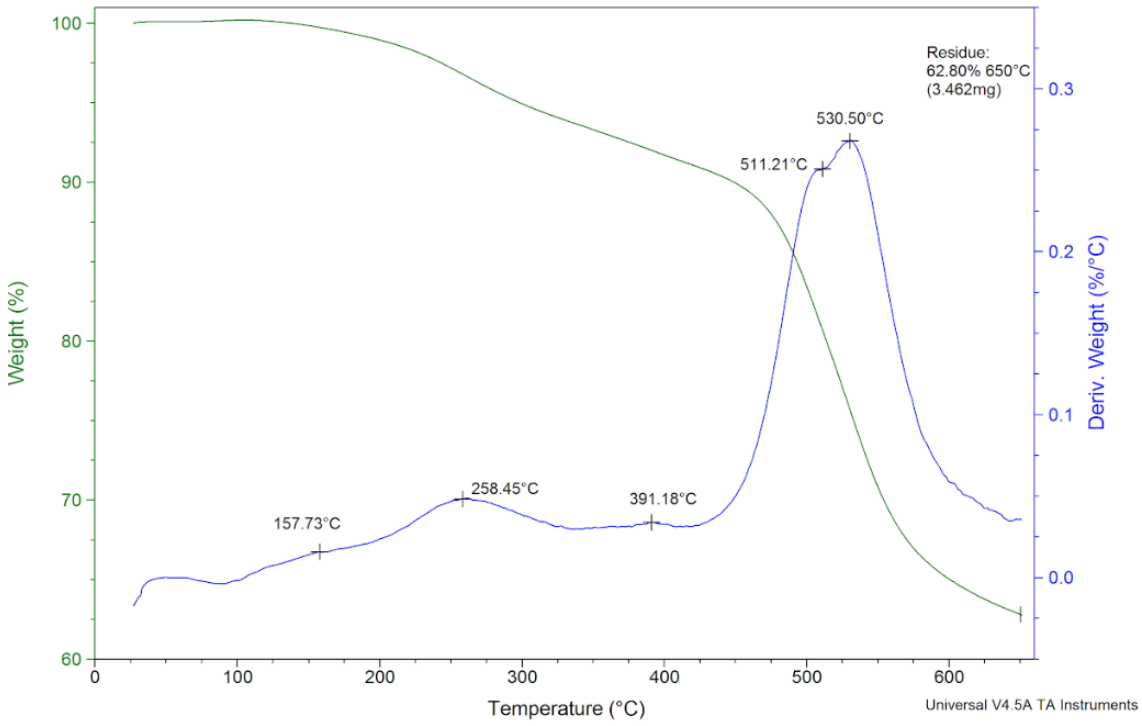

Figure S21 Scheme of thermal behaviour of created fibrous materials made from BiTSAP.

9.7 Specific surface area (BET method)

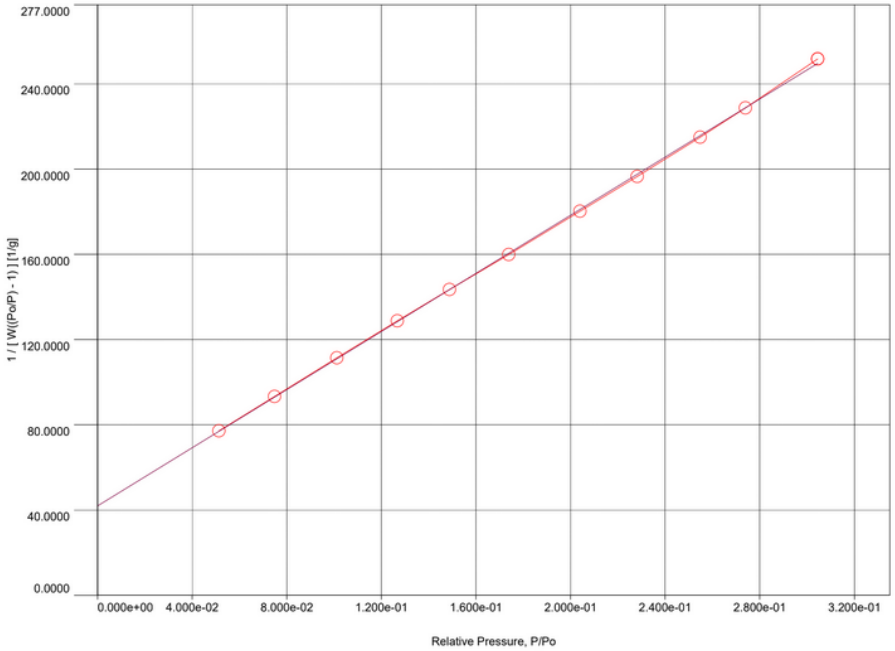

Figure S22 Adsorption isotherm of created OBA fibres.

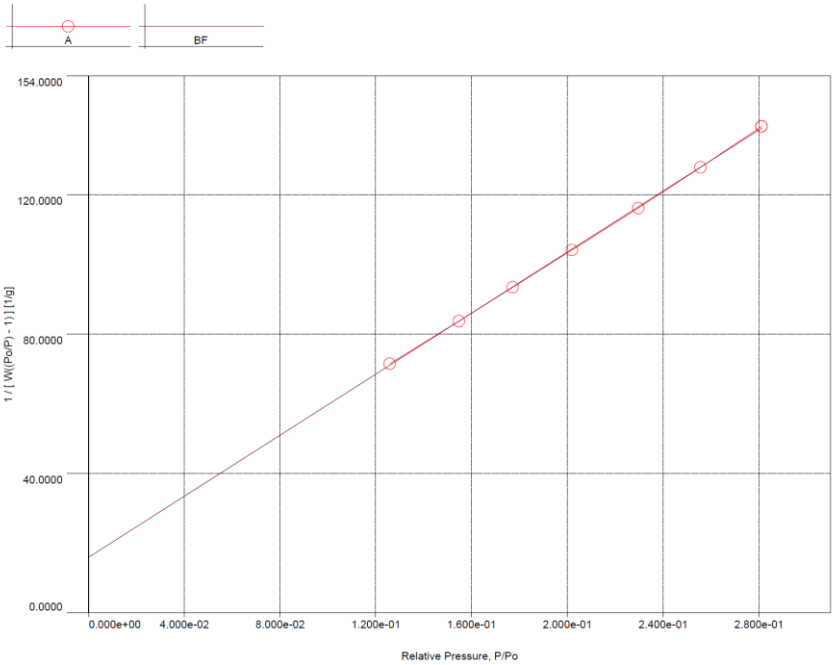

Figure S23 Adsorption isotherm of created BiTSAB fibres.

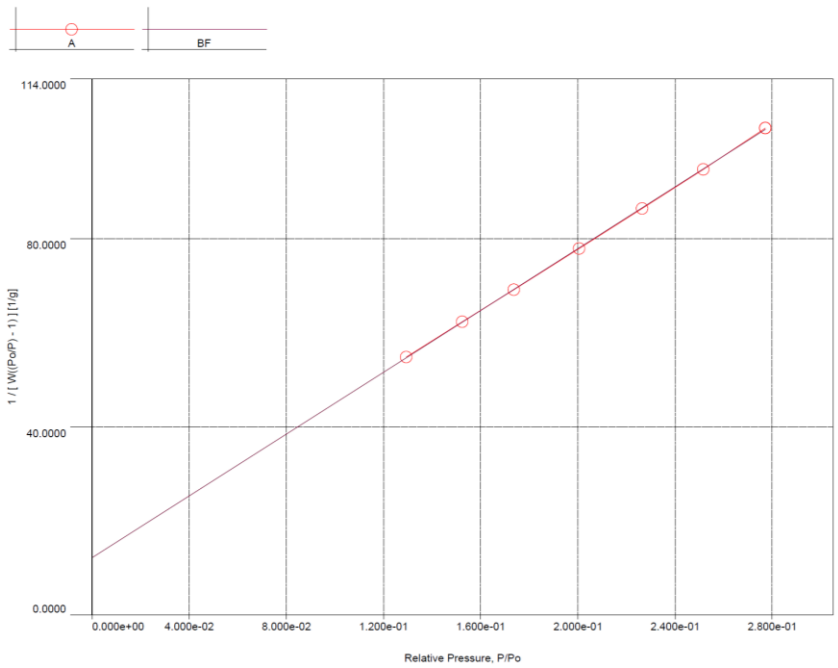

Figure S24 Adsorption isotherm of created BiTSAP fibres.

9.8 Metabolic activity ASC cells in the presence of OBA and PS fibres

In the study of cell biology, the visualization technique of cellular structures involves fluorescence staining using phalloidin and DAPI. Phalloidin, a cyclic heptapeptide derived from the poisonous Amanita phalloides, specifically binds to the cellular cytoskeleton. This binding allows for the visualization of cell morphology by highlighting the actin filaments. In conjunction with phalloidin, DAPI is employed to visualize cell nuclei. DAPI fluoresces blue upon binding to DNA, providing a clear and distinct view of the cell's nuclear architecture (**Figure S25**). The samples underwent fixation with 4% formaldehyde, ensuring structural preservation before staining. The resulting fluorescence images were captured using an Olympus fluorescence microscope. The dual staining approach offers a comprehensive insight into cell structure and organization (**Figure S30**).

Tracking the number of cells is also important technique providing quantitative data on cell proliferation or viability. **Figure S31** focuses on the monitoring of cell morphology, offering valuable information about changes in cell shape or structure over time. This combination of visualization techniques, employing phalloidin and DAPI staining, alongside quantitative analyses, enhances our understanding of cellular dynamics.

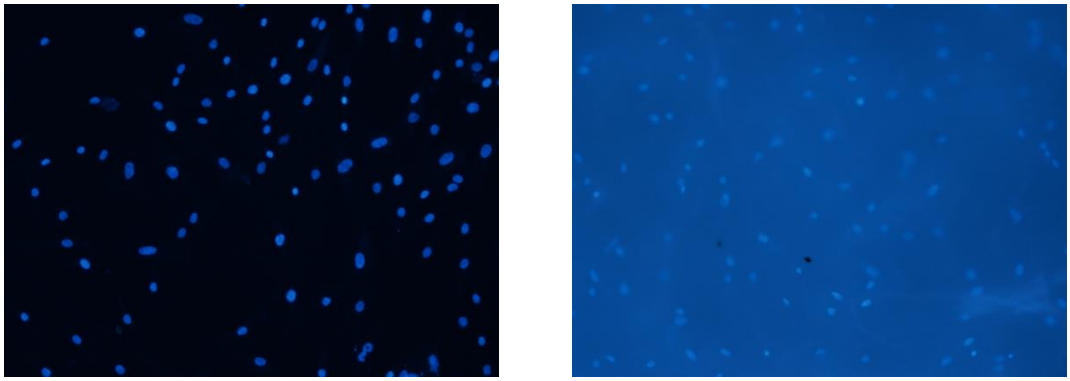

Figure S25 DAPI staining nuclei after day 2; (a) PS; (b) OBA.

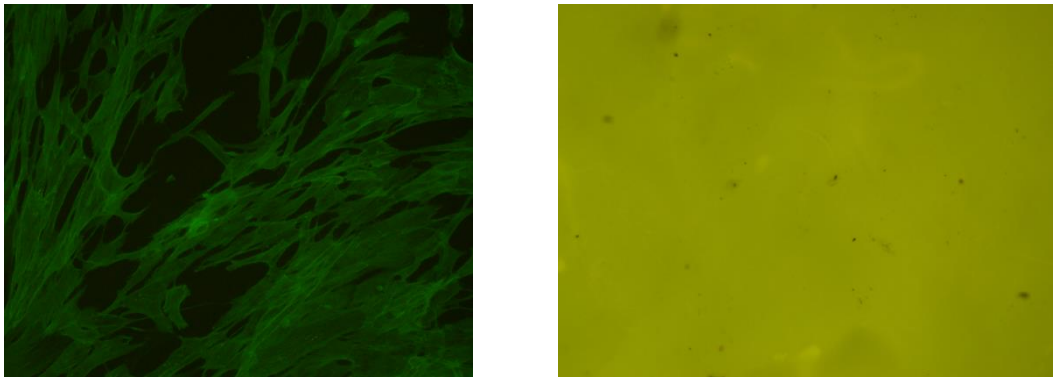

Figure S26 Phalloidin-DAPI staining after day 2; (a) PS; (b) OBA.

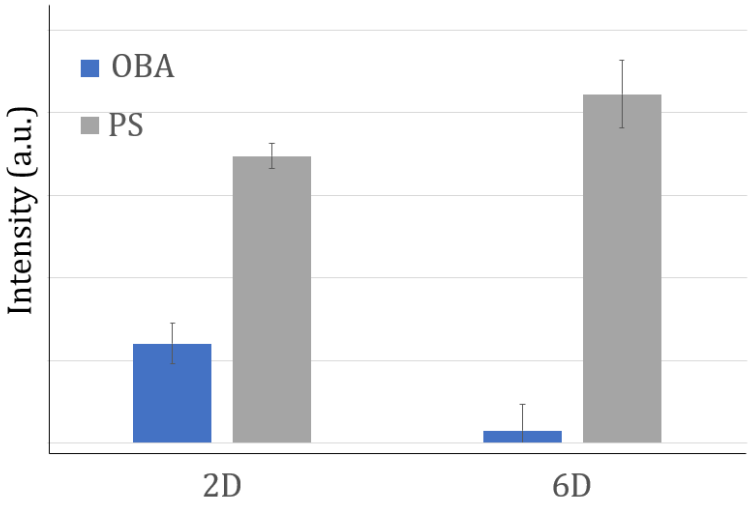

Figure S27 Metabolic activity of ASC cell depending on the underlying material.

9.9 Morphology of cell lines HUVEC and ADSC

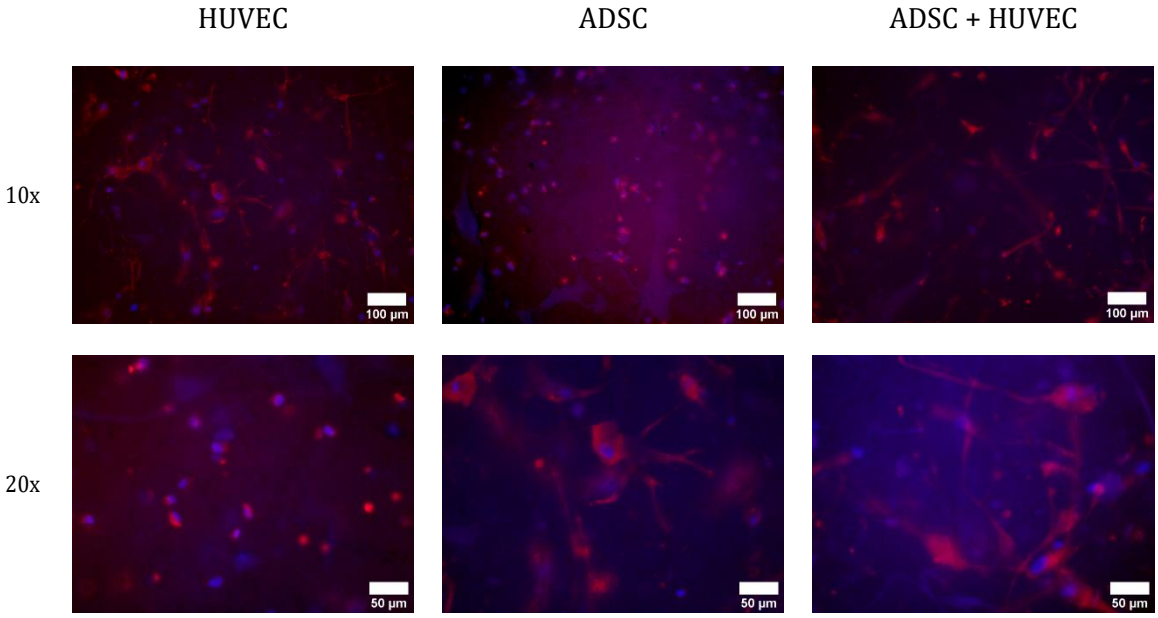

Figure S29 Morphology of cell lines after 3 days seeded on material BiTSAB; visualised by F-actin staining (red) and Cell nuclei counterstained by DAPI (blue). Fluorescent images were acquired by Microscope Olympus IX71 (digital camera DP71, two magnifications).

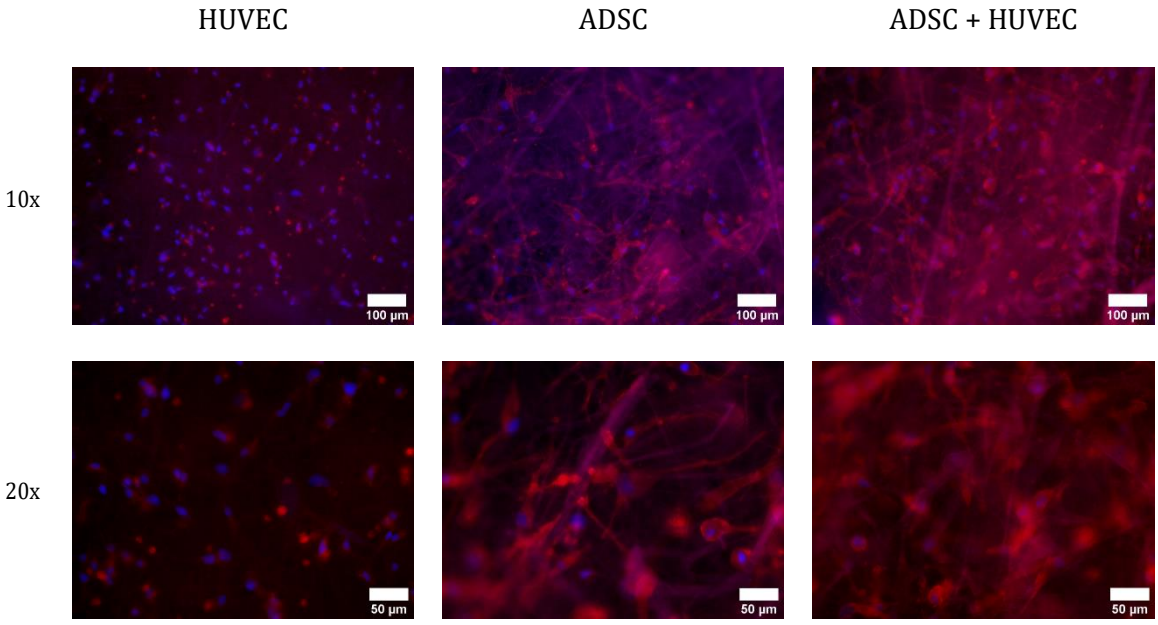

Figure S30 Morphology of cell lines after 3 days seeded on material BiTSAP; visualised by F-actin staining (red) and Cell nuclei counterstained by DAPI (blue). Fluorescent images were acquired by Microscope Olympus IX71 (digital camera DP71, two magnifications).

9.10 Testing of iMR-90

The application of iMR-90 neural stem cells to the nanofibrous samples, following a methodology similar to the previous experiment, yielded notable outcomes. However, at the 48-hour mark post-seeding, observations revealed that only a limited number of cell

clusters were present on the OBA fibrous samples. Remarkably, the morphology of the neural stem cells suggested challenges in proper attachment to the nanofibrous surface. These findings prompt a deeper investigation into the interaction dynamics between the neural stem cells and the nanofibrous substrates, emphasizing the critical role of surface characteristics and cell-material interactions in influencing cellular adhesion and morphology. Further exploration of these observations may contribute valuable insights for refining the nanofibres design to enhance the compatibility and support for neural stem cell attachment and growth.

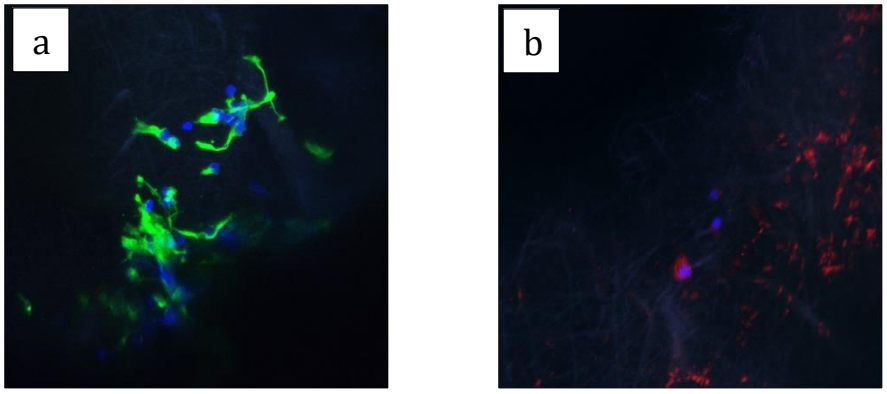

Figure S28 Nestin/DAPI staining (a); βIIItubulin/DAPI staining of iMR-90 cells after 2 days of seeding on OBA sample.